Electronic transport properties of topological insulators

Pierre Adroguer

Thèse de doctorat de
l'Ecole Normale Supérieure de Lyon

Discipline : Physique

Laboratoire de Physique, ENS de Lyon
Ecole doctorale de Physique et Astrophysique de Lyon

Présentée et soutenue publiquement le 15 février 2013 par

Pierre Adroguer

En vue d'obtenir le grade de

Docteur de l'Ecole Normale Supérieure de Lyon - Université de Lyon

---

Propriétés de transport électronique des isolants topologiques

---

devant le jury composé de :

David Carpentier	Directeur de thèse
Pascal Degiovanni	Directeur de thèse
Laurent Lévy	Président du jury
Gilles Montambaux	Examinateur
Christophe Texier	Rapporteur
Björn Trauzettel	Rapporteur

ENS DE LYON

Université de Lyon

Parce que quand on a le goût de la chose, quand on a le goût de la chose bien faite, le beau geste, parfois on ne trouve pas l'interlocuteur en face je dirais, le miroir qui vous aide à avancer. Alors ce n'est pas mon cas, comme je disais là, puisque moi au contraire, j'ai pu : et je dis merci à la vie, je lui dis merci, je chante la vie, je danse la vie...

Astérix : Mission Cléopâtre

Remerciements

Il est d'usage de commencer un manuscrit de thèse par des remerciements. Cependant, j'aimerais que les personnes que je remercie ci-après ne considèrent pas ces remerciements comme le résultat d'un exercice nécessaire, mais bel et bien comme une preuve (peut-être maladroite) de ma gratitude.

Je tiens à remercier en premier lieu David Carpentier, pour la qualité de son encadrement qui m'a permis d'effectuer ce travail. Sa pédagogie lors de ma découverte du sujet, son enthousiasme à mesure de ma progression ainsi que sa disponibilité ont été plus que précieux. Je voudrais aussi remercier Pascal Degiovanni qui m'a peut-être accompagné d'un peu plus loin au niveau scientifique, mais qui a toujours été présent pour m'aider à clarifier mes idées, surtout quand elles étaient loin de l'être.

Je voudrais aussi remercier Björn Trauzettel et Christophe Texier d'avoir accepté d'être les rapporteurs de cette thèse. Malgré le peu de temps à leur disposition, leur lecture attentive et leurs conseils m'ont permis d'améliorer ce manuscrit en le débarrassant de certaines scories. Merci aussi à Gilles Montambaux d'avoir accepté d'être membre de ce jury, et à Laurent Lévy de l'avoir présidé.

Je me demande si j'aurais pu mener à bien un tel travail dans un autre laboratoire que celui de l'ENS de Lyon, tant le cadre de travail a été agréable. Je voudrais remercier les membres du groupe de travail Matière Condensée (Pascal, David, Tommaso, Andrei, Edmond, Guillaume, Louis-Paul, Cyrille, Peter, ...), qui ont été les premiers à faire les frais de mes présentations, et l'équipe de physique théorique de manière générale. Un grand merci aussi à l'équipe pédagogique du département de physique de m'avoir si bien accueilli dans ses rangs, et aux services techniques (Laurence, Laure, Nadine, Hervé, Bertrand) qui nous permettent de travailler dans d'excellentes conditions. Mais comme la vie d'un labo ne se résume pas qu'au travail, je voudrais remercier tous les gens avec qui j'ai pu partager un café, un repas, une discussion ou encore un match de foot. Un peu dans le désordre : Chris, Les Baptistes, Ju, Nico, Ernesto, Angel, Thierry, Patrick, Clément, Thomas, Etienne, Nicolas, et tant d'autres.

A la fin de mon périple scolaire, je me rends compte que j'ai eu la chance de rencontrer des professeurs dont les conseils m'ont poussé à me dépasser et m'ont mené jusqu'ici. En remontant le cours du temps, je pense à Peter qui m'a introduit à la beauté de la matière condensée, à mes professeurs de prépa MM. Gonnord et Mercier, et plus loin dans le temps à MM. Sagné et Bergé qui ont encouragé ma curiosité scientifique. Et surtout un grand merci aux premiers à avoir apporté des réponses à mes "pourquoi" et "comment", à savoir mes parents et ma famille.

La fin de cette thèse coïncide avec la fin de ma présence au sein de l'Ecole Normale Supérieure de Lyon, qui m'aura hébergé pendant 7 ans. Durant ce septennat, j'ai rencontré quantité de gens formidables, je pense particulièrement aux Zébus et à l'AS, donc merci à Ju, Fifi, Anto, Bru, Marek, Tom, Bat, Bleue, Anne-so, Tam, Magouille, Lise, Paulo, Chris, Dam, Marjo, Oliv, Marion. Une attention particulière va à ceux qui ont partagé leur logement avec moi pendant quelque temps, et dont les discussions ont été un réel encouragement à entamer une thèse, tout comme l'ont été celles avec mes amis de prépa (Pimousse, Matou, Rod, etc).

Cependant, la plus belle rencontre que j'ai faite ici est celle de Charlène qui a été à mes cotés du début jusqu'à la fin de cette thèse, et que je ne saurai remercier assez pour son soutien et sa patience à mon égard.

Contents

Résumé de la thèse

Un des buts de la physique moderne est de comprendre les propriétés électroniques des solides. En effet, comment expliquer leur variété alors que les élements de départ sont les mêmes pour tous les solides, à savoir des électrons, des protons et des neutrons ? Par exemple, quelle est la cause de la différence entre les isolants comme le bore, et les isolants comme l'aluminium ? Ou encore quelle est l'origine du magnétisme ou de la supraconductivité ?

Un des grands succès de la physique de la matière condensée dans les années soixante a été de comprendre ces différentes propiétés à travers une unique théorie, baptisée théorie de Ginzburg-Landau. Dans ce cadre, on montre que ces transitions de phase sont associées à des brisures spontanées de symétries quand la température diminue. par exemple, la transition d'un matériel entre une phase paramagnétique et une phase magnétique à la température de Curie T_C correspond à la brisure de la symétrie $SU(2)$ des moments magnétiques intrinsèques : au-dessus de T_C, ils pointent dans des directions différentes, mais tendent à s'aligner lorsque la température descend sous T_C. De même, la transition vers un supraconducteur correspond à la brisure d'une symétrie de jauge, et un cristal brise la symétrie par transition, au contraire d'un liquide.

Cette classification des solides en fonction des symétries spontanément brisées a nécessité d'être raffinée lors de la découverte de l'effet Hall quantique entier par von Klitzing *et al.* en 1980. Dans le cadre des symétries spontanément brisées, on s'attend à ce que cette phase soit un isolant, puisquil s'agit d'un cristal ne présentant pas d'électrons de conduction. Cependant, von Klitzing *et al.* ont montré l'existence d'états de bord conducteurs. De manière plus surprenante, ces états de bord sont robustes : ils ne disparaissent pas en présence du désordre. il a été rapidement montré que la présence et la robustesse de ces états de bord est expliquée par un ordre topologique en complément des symétries brisées. Les expériences sur l'effet Hall quantique entier requièrent des champs magnétiques intenses, des faibles températures et un gaz d'électrons purement bidimensionnel. Il était alors admis qu'il était nécessaire de briser l'invariance par renversement du temps et des échantillons bidimensionnels pour observer un ordre topologique non trivial.

Cependant, Kane et Mele ont proposé en 2005 que le graphène pouvait présenter un tel ordre topologique non trivial, tout en respectant l'invariance par renversement du temps. Le graphène est le premier exemple d'un cristal

bidimensionnel, et venait juste d'être réalisé expérimentalement. Il s'agit d'un semi-métal (les bandes de conduction et de valence se touchent), mais Kane et Mele ont montré que la prise en compte du couplage spin-orbite ouvre un gap entre les deux bandes, et le graphène devient isolant. De plus, ce couplage spin-orbite est responsable d'un ordre topologique non trivial qui se manifeste par l'apparition de deux états de bord contre-propageants et de spin opposé. Cette phase topologique non triviale, différente d'un isolant conventionnel (par la présence de deux états de bord conducteurs), et de l'effet Hall quantique (par le respect de l'invariance par renversement du temps) a été aussi prédite dans des puits quantiques de HgTe/CdTe, où le couplage spin-orbite joue aussi un rôle crucial. Peu après, cette phase a été généralisé à des équivalents tridimensionnels, contrairement à l'effet Hall quantique. Ces isolants topologiques tridimensionnels ont été proposés en premier dans l'alliage Bi_xSb_{1-x}, puis dans une famille de semi-conducteurs conventionnels comme Bi_2Se_3, Bi_2Te_3, Sb_2Se_3, ou encore dans du HgTe sous contrainte.

Les réalisations expérimentales des ces prédictions d'isolants topoogiques ont vite suivi : l'effet Hall quantique de spin a été observée par Molenkamp *et al.* dans des puits quantiques de HgTe/CdTe, et les isolants topologiques tridimensionnels par différents groupes dans différents matériaux (Hasan *et al.*, Ando *et al.*, Kapitulnik *et al.*, Lévy *et al.*).

Ces réalisations expérimentales ont été la source d'un grand enthousiasme dans la communauté de la matière condensée, grâce aux applications potentielles de ces isolants topologiques, au-delà de leur seul intérêt d'un point de vue fondamental. L'effet Hall quantique de spin présente de robustes états de bords hélicaux ; leur robustesse empêche la rétrodiffusion, et donc la perte de potentiel chimique le long du bord : ils sont parfaitement transmis. Associé au fait qu'il trie les spins selon leur direction (des spins opposés vont dans des directions opposés), cette transmission sans dissipation des états de bord fait de l'effet Hall quantique de spin un candidat idéal pour la spintronique.

De plus, associés à des supraconducteurs, les isolants topologiques tridimensionnels pourrait réaliser des supraconducteurs topologiques, et créer des fermions de Majorana. De la même manière que les isolants topologiques sont des isolants avec des états de bord ou de surface robustes, les supraconducteurs topologiques présentent des états de bord ou de surface protégés par la topologie : les fermions de Majorana. Ces fermions de Majorana sont des particules fondamentales dont l'existence est discutée depuis leur proposition en 1937, et sont remarquables en ce qu'ils sont leur propre antiparticule. Le tressage de ces fermions de Majorana suit une statistique non-abélienne, ce qui est très utile pour l'informatique quantique, et la preuve de leur existence dans une hétérostructure isolant topologique/supraconducteur par Kouwenhoven *et al.* en 2012 est une étape importante, même si ces résultats ne font pas consensus.

Quand on s'intéresse aux propriétés électroniques, les expériences de transport sont des outils naturels et puissants pour classer les solides. Par exem-

ple, la découverte de l'effet Hall quantique entier a été faite en observant des plateaux lors de la mesure d'une conductivité transverse en fonction d'un champ magnétique.

Le transport des électrons dans un cristal est expliqué par la théorie des ondes de Bloch : les électrons de conduction sont soumis à un potentiel périodique créé par les ions du cristal. cette périodicité engendre la délocalisation des électrons par le théorème de Bloch. La théorie du liquide de Fermi-Landau assure que l'on peut négliger les interactions entre électrons ou entre les électrons et les ions du cristal, et que l'on peut considérer les électrons comme des électrons libres avec une masse renormalisée. Les résultats de la théorie de Fermi-Landau sont en excellent accord avec les expériences conduites sur les conducteurs, même à très basse température.

Dans le cas de l'effet Hall quantique, qui est un isolant, le transport correspond à des canaux indépendants unidimensionnels : les états de bord. On utilise alors le formalise de Landauer-Büttiker pour décrire le transport et retrouver les plateaux dans la mesure de la conductance. On peut décrire avec le même formalisme le cas de l'effet Hall quantique de spin où les deux états de bords contre-propageants sont indépendants et calculer la valeur attendue pour les conductances.

Le cas des états de surface d'un isolant topologique tridimensionnel est différent à cause du phénomène de diffusion : en présence d'impuretés, un électron avec une direction de propagation donnée peut-être réfléchi dans n'importe quelle direction, contrairement au cas unidimensionnel où le désordre n'est pas pertinent. Cette diffusion permet alors des interférences quantiques, responsables dans le régime mésoscopique (basse température, faible désordre et petits échantillons) du phénomène de localisation faible et de fluctuations universelles de la conductance. Ce régime mésoscopique est le régime naturel pour décrire les expériences menées sur les isolants topologiques, il est donc nécessaire de calculer la valeur de cette correction de localisation faible et de l'amplitude des fluctuations de conductance afin de les comparer aux expériences : une description théorique reliant les propriétés topologiques des matériaux aux grandeurs mesurées expérimentalement nous aidera à classer les solides.

Pendant ma thèse, j'ai étudié principalement deux problèmes. Le premier concerne l'effet Hall quantique de spin, et comment on peut utiliser un supraconducteur afin de sonder ses propriétés uniques en y injectant des paires de Cooper. Nous en avons en particulier montré que la conservation du spin total de la paire pendant son transfert, associé avec l'hélicité des canaux de bords engendre une séparation parfaite de la paire de Cooper. Dans le cas où la région supraconducteur est grande, nous avons alors prédit une réflexion d'Andreev totale, ce qui a été observé expérimentalement peu après a publication de nos résultats dans *Probing the helical edge states of a topological*

insulator by Cooper-pair injection published in Physical Review B, **82**, 081303 (R).

J'ai ensuite étudié le diffusion des états de surface des isolants topologiques tridimensionnels. Ces états de surface présentent une relation de dispersion relativiste, ils sont donc décrits comme des fermions de Dirac. Nous avons dans un premier temps calculé la conductance obtenue pour des fermions de Dirac en présence de désordre, en utilisant deux techniques, la résolution de l'équation de Boltzmann et un calcul diagrammatique standard. La technique diagrammatique nous a aussi permis de calculer la valeur de la correction de localisation faible ainsi que les amplitudes des fluctuations de conductance. Nous avons pu vérifier que la conductivité est alors fonction d'un seul paramètre, le coefficient de diffusion, une fois que la classe de symétrie universelle, dépendant des symétries explicitement brisées par le hamiltonien, est connue. Nous avons ensuite pris en compte le gauchissement hexagonal de ces cônes de Dirac observé expérimentalement dans notre étude, et ce de manière non-perturbative, afin de présenter une théorie au plus proche des conditions expérimentales. Ces travaux ont été publiés dans *Diffusion at the surface of topological insulators* in New Journal of Physics, **14**, 103027.

Introduction

One goal of modern physics is to understand the electronic properties of solids, and how to classify them. Indeed, starting with so few ingredients (protons, neutrons and electrons), how can we explain the variety of the electronic properties of solids ? For example, what causes the difference between insulators as boron, and metals as aluminum ? Where does magnetism or superconductivity come from ?

A great success of condensed matter physics in the 1960's was to understand within a unique framework the origin of these different properties between solids. From Ginzburg-Landau's theory, it can be shown that phase transitions occur when temperature decreases, simultaneously with spontaneous symmetry breaking[1]. For example, the transition between a paramagnet and a ferromagnet at the Curie temperature T_C corresponds to the breaking of the SU(2) symmetry of the spin : above T_C, all the spins of the sample point in different directions, but below T_C they all tend to point in the same direction. Similarly, the superconducting transition is explained by a breaking of a gauge symmetry, and a crystal breaks the translational symmetry, as opposed to a liquid.

This classification of solids depending on the spontaneously broken symmetries had to be refined with the discovery in 1980 by von Klitzing *et al.* of the integer quantum Hall effect[2]. Within the symmetry breaking framework, we expect this phase to be an insulator as it is a crystal with no conduction electrons. However, von Klitzing *et al.* showed the existence of conducting edge states. More surprisingly these edge states are robust : they do not disappear in presence of disorder. It was shown soon after that there is a topological order beyond the symmetry breaking[3], and that this topological order explains the presence and the robustness of the edge states[4]. To observe the quantum Hall effect, experiments require strong magnetic fields, low temperatures and bidimensionality of the sample considered. At the time it was believed that the breaking of the time-reversal symmetry and the bidimensionality were necessary conditions to non trivial topological orders.

However, Kane and Mele proposed in 2005[5], that graphene could present a non-trivial topological order, without breaking the time-reversal symmetry. Graphene is the first example of bidimensional crystal, just realized experimentally[6] at that moment. It is a semi-metal (conduction and valence

band touch), but Kane and Mele showed that the introduction of the spin-orbit coupling could open a gap, and turns it into an insulator. Moreover, this spin-orbit coupling is responsible for a non trivial topological order, resulting in the appearance of two robust counterpropaging edge states of opposite spins. This non trivial topological phase, different from a conventional insulator (the edge states conduct) or the quantum Hall effect (the time-reversal symmetry is preserved) was also predicted[7] in HgTe/CdTe quantum wells. In this material, spin-orbit coupling still plays a crucial role. This was soon after generalized to three dimensional equivalents[8][9][10], as opposed to the quantum Hall effect. Three dimensional topological insulators were first proposed to be seen in Bi_xSb_{1-x}, then in usual semi-conductors such as the family of compounds Bi_2Se_3, Bi_2Te_3, Sb_2Se_3[11], or stressed HgTe.

The experimental realizations of these predicted topological insulators followed rapidly : the quantum spin Hall effect in 2 dimensions by Molenkamp *et al.*[12], and the 3 dimensional topological insulators by many groups in different compounds (Hasan *et al.*[13], Ando *et al.*[14], Kapitulnik *et al.*[15], Lévy *et al.*[16]).

These experimental realizations brought a lot of enthusiasm in the field of condensed matter, motivated by potential applications of these topological insulators beyond their interest from a fundamental point of view. The quantum spin Hall phase presents robust helical edge states[17] ; their robustness implies that there is no backscattering allowed hence no loss of the chemical potential along an edge : they are perfectly transmitted. In association with their spin-filtering property (opposite spins move in opposite direction), this dissipationless transmission of the edge states turns the quantum spin Hall effect in a perfect candidate for spintronics[18].

Moreover, combined with superconductors, the topological insulators could realize topological superconductors[19][20][21] and lead to the creation of Majorana fermions[22][23]. Similarly to topological insulators being insulators with robust edge or surface states, the topological superconductors are superconductors with edge or surface states (the Majorana fermions) protected by topology. These Majorana fermions are fundamental particles whose existence is discussed among physicists since their proposal in 1937[24], and are fermions remarkable as they are their own antiparticle. The braiding of Majorana fermions obeys a non-abelian statistic[25] which turns very useful for quantum computing[26][27][28][29], and the proof of their realization in topological insulator/superconductor hybrid structure by Kouwenhoven *et al.* in 2012[30], even if still debated, is a milestone.

When dealing with electronic properties, transport experiments are a natural and powerful choice to classify the solids. For example, the discovery of the integer Hall effect occurred through a resistance measurement as a function of magnetic field showing plateaux.

The transport of electrons in crystals is explained by the Bloch's wave theory : the conducting electrons are submitted to a periodic potential, created by the ions on the lattice. This periodicity leads to delocalization of the electrons in the sample *via* the Bloch's theorem[31]. The Landau-Fermi liquid theory ensures that we can neglect the interaction between these electrons and the ions and between the electrons, and consider them as free particles, with a renormalized mass. The Landau-Fermi liquid theory provides results in excellent agreement with experiments for metals, even at low temperatures.

In the case of the quantum Hall effect, which is an insulating phase, transport corresponds to 1 dimensional independent channels : the edge states. We use the Landauer-Büttiker formalism to describe the transport and find the plateaux in the transverse conductance. Similarly, when the two counter-propaging edge states of the quantum spin Hall effect are independent, this formalism is still valid, and we derive the expected value of the conductances.

The case of surface states of 3 dimensional topological insulators is different because of diffusive processes : in presence of impurities, an electron with a given direction of propagation can be scattered in every direction, as opposed to the 1 dimensional case where disorder is irrelevant. This diffusive process allows for quantum interferences responsible for weak localization effect and universal conductance fluctuations[32], when in the mesoscopic regime (low concentration of impurities, small samples, low temperatures). This mesoscopic regime is the natural regime to describe transport experiments in topological insulator, thus a derivation of these quantities is needed to confront with experiments : a theoretical description relating the topological order to measured transport properties helps to understand the classification of solids.

In this thesis, I will give in the first part an introduction to the physics of topological insulators. The first chapter intends to describe the topological properties behind the quantum Hall effect, as shown by Thouless *et al.*[3]. The techniques presented in the first chapter will be adapted to the time-reversal invariant topological phases in the second chapter, following the works of Kane *et al.*[5][33][8]. Whereas these two first chapters focus on the technical side of the description of the topological insulators, the last chapter of this introduction will be a brief presentation of their experimental realizations.

The second part focuses on the two dimensional quantum spin Hall effect, and proposes an original way to probe the unique properties of the quantum spin Hall edge states by Cooper pair injection from a superconducting electrode. In particular, we show that the s-pairing of the superconductor, associated with the helicity of the edge states induces a perfect Cooper pair splitting or equivalently that the Andreev reflection is perfect at the interface between a quantum spin Hall phase and a superconductor. This quantum spin Hall effect/superconductor junction have potential applications in spintronics, or in the optics to create Majorana bound states. We also present experimental works exploiting this property. This part is an adaptation of our

paper, *Probing the helical edge states of a topological insulator by Cooper-pair injection* published in Physical Review B, **82**, 081303 (R), chosen by editor's suggestion.

The third part focuses on the transport properties of 3 dimensional topological insulators, resulting in the publication of *Diffusion at the surface of topological insulators* in New Journal of Physics, **14**, 103027 in 2012. In the case of 3 dimensional topological insulators, the surfaces states are represented as Dirac fermions, with a relativistic dispersion. Because of the impurities, the Dirac fermions are diffusive. The first chapter of this part (chapter 5) is a general derivation of the classical transport properties of Dirac fermions, using two different techniques : solving the Boltzmann equation and the standard diagrammatic technique. The chapter 6 presents the quantum interferences effects such as the weak anti-localization or the universal conductance fluctuations. In this chapter, we use the standard diagrammatic technique to derive these two quantities. We also stress the importance of the symmetry explicitly broken by the hamiltonian, showing that the values of these quantum corrections only depend on a universal symmetry class. Finally, the chapter 7 is about a special feature of the 3DTI surface states : because of the lattice geometry of the crystal, and the time-reversal symmetry, they present at high Fermi energy a hexagonal warping of the Fermi surface : the Fermi surface turns from a circle into a hexagon or a snow-flake. We study in this chapter the effects of this hexagonal warping, and show that it manifests through a dependance of the diffusion constant on the Fermi energy. We also show a dependance of the magnetic field characterizing the magnetoconductance experiments measuring the weak anti-localization correction or the amplitude of the universal conductance fluctuations. Moreover, we show that this hexagonal warping is also responsible for magnetoconductance even when the magnetic field is along the surface.

Published works

- *Probing the helical edge states of a topological insulator by Cooper-pair injection* published in Physical Review B, **82**, 081303 (R)
- *Diffusion at the surface of topological insulators* in New Journal of Physics, **14**, 103027

Part I

Introduction to topological insulators

Le suprême en ce genre est atteint quand on arrive à la quantification.

Paul Valéry, *Cahiers*

Chapter 1

The first topological insulator : the Integer Quantum Hall effect

Classical Hall effect

If we consider a metallic two dimensional sample in the xy-plane, the presence of a transverse magnetic field $\vec{B}$ along the z-axis, creates a voltage V_H in one direction when a current I_x flows along the other direction (see fig 1.1).

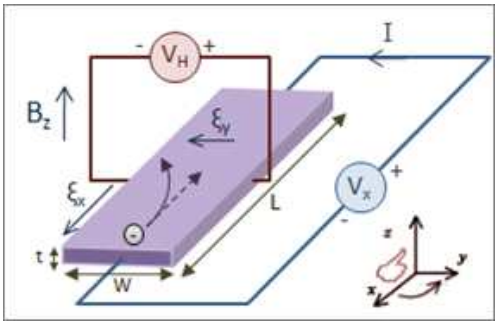

Figure 1.1: Schematic representation of an experimental setup measuring the Hall effect. A current I, provided by the voltage source V_x flows along the conductor creates a transverse voltage V_h when the magnetic field B_z is applied.

The classical Hall effect was discovered in 1879, and the underlying mechanism is simple to explain : the electric charges experience the Lorentz force from the magnetic field $q\vec{v} \times \vec{B}$ which curves their trajectories. Hence, positive charges tend to move to one side of the sample, the negative charges to the other, creating a voltage in the direction transverse to the current.

We can quantify this effect by measuring the transverse conductance, namely the ratio $\sigma_{xy} = \frac{I_x}{V_H}$. This transverse conductance is directly proportional to the magnetic field. This linearity is for example used in some teslameters to measure external magnetic fields.

1.1 Quantum Hall effect

1.1.1 The edge states

The classical Hall effect explanation is no longer valid at high magnetic field, as discovered in 1980 [2] : the transverse conductance is no longer proportional to the magnetic field for purely 2-dimensional samples (cf Fig. 1.2). To explain this, we have to use quantum mechanics[34].

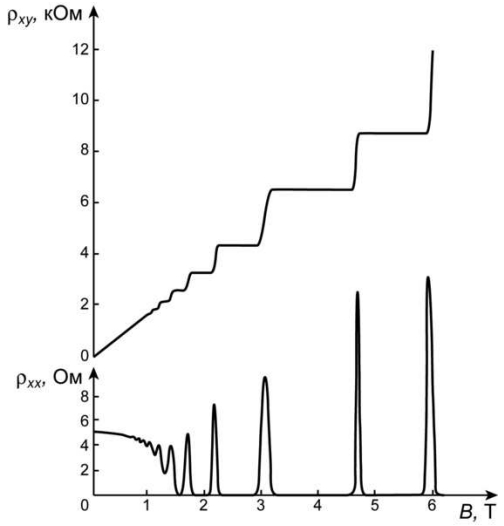

Figure 1.2: Transverse (up) and longitudinal (down) resistances as a function of the applied magnetic field B. We observe the departure of the transverse resistance from a linear model, with the presence of plateaux.

We consider a two dimensional electron gas in the x, y-plane (e.g. at the interface between two semi conductors), and use the Landau gauge for the magnetic field $\vec{A} = (-By, 0, 0)$. The Hamiltonian reads :

$$\mathcal{H} = \frac{1}{2m}\left(\left(p_x - \frac{eBy}{c}\right)^2 + p_y^2\right) + V(y)\ . \tag{1.1}$$

Because of the commutation between the Hamiltonian and the momentum along x, $[\mathcal{H}, p_x] = 0$, k_x is a conserved quantity. Consequently we look for ansatz of the form $\Psi(x, y) = e^{ikx}\xi_k(y)$, where $\omega_c = |eB|/mc$ is the cyclotron frequency associated to the magnetic field and $y_0 = -\hbar k/m\omega_c$ the eigenvalues problem reads :

$$\left(-\frac{\hbar^2}{2m}\frac{\partial^2}{\partial y^2} + \frac{m}{2}\omega_c^2\left(y - y_0\right)^2 + V(y)\right)\xi_{k,n} = E_{k,n}\xi_{k,n}\ . \tag{1.2}$$

This expression shows that in absence of the confinement potential, the two dimensional electron gas with magnetic field problem can be mapped onto

an harmonic oscillator. This mapping exhibits the presence of the so-called Landau levels, strongly degenerated states spaced by a value $\hbar\omega_c$. This gives a scale of relevant energies, and if the variations of the potential $V(y)$ are small compared to this scale of energy, we can neglect them, and thanks to the analogy with an harmonic oscillator problem, we find the solutions $E_{k,n} = \hbar\omega_c(n+1/2)$. However, near the edges of the sample, the confinement potential strongly varies which changes the energy as $E_{k,n} = E(n, \omega_c, y_0(k))$ with a typical profile plotted in Fig. 1.3.

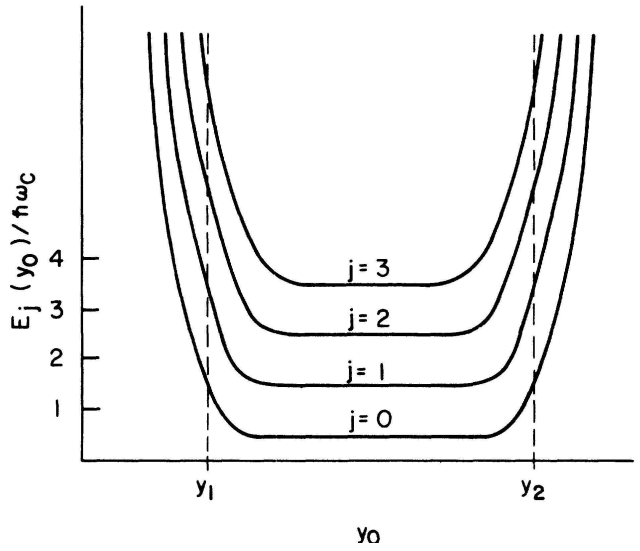

Figure 1.3: Typical profile of the confinement potential as a function of y

The profile of the energy gives the group velocity corresponding to each energy through the formula $v_{k,n} = \frac{1}{\hbar}\frac{dE_{k,n}}{dk} = \frac{1}{\hbar}\frac{dE_{k,n}}{dy_0}\frac{dy_0}{dk}$. Hence, along the lower edge y_1, the group velocity is positive, and along the upper edge y_2 it is negative. Moreover, at the center of the sample, the group velocity is zero because of the flatness of the band, so we do not observe a current flowing. This proves that only the edge states participates to electronic transport, and this can be extended to other potential profiles smooth enough (the variations of the central part of the potential should be on length scales larger than $l_B = \sqrt{h/eB}$).

At a given Fermi energy, we observe as many edge states as there are filled Landau levels.

Furthermore, we see that disorder cannot cause backscattering : a given edge state traveling with a positive velocity v cannot be backscattered with a negative velocity since the states with negative velocity are at the other edge of the sample. This spatial separation of the two edges ensures the robustness of these edge states to disorder.

In the following, we will focus on the transport properties of these robust edge states, first showing that they have a finite conductance, then explaining the presence of the plateaux in conductance measurement experiments.

1.1.2 Conductance quantification

We have just seen that electronic transport only occurs along the edges states, so to access to electric properties of the sample, we should know what is the conductance associated to each edge state. Let us first consider the case of a metal, contacted by a perfect wire to two reservoirs at the same temperature and at different chemical potentials $\mu_L = \mu_0 - \frac{eV}{2}$ et $\mu_R = \mu_0 + \frac{eV}{2}$ and calculate its conductance (we will see that it is finite). The i reservoir injects in the metal electrons at energy E according to the Fermi-Dirac distribution ($\beta_i = (k_B T_i)^{-1}$):

$$f_i(E) = \frac{1}{e^{\beta_i(E-\mu_i)} + 1} \, . \tag{1.3}$$

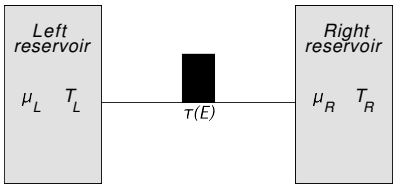

Figure 1.4: Representation of the studied single channel.

The part of the current flowing at energy E from left to right is given by the formula :

$$dI_{L\to R}(E) = \underbrace{\frac{d\rho_{L\to R}(E)}{dE}dE}_{\text{Density of states}} \quad ev(E) \quad \underbrace{\tau(E)}_{\text{transmission probability}} \quad \underbrace{f_L(E)}_{\text{injection probability}} \, . \tag{1.4}$$

However, we can deduce the velocity of the charges and the density of states from the spectrum by $v(E) = \frac{1}{\hbar}\frac{dE}{dk}$ and $\frac{d\rho_{L\to R}(E)}{dE} = \frac{1}{2\pi}\frac{dk}{dE}$, simplifying by $v(E)\frac{d\rho}{dE} = \frac{1}{h}$ and substracting the part of the current flowing from right to left :

$$\begin{aligned} I &= \int \frac{e}{h}\left[f_L(E) - f_R(E)\right]\tau(E)dE \simeq \frac{e}{h}\int -eV\tau(E) \underbrace{\frac{\partial f}{\partial E}}_{\xrightarrow[T\ll 1]{} -\delta(E-E_F)} dE \, , \\ &= \frac{e^2}{h}\tau(E_F)V \, . \end{aligned} \tag{1.5}$$

A difference between the classical world and the quantum world is seen through this simple example : even if the metal considered was perfect, the conductance could not exceed $\frac{e^2}{h}$. This paradox is lifted by remembering that we have measured the conductance of the system composed of the metal and the contacts. The contacts are responsible for the dissipation, and each counts as a $2e^2/h$ conductance.

1.1.3 Landauer-Büttiker formalism

To measure the transverse conductance of a sample, and see its quantification in the regime of quantum Hall effect, it is necessary to use a particular geometry of the conductor, named a Hall bar : because of the presence of at least 4 different contacts (2 allowing the current to flow, and 2 to measure the chemical potentials) we need to use a multiterminal formalism.

The formalism to describe the conductivity of a multiterminal device, where the terminal are connected by independant channels is known as the Landauer-Büttiker formalism.

In this formalism, each channel is characterized by its conductance $\tau(E)e^2/h$, and we express the the current flowing from the lead α to the device as a function of the potential of each lead through the conductance matrix G as :

$$I_\alpha = \sum_\beta G_{\alpha\beta} V_\beta \ . \tag{1.6}$$

The matrix coefficient $G_{\alpha\beta}$ is the sum of all the conductances $\tau(E)e^2/h$ of each channel connecting the lead α to the lead β. The conductance matrix is constrained by Kirchoff's laws, as $\sum_\beta G_{\alpha\beta} = 0$ to ensure the conservation of the charge, and $\sum_\alpha G_{\alpha\beta} = 0$ because the potentials are defined up to an additive constant. The coefficient on the diagonal $G_{\alpha\alpha}$ are the number of conducting channels going out of the lead α times the quantum of conductance $G_{\alpha\alpha} = n_\alpha e^2/h$, and, in the case of perfectly transmitted channels, the non diagonal coefficients $G_{\alpha\beta}$ are the opposite of the number of channels coming from the lead β to the lead α : $G_{\alpha\beta} = -n_{\beta\alpha} e^2/h$.

In the case of n edge states in the quantum Hall effect, then this matrix is made out of n on the diagonal, and $-n$ just behind the diagonal, for example in a 6-terminals device :

$$G^{QHE} = \frac{e^2}{h} \begin{pmatrix} n & 0 & 0 & 0 & 0 & -n \\ -n & n & 0 & 0 & 0 & 0 \\ 0 & -n & n & 0 & 0 & 0 \\ 0 & 0 & -n & n & 0 & 0 \\ 0 & 0 & 0 & -n & n & 0 \\ 0 & 0 & 0 & 0 & -n & n \end{pmatrix} . \tag{1.7}$$

We want to invert this conductance matrix as we constrain the current vector I_α and look for the potential vector V_β, but the determinant of the

conductance matrix vanishes because of the Kirchoff's law. This problem is solved by considering that the information on one lead is already provided by the other leads : if we take the 6th lead in the previous example, we can measure all the potentials with respect to V_6, and the current through this lead is $I_6 = -\Sigma_{\alpha=1}^{5} I_\alpha$. With this simplification the problem can be inverted as :

$$\begin{pmatrix} V_1 - V_6 \\ V_2 - V_6 \\ V_3 - V_6 \\ V_4 - V_6 \\ V_5 - V_6 \end{pmatrix} = \frac{h}{e^2} \begin{pmatrix} 1/n & 1/n & 1/n & 1/n & 1/n \\ 0 & 1/n & 1/n & 1/n & 1/n \\ 0 & 0 & 1/n & 1/n & 1/n \\ 0 & 0 & 0 & 1/n & 1/n \\ 0 & 0 & 0 & 0 & 1/n \end{pmatrix} \begin{pmatrix} I_1 \\ I_2 \\ I_3 \\ I_4 \\ I_5 \end{pmatrix} . \tag{1.8}$$

Solving the problem for the quantum Hall effect in this 6 terminal geometry is then performed by imposing the current vector. In the example of Fig. 1.5, we impose $I_1 = -I_4 = I$, $I_2 = I_3 = I_5 = I_6 = 0$, and we observe that $V_1 = V_2 = V_3 = \frac{h}{ne^2} I$ and $V_4 = V_5 = V_6 = 0$.

The calculation of the transverse conductance $G_H = \frac{V_2 - V_5}{I}$ shows the conductance quantification and the plateaux $G_H = ne^2/h$.

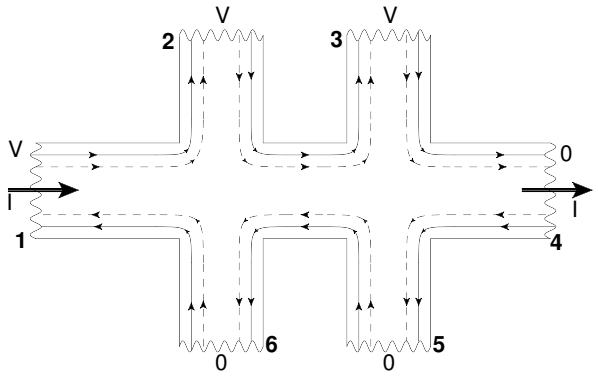

Figure 1.5: Schematic representation of the six-terminal measurement in the quantum Hall regime with two filled Landau levels.

We also observe equipotentials along the edge, with no loss of the potential, as expected from the absence of backscattering.

We have seen that the conductance plateaux observed in the quantum Hall effect are a property arising from the edges of the 2 dimensional sample regardless of its size or shape or even the disorder of the sample. The branch of mathematics that concerns a property independent of "deformations" is topology, and it seems natural to see if this conductance quantification is not related to a topological property of the quantum Hall effect. This is what we aim to do in the rest of this chapter.

1.2 Topology and Quantum Hall effect

1.2.1 Topology

Topology is the branch of mathematics that tries to attribute properties to mathematical objects that do not depend on the metric, the way how the length between two points is measured. The first example of a topological problem was the resolution of the Seven Bridges of Königsberg by Euler. The problem is the following : is it possible to do a walk in the town by crossing every bridge of the city only once ? The solution appeared obvious when Euler considered the problem as shown in the Fig. 1.6 : when the problem is shown in the graph form, all you need to do is to count the number of vertices of the graph connected to an odd number of edges (if this number is 3 or more, then there is no solution).

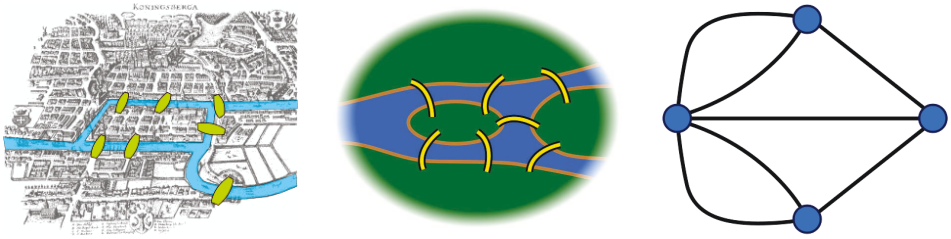

Figure 1.6: The Seven Bridges of Königsberg problem, and the graph resolution to solve it.

This problem does not depend on the size or the shape of the different part of the city, this is what the deformation to a graph shows, and the same result is expected for two different cities that can be mapped into the same graph : this is why topology is also defined as the science of global properties, or also as the invariant properties with respect to smooth deformations.

1.2.1.1 Genus of closed surfaces

Another topology problem that will help us to understand to what extend these insulators are topological is the problem of the classification of closed surfaces in 3 dimensions. For example, a football ball can be smoothly deformed into a rugby ball, or even a flying disc by squishing it, but it is impossible to turn it into a torus without cutting and glueing it. The definition of what is a "smooth" deformation needs to be precised, but in this context of closed surface, we will require the impossibility to cut or glue it. In this case, one way to characterize the different kinds of surfaces would be to deform them into polyhedra and calculate their corresponding Euler characteristic $\chi = v - e + f$ where v (resp. e and f) is the number of vertices (resp. edges and faces) of the polyhedron. For example, both the rugby ball and the football ball can

be deformed into a cube or a tetrahedron, but the calculation of their Euler characteristic gives the same value : for a cube $\chi = 8 - 12 + 6 = 2$, for a tetrahedron $\chi = 4 - 6 + 4 = 2$. The same calculation can be done for all the platonician solids, and even for the different polyhedra the sphere can be turned into : to be accurate, a football is actually a truncated icosahedron, with 12 pentagonal and 20 hexagonal faces, 90 edges and 60 vertices, and thus the same Euler characteristic $\chi = 2$. This characteristic does not depend on the particular deformation, since the fusion of a two vortices will decrease both the number of vertices and edges by one, and similarly, the suppression of a given edge will decrease both the number of edges and faces by one.

However, the torus can not be deformed into the same class of polyhedra, but it can be turned into the two pictured in Fig. 1.7. For the cubic toroid, one finds that $\chi = 32-64+32 = 0$, and for the hexagonal one $\chi = 24-48+24 = 0$.

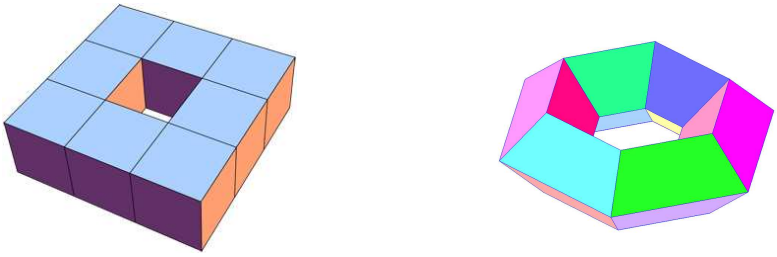

Figure 1.7: Two toroidal polyhedra, left the cuboid one, right the hexagonal one.

Intuitively, there is a generalization of the Euler characteristic in the case of a polyhedron : we can see that the difference between the toroidal polyhedra and the platonician solids is the number of holes, and the relation between the Euler characteristic and the number of holes g, called the genus is $\chi = 2 - 2g$. This intuitive manner to classify the surfaces by their gender is very convenient, since it is a generalization to surfaces that are not polyhedra, but we need a more rigorous approach to calculate the number of holes. A mathematical theorem helps us to define it more precisely : the Gauss-Bonnet theorem which states that for a closed surface $\mathcal{S}$:

$$\chi = \frac{1}{2\pi} \int_{\mathcal{S}} K dS \, , \tag{1.9}$$

where K is the local curvature. We can foresee its importance for our study of topological insulators, because it relates a global property to a local geometry. We will provide other examples of this relation when studying the topological order of topological insulators.

In the case of a sphere of radius R, the curvature is constant and equal to $1/R^2$, so $\chi = 2$ as previously calculated. In the case of the torus, it can be identified with a flat square whose sides are identified one with another, and because of the flatness of the square $K = 0$, so we find that $\chi = 0$.

1.2.2 Quantum Hall effect as a topological insulator

We have just seen that the edge states of a quantum Hall effect are the relevant states to describe its electric properties. Indeed, the number n of filled Landau levels does not depend on small changes of the Hamiltonian, such as disorder, profile of the confinement potential, etc... The transverse conductance ne^2/h appears to be a global property independent of "deformations" of the Hamiltonian[35] : in this section we intend to show that there is a sublying topology that explain this behavior.

To have a better understanding of the quantum Hall effect, it could be useful to picture what happens in a semi-classical way, where electrons follow circles of radius $l_B = \sqrt{\hbar/eB}$. At the center of the sample, they do not participate to electric current ; at the edges the electrons bounce and participate to current. The bigger the magnetic field, the higher the Landau level spacing, and the fewer the edge states.

The presence of an impurity will not affect the transport since it could change the trajectory of the electrons on a scale l_B, if the other edge is far enough, each incoming electron on the impurity has to leave on the same edge, with same velocity : there is no loss of chemical potential along the edges. Similarly, even in the case of non perfectly flat edges, the concerned electrons will still bounce (provided that the potential variations occur on a length scale bigger than l_B).

This robustness of the number of edge states seems very similar to the robustness of the Euler characteristic, this is the idea that led Thouless, Kohmoto, Nightingale and den Nijs [3][36] to look for a topological invariant characterizing the quantum Hall effect[37][38]. It was later shown by Hatsugai[4] that the topological invariant they propose in the case of an infinite sample, with no edge, is equivalent to the number of edge states for finite samples.

For a 2-dimensional gas of non-interacting electrons, in presence of a periodic potential $U(x, y)$ and a constant magnetic field, the Hamiltonian is written as :

$$\mathcal{H} = \frac{1}{2m}\left(\vec{p} + e\vec{A}\right)^2 + U(x, y) \ . \tag{1.10}$$

We assume that the periodicity of the potential $U(x, y)$ in x and y is given by $U(x + a, y) = U(x, y + b) = U(x, y)$. The system is invariant under translations of a in the direction x and b in the direction y, but because of the presence of the potential vector, the Hamiltonian is not. We introduce the magnetic translation operators as :

$$\hat{T}_{\vec{R}} = \exp\left[(i/\hbar)\vec{R}.\left(\vec{p} + e\vec{A}\right)\right] \ . \tag{1.11}$$

If we choose the symmetric gauge for the potential vector $\vec{A} = (B_z y/2, -B_z x/2, 0)$, the Hamiltonian commutes with $\hat{T}_a$ and $\hat{T}_b$. The product

of 4 magnetic translation operators corresponds to move around a loop, thus :

$$\hat{T}_a^{-1}\hat{T}_b^{-1}\hat{T}_a\hat{T}_b = e^{i2\pi\phi} \,, \tag{1.12}$$

where $\phi = (eB_z/h)ab$ is the magnetic flux through the unit cell of size a and b. If this flux is an integer[1], then the Eq. (1.12) simplifies as $\hat{T}_a\hat{T}_b = \hat{T}_b\hat{T}_a$: the two magnetic translation operators commute.

If ψ is an eigenfunction that diagonalizes simultaneously $\mathcal{H}$, $\hat{T}_a$ and $\hat{T}_b$, the eigenvalues of the magnetic translation operators are given by :

$$\hat{T}_a\psi = e^{ik_x a}\psi \,, \tag{1.13}$$
$$\hat{T}_b\psi = e^{ik_y b}\psi \,, \tag{1.14}$$

where k_x and k_y are generalized crystal momenta and are restricted to the Brillouin zone of length $2\pi/a$ and $2\pi/b$. Since k_x and k_y are conserved quantities, the starting Hamiltonian of Eq. (1.10) can be written as :

$$\mathcal{H}(\vec{k}) = \frac{1}{2m}\left(-i\hbar\vec{\nabla} + \hbar\vec{k} + e\vec{A}\right)^2 + U(x,y) \,, \tag{1.15}$$

where $\vec{k}$ is the vector of components k_x and k_y, $\vec{A}$ is the potential vector and $U(x,y)$ is a periodic potential. The Bloch states corresponding to this Hamiltonian $u^{\alpha}_{k_x k_y}$ are defined on the Brillouin zone such that :

$$\mathcal{H}(\vec{k})u^{\alpha}_{k_x k_y} = E^{\alpha}(\vec{k})u^{\alpha}_{k_x k_y} \,. \tag{1.16}$$

When $\vec{k}$ is varied through the Brillouin zone, the eigenvalue E^{α} varies continuously, for a given α index, this forms a dispersion band. The eigenstates are normalized as $\int_{UC} dxdy|u|^2 = 1$ where $\int_{UC}$ denotes the integration over a unit cell.

In the quantum Hall regime,we apply a small electric field to flow a current in the sample and the transverse conductivity is derived by a linear response theory through the Kubo formula :

$$\sigma_{xy} = \frac{e^2\hbar}{i}\sum_{E^{\alpha}<E_F<E^{\beta}} \frac{(v_y)_{\alpha\beta}(v_x)_{\beta\alpha} - (v_x)_{\alpha\beta}(v_y)_{\beta\alpha}}{(E^{\alpha}-E^{\beta})^2} \,, \tag{1.17}$$

where E_F is the Fermi energy and $\vec{v}$ is the velocity operator $\vec{v} = (-i\hbar\vec{\nabla} + e\vec{A})/m$. The matrix elements $v_{\alpha\beta}$ are integrated over a unit cell :

$$(\vec{v})_{\alpha\beta} = \delta_{k_x k'_x}\delta_{k_y k'_y}\int_{UC} dxdy \quad (u^{\alpha}_{k_x k_y})^* \; \vec{v} \; u^{\beta}_{k'_x k'_y} \,. \tag{1.18}$$

[1]In the more general case where this flux is a rational, we can turn it into an integer by multiplication of the lattice vectors.

Since the Kubo formula takes into account only off diagonal matrix elements (α states are below Fermi energy whereas β states are above), it is possible to write these matrix elements as a partial derivatives of the $\vec{k}$-dependant Hamiltonian :

$$(v_i)_{\alpha\beta} = \frac{1}{\hbar}\langle\alpha|\partial_{k_i}\mathcal{H}(\vec{k})|\beta\rangle \ , \qquad i = x, y \ , \tag{1.19}$$

$$= \frac{E^\beta - E^\alpha}{\hbar}\langle\alpha|\partial_{k_i}u^\beta\rangle = -\frac{E^\beta - E^\alpha}{\hbar}\langle\partial_{k_i}u^\alpha|\beta\rangle \ . \tag{1.20}$$

Inserting the result of Eq. (1.20) into the Kubo formula Eq. (1.17) gives :

$$\sigma_{xy} = \frac{e^2}{i\hbar}\sum_{E^\alpha<E_F<E^\beta}\left(\langle\partial_{k_y}u^\alpha|\beta\rangle\langle\beta|\partial_{k_x}u^\alpha\rangle - \langle\partial_{k_x}u^\alpha|\beta\rangle\langle\beta|\partial_{k_y}u^\alpha\rangle\right) \ . \tag{1.21}$$

As we assumed the Fermi energy is in a gap between two bands, we use the closure relation $\sum_{E^\alpha<E_F<E^\beta}\left(|\alpha\rangle\langle\alpha| + |\beta\rangle\langle\beta|\right) = Id$ to write $\sigma_{xy} = \sum_{E^\alpha<E_F}\sigma^\alpha_{xy}$ where :

$$\sigma^\alpha_{xy} = \frac{e^2}{h}\frac{1}{2\pi i}\int_{BZ}d\vec{k}\int_{UC}d\vec{r} \quad \partial_{k_y}(u^\alpha)^* \ \partial_{k_x}u^\alpha \ - \ \partial_{k_x}(u^\alpha)^* \ \partial_{k_y}u^\alpha \ , \tag{1.22}$$

where $\int_{BZ}$ is the integration over the Brillouin zone, and σ^α_{xy} is the contribution of each filled band to the Hall conductivity.

Introducing the Berry connection :

$$\vec{\mathcal{A}}(\vec{k}) = -i\int_{UC}d\vec{r} \quad u^*_{k_xk_y} \ \vec{\nabla}_{\vec{k}} \ u_{k_xk_y} = i\langle u_{k_xk_y}|\vec{\nabla}_{\vec{k}}|u_{k_xk_y}\rangle \ , \tag{1.23}$$

where the vector $\vec{\nabla}_{\vec{k}}$ is the vector of components ∂_{k_x} and ∂_{k_y} we can express the Hall conductivity of the α band as :

$$\sigma^\alpha_{xy} = \frac{e^2}{h}\frac{1}{2\pi}\int_{BZ}d\vec{k}\left[\vec{\nabla}_{\vec{k}}\times\vec{\mathcal{A}}(\vec{k})\right]_z \ . \tag{1.24}$$

The Berry connection $\vec{\mathcal{A}}$ corresponds to the linear transport of the information on the phase when moving on the torus forming the Brillouin zone, this is why it is called a connection. Let us see where this parallel transport comes from with a simple example. Let us take a general Hamiltonian H_λ depending on a parameter λ and corresponding eigenstates $|\psi;\lambda\rangle$. Then if we adiabatically change the value of the parameter λ in time, the evolution of the eigenstates will be given by :

$$H_{\lambda(t)}|\psi(t);\lambda(t)\rangle = i\partial_t|\psi(t);\lambda(t)\rangle \ . \tag{1.25}$$

Solving this equation shows that the eigenstate acquires a phase γ called the Berry phase during the evolution namely :

$$|\psi(t)\rangle = e^{i\gamma} \exp\left(-i \int_0^t E(s)ds\right) |\psi; \lambda(t)\rangle \ , \tag{1.26}$$

$$\gamma = i \int_0^t \langle \psi; \lambda(s)|\partial_s|\psi; \lambda(s)\rangle ds \ . \tag{1.27}$$

Applying this result to a change of the parameter $\vec{k}$ in the Hamiltonian $\mathcal{H}(\vec{k})$ of eigenstates $u_{k_x k_y}$ shows the link between parallel transport and the Berry connection $\vec{\mathcal{A}}$ we calculated. If we define the Berry curvature associated to this connection on the torus of the Brillouin zone as $\mathcal{F}(\vec{k}) = \vec{\nabla}_{\vec{k}} \times \vec{\mathcal{A}}(\vec{k})$, we observe that the equation Eq. (1.24) simplifies as :

$$\sigma_{xy}^{\alpha} = n_\alpha \frac{e^2}{h} \ , \tag{1.28}$$

$$n_\alpha = \frac{1}{2\pi} \int_{BZ} d\vec{k} \mathcal{F}(\vec{k}) \ . \tag{1.29}$$

The quantity n_α is quantified, in the same way as the Euler characteristic is for the classification of closed surfaces.

Precisely, we are studying the geometric object formed by the eigenstates $u(\vec{k})$ for each point $\vec{k}$ of the torus of the Brillouin zone, each eigenstate being defined up to a phase factor : this structure is known as a *fiber bundle*. A simple image of a fiber bundle is a Möbius strip (combination of a circle and a fiber). In each point of the circle, the Möbius strip looks like any regular piece of paper, similarly, the fiber bundle we are studying is locally similar to the product of a portion of the Brillouin zone and of the phase associated to each point. This phase is not of importance if we only look for local properties, but its importance is capital to topology : you can distinguish a Möbius strip from a simple cylinder only if you look at the whole strip of paper.

The Brillouin zone is a 2 dimensional torus, and Chern showed[39] that there is n topological invariants associated to every fiber bundle constructed upon a 2n dimensional orientable manifold. In our case, the only topological invariant is an integer named the first Chern number and is defined as n_α in Eq. (1.29).

In analogy with the closed surfaces classification of Sec. 1.2.1.1 where we have seen that we can deform a football ball without changing the Euler characteristic, this Chern number can not be modified by "smooth" deformation. The action corresponding to cut or glue surfaces will be any action on the Hamiltonian that closes the gap, as this derivation holds only for insulators.

We deduce from Eq. (1.28) the quantification of the Hall conductance. This expression also shows that the Hall conductivity does not depend on any choice

of the phase : if we change all the eigenstates $u_{k_xk_y}$ by a $\vec{k}$-dependant phase $u'_{k_xk_y} = u_{k_xk_y}e^{i\phi_k}$, then the Berry connection is modified as $\vec{\mathcal{A}}' = \vec{\mathcal{A}} + \vec{\nabla}\phi_k$ but the Berry curvature is not $\mathcal{F}' = \mathcal{F}$.

1.2.3 Haldane model

1.2.3.1 Introduction of the model

To see how this Chern invariant can be derived, but also in order to introduce more easily the $\mathbb{Z}_2$ topological insulators, we now study a theoretical model introduced by Haldane where a quantum Hall phase appears in the absence of a net magnetic field. This model consists in spinless electrons on a honeycomb lattice (e.g. graphene). A honeycomb lattice consists of two triangular sublattices labeled A and B, where we develop the states on each of the sublattice $|\psi\rangle = \begin{pmatrix} \psi_A \\ \psi_B \end{pmatrix}$. The different terms in the Hamiltonian are (see Fig.1.8) :

- nearest neighbor hopping t connecting two sites of the different sublattices A and B ;
- next-nearest neighbor hopping t' connecting two sites of the same sublattice A or B ;
- a term breaking the symmetry between the two sublattices $+M$ on the A sublattice, $-M$ on the B sublattice. This symmetry is known as the parity symmetry ;
- finally a local magnetic field is added in such a way that the flux through an unit cell vanishes. This can be done by assuming that the nearest neighbor hopping coefficient is real and the next nearest neighbor hopping coefficient acquires a phase $t' = t_2 e^{\pm i\Phi}$.

We introduce the vectors $\vec{a_i}$ that connect the B sites to the A sites, and the lattice vectors $\vec{b_i}$ that represent the displacement on the same sublattice. If we express the states as a two-component spinor acting on the A and B sublattices, the Hamiltonian reads :

$$\begin{aligned}\mathcal{H}(\vec{k}) =& 2t_2\cos\Phi\left(\sum_{i=1}^{3}\cos(\vec{k}.\vec{b_i})\right)Id + t\left(\sum_i\left[\cos(\vec{k}.\vec{a_i})\sigma^x + \sin(\vec{k}.\vec{a_i})\sigma^y\right]\right)\\ &+\left[M - 2t_2\sin\Phi\left(\sum_{i=1}^{3}\sin(\vec{k}.\vec{b_i})\right)\right]\sigma^z\ . \end{aligned} \tag{1.30}$$

This Hamiltonian can be written as $\mathcal{H}(\vec{k}) = h_0(\vec{k})Id + \vec{h}(\vec{k}).\vec{\sigma}$, and this expression shows that the 2 energy bands only touch when $\vec{h}(\vec{k}) = \vec{0}$. Focusing only on the first two components of the vector $\vec{h}(\vec{k})$ this can only occur

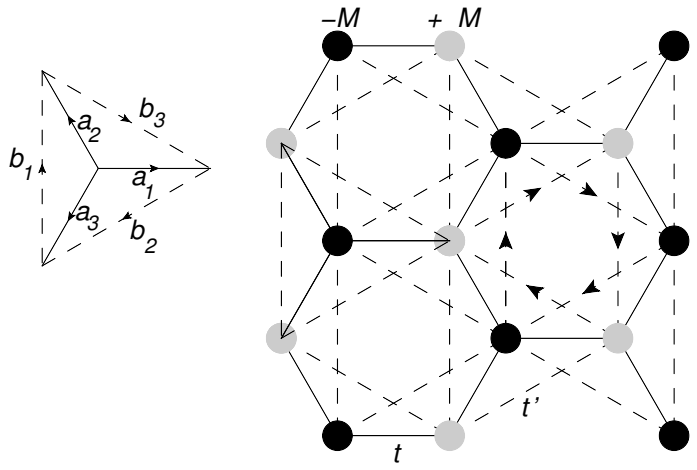

Figure 1.8: Haldane model for the honeycomb lattice. The parity breaking term $\pm M$ is shown, as the hopping coefficients. On the right cell, the arrows indicate the hopping terms with a positive phase $t' = t_2 e^{i\Phi}$. The lattice vectors a_i and b_i are also shown.

at the corners of the Brillouin zone, where $\vec{k}.\vec{a_1}, \vec{k}.\vec{a_2}, \vec{k}.\vec{a_3}$ take the values $0, +2\pi/3, -2\pi/3$. When in these corners, the third component of the vector is zero only if $M = \pm 3\sqrt{3} t_2 \sin\Phi$.

We will assume that $|t_2/t| \leq 1/3$ so that the two energy bands never cross the same energy unless when they touch.

Since we are interested in topological invariants, when the condition $M = \pm 3\sqrt{3} t_2 \sin\Phi$ is not satisfied, we can change the Hamiltonian as long we do not close the gap. For example, we can get rid of the h_0 term which is just a shift of the two energy bands. We can also change the value of $|\vec{h}|$ so it is constant and equal to 1 everywhere in the Brillouin zone since it just corresponds to varying the gap between the two energy bands.

1.2.3.2 Diagonalization of the Hamiltonian and topology

With these modifications, the Hamiltonian now reads :

$$\mathcal{H}(\vec{k}) = \vec{h}(\vec{k}).\vec{\sigma} \, , \tag{1.31}$$

where $\vec{h}$ is on the Bloch sphere, and can be labeled by the azimuthal and polar angles $\theta(\vec{k})$ and $\phi(\vec{k})$ so that $(h_x, h_y, h_z) = (\sin\theta\cos\phi, \sin\theta\sin\phi, \cos\theta)$. The diagonalization is straightforward and gives the two eigenvalues ± 1 with corresponding eigenstates :

$$|u_-^{(N)}(\vec{k})\rangle = \begin{pmatrix} \sin(\theta/2) e^{-i\phi} \\ -\cos(\theta/2) \end{pmatrix} \quad ; \quad |u_+^{(N)}(\vec{k})\rangle = \begin{pmatrix} \cos(\theta/2) \\ \sin(\theta/2) e^{i\phi} \end{pmatrix} . \tag{1.32}$$

The superscript (N) stands for north pole, because we have chosen this particular point to define what is the azimuthal angle. The problem with this choice of the eigenstates is that there is a non physical ambiguity at the south pole where $\theta = \pi$, as the polar angle ϕ is not defined ; in most of the cases, this is solved by considering a different expression for the eigenstates, for example we can introduce :

$$|u_-^{(S)}(\vec{k})\rangle = \begin{pmatrix} \sin(\theta/2) \\ -\cos(\theta/2)e^{i\phi} \end{pmatrix} \quad ; \quad |u_+^{(S)}(\vec{k})\rangle = \begin{pmatrix} \cos(\theta/2)e^{-i\phi} \\ \sin(\theta/2) \end{pmatrix} . \quad (1.33)$$

The two bands are well separated by a gap of value 2, and we know that we need to calculate the Chern numbers only for the filled bands : in this model, this corresponds to focus only on the $|u_-\rangle$ band.

During the calculation of the integral of its Berry curvature, two cases must be distinguished.

In the first one, one of the points on the Bloch sphere is never reached when $\vec{k}$ is moved along the Brillouin zone, for example the south pole. In this case, no problem appears by taking the eigenstates $|u_-^{(N)}\rangle$ for all the states, and the integral of the curvature on all the Brillouin zone reduces to zero : there is no quantum Hall effect. It can be seen as the fact that we are not sensitive to the topological singularity, just as a portion of a Möbius strip looks totally similar to a portion of a non twisted strip.

The second case is when all of the Bloch sphere is spanned when $\vec{k}$ described the whole Brillouin zone : in this case the singularity at the south pole can not be ignored. The presence of this singularity is an *obstruction* to a single definition of the phase on all the space.

To treat it properly, we need to cut our Bloch sphere in two halves, and define the eigenstates with the convention $|u_-^{(N)}\rangle$ (resp. $|u_-^{(S)}\rangle$) on the northern (resp. southern) hemisphere. It is possible to use the mapping $\vec{h}$ to change the variables of integration from the $\vec{k}$ in the Brillouin zone to the θ, ϕ labeling the direction of $\vec{h}(\vec{k})$, and introducing the number of times n_w this vector $\vec{h}$ winds around all the sphere ($n_w = 0$ in the previous case), the calculation of the Chern number is then given by :

$$n = \frac{1}{2\pi}\int_{BZ} d\vec{k}\mathcal{F}(\vec{k}) = \frac{n_w}{2\pi}\int_{\text{Bloch sphere}} d\theta d\phi \mathcal{F}(\theta,\phi) . \quad (1.34)$$

The integral on the whole Bloch sphere is then done by integrating on each hemisphere, and using the Stokes theorem, the integral of the Berry curvature on each hemisphere gives the integral of the Berry connection along the equator :

$$n = \frac{n_w}{2\pi}\int_{\theta=\pi/2} (\vec{\mathcal{A}_N} - \vec{\mathcal{A}_S}).d\vec{l} . \quad (1.35)$$

However, we have derived in the subsection 1.2.2 that a change of the phase for all the eigenstates $u'_{k_x k_y} = u_{k_x k_y} e^{i\phi_k}$ changes the Berry connection as $\vec{\mathcal{A}}' = \vec{\mathcal{A}} + \vec{\nabla}\phi_k$ and in this case we know that $|u_-^{(N)}\rangle = e^{-i\phi}|u_-^{(S)}\rangle$ and this gives :

$$n = n_w \ . \tag{1.36}$$

1.2.3.3 Resolution of the Haldane model

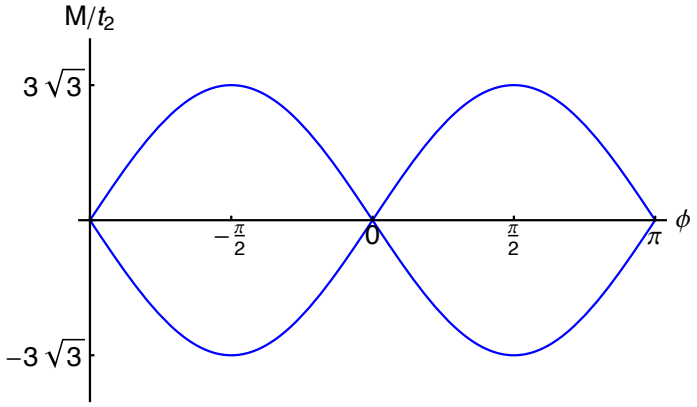

Figure 1.9: Phase diagram of the Haldane model as a function of the parameters M/t_2 and ϕ. Along the blue lines, the gap closes, allowing for a topological phase transition.

We want to precise the phase diagram of Fig. 1.9, where the Chern number is defined as a function of the parameters M/t_2 and ϕ. It is not necessary to calculate the Chern number for all values of the coefficients M/t_2 and ϕ since we know that the gap never closes outside of the blue lines. This means that the Chern number can not change away from the blue lines : we have only three Chern numbers to determine. Moreover, the operation $\phi' = -\phi$ corresponds to the flipping of the magnetic field, so we should have $n(-\phi) = -n(\phi)$ because these numbers gives the Hall conductivity in units of e^2/h. In conclusion, outside of the two lobes, $n = 0$, and we only need to calculate n for a positive value of ϕ.

We can calculate directly the Chern number :

$$n = \frac{1}{2\pi} \int_{BZ} d\vec{k} \mathcal{F}(\vec{k}) \ . \tag{1.37}$$

In the case where the Hamiltonian is defined as $\mathcal{H}(\vec{k}) = \vec{h}(\vec{k}).\vec{\sigma}$, with $\vec{h}$ on the Bloch sphere, the calculation of the Berry curvature reduce to a simpler value and the Chern number reads :

$$n = \frac{1}{4\pi} \int_{BZ} \vec{h}.\left(\partial_{k_x}\vec{h} \times \partial_{k_y}\vec{h}\right) \ . \tag{1.38}$$

For $\phi = \pi/2$ and $t_2 = t_1/4$, we calculated this Chern number and found that for $M = 0$, $n = 1$, and for $M = 8t_2$, we found $n = 0$, as expected. The final diagram phase is plotted in Fig. 1.10.

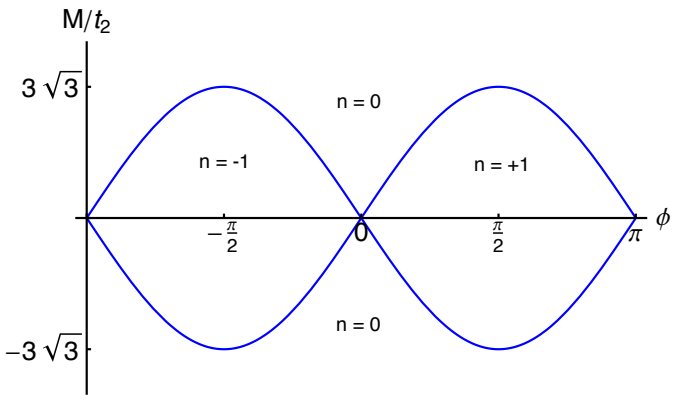

Figure 1.10: Final phase diagram of the Haldane model as a function of the parameters M/t_2 and ϕ, where we have indicated the value of the Chern number in each domain.

Le temps ne fait rien à l'affaire.

Georges Brassens

Chapter 2

Time reversal invariance and topological order

2.1 Towards two-dimensionnal topological insulators : graphene and spin-orbit coupling

2.1.1 The Quantum Spin Hall Effect

Graphene is a two-dimensional crystal consisting of a honeycomb lattice of carbon atoms [6]. As pictured in Fig. 1.8, it consists of two triangular sublattices labeled A and B, and with a lattice model where we develop the states on each of the sublattice $|\psi\rangle = \begin{pmatrix} \psi_A \\ \psi_B \end{pmatrix}$. Adding a nearest neighbor hopping t we obtain the Hamiltonian :

$$\mathcal{H}_0 = t \sum_{\langle i,j \rangle} c_i^\dagger c_j = \sum_{\vec{k}} \mathcal{H}(\vec{k}) \ , \tag{2.1}$$

where we defined :

$$\mathcal{H}(\vec{k}) = t \left(\sum_i \left[\cos(\vec{k}.\vec{a_i})\sigma^x + \sin(\vec{k}.\vec{a_i})\sigma^y \right] \right) \ . \tag{2.2}$$

The dispersion relation plotted in Fig. 2.1 shows the Dirac cones with a linear dispersion $E = \hbar v_F k$ at the corners of the Brillouin zone, and because of the triangular lattice structure, there are only two independant cones labeled $\vec{K}$ and $\vec{K'} = -\vec{K}$. The corresponding degeneracy is called the valley degeneracy, and we account for this degeneracy with a second Pauli matrix τ where $\tau^z = \pm 1$ corresponds to momentum located near one or the other of the valleys $\vec{K}$ or $\vec{K'}$. The effective Hamiltonian is obtained by expanding Eq. (2.2) around $\vec{K}$ and $\vec{K'}$:

$$\mathcal{H}_{eff} = -i\hbar v_F \left(\sigma^x \tau_z \partial_x + \sigma^y \partial_y \right) \ , \tag{2.3}$$

where ψ is a four components spinor, describing the valley and the sublattice degeneracy.

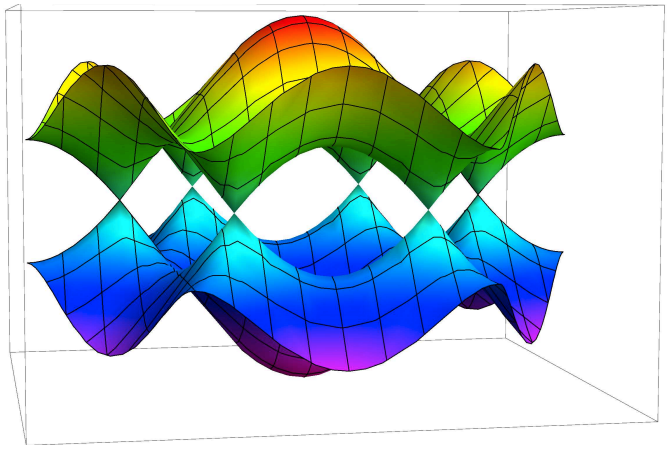

Figure 2.1: Dispersion relation of the graphene. The first Brillouin zone consists of the hexagon formed by the six cones where the two bands touch each other.

As we will see in Sec. 3.0.3, the introduction of spin-orbit coupling [40][5] allows a new term in the Hamiltonian that do not break time-reversal invariance nor parity :

$$\mathcal{H}_{SO} = \Delta_{SO}\sigma^z\tau^z s^z \ . \tag{2.4}$$

In this expression, the spin-orbit coupling preserves the electron spin's on the z-axis s^z to be a good quantum number. In this case, it is possible to separate electrons into up and down spins. We treat this spin-orbit coupling by introducing a tight binding model : we add to the next-nearest hopping term t of the kinetic Hamiltonian $\mathcal{H}_0$ a new term :

$$\mathcal{H} = \sum_{\langle ij\rangle\alpha} t c^\dagger_{i\alpha} c_{j\alpha} + \sum_{\ll ij\gg\alpha\beta} i t_2 \nu_{ij} s^z_{\alpha\beta} c^\dagger_{i\alpha} c_{j\beta} \ . \tag{2.5}$$

The $\langle ij\rangle$ (resp. $\ll ij \gg$) represents nearest (resp. next nearest) neighbor pairs. We check that the spin s^z is conserved by the second term ; it also preserves τ^z and σ^z. The term $\nu_{ij} = -\nu_{ji} = \pm 1$ depends on the orientation of the two nearest neighbor bonds connecting the site i to site j. ν_{ij} takes the value $+1$ (resp. -1) when the electron has to do a clockwise (resp. anticlockwise) turn. To be consistent with Eq. (2.4) at low energies, $t_2 = \Delta_{SO}/3\sqrt{3}$.

This tight-binding model is equivalent to the Haldane model of Eq. (1.30) where the parameters are defined as $M = 0$, $\phi = \pm\pi/2$ depending on the value of the spin s^z. In this case, we can define a Chern number for each value of s^z, $n_\uparrow$ and $n_\downarrow$. From the calculation of Sec. 1.2.3, we deduce that $n_\uparrow = -n_\downarrow = 1$

(up to a sign that is not relevant). The total Chern number, as it is the sum of all the filled bands $n_\uparrow + n_\downarrow$, vanishes : as expected, because we do not break the time-reversal symmetry, we can not see quantum Hall effect. However, this phase differs from a trivial insulator as it presents two edge states of opposite spins and counterpropaging (cf.Fig 2.2).

In comparison to the quantum Hall phase, if we perform a four-terminal terminal experiment to measure the transverse conductance, we obtain $\sigma_H = 0$ since the transverse voltage V_H vanishes by symmetry. However, we can measure the transverse spin voltage $V_{H,\uparrow} - V_{H,\downarrow}$ since the edge states are counterpropaging for opposite spins. Reciprocally, when we bias two leads with a potential V, we obtain a transverse spin current I_s (and not a charge current) flowing between the two other leads (cf Fig. 2.3). The associated transverse spin conductance is quantified as $I_s/V = e/(2\pi)$. However, we can not measure the specificity of this topological phase by measuring the transverse spin conductance as spin currents do not couple to experimental probes.

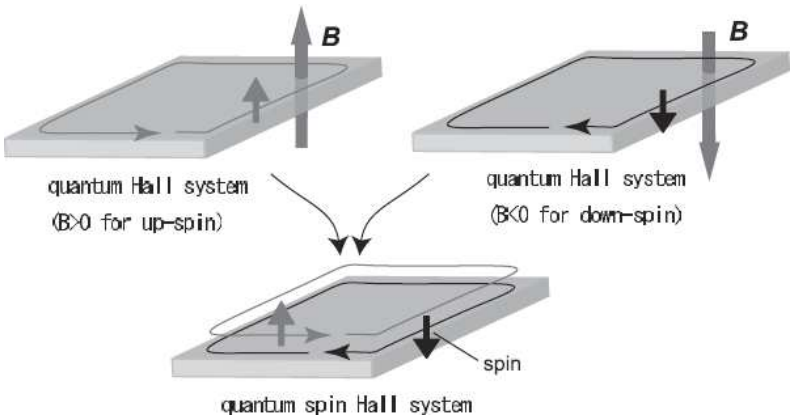

Figure 2.2: Representation of the Quantum Spin Hall phase as two copies of Quantum Hall effect of opposite direction for opposite spins. (Source : Murakami, New J. Phys. 9 (2007) 356)

2.1.2 The $\mathbb{Z}_2$ topological invariant

This first approach to a time-invariant topological invariant as a pair of reversed quantum Hall effect is not satisfying because to mimic opposite magnetic fields we used a spin-orbit coupling that preserve the s^z component of the spin whereas we know that because of this coupling there is a relation between spin and momentum : the spin is no longer a good quantum number. More precisely, the introduction of the spin-orbit coupling in graphene allows Rashba spin-orbit coupling which in this model is of the form $\mathcal{H}_R = \lambda_R(\sigma^x\tau^z s^y - \sigma^y s^x)$. As a consequence, s^z is not conserved $[s^z, \mathcal{H}] \neq 0$, and we can not separate electrons in spins up and spins down. In the next section, we present how

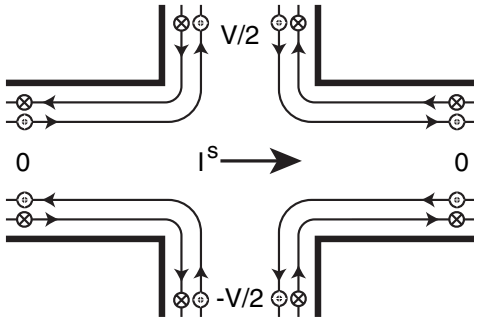

Figure 2.3: Schematic description of the transverse spin current I_s obtained when a bias V is applied to two leads[5].

Kane and Mele derived the $\mathbb{Z}_2$ topological invariant in the general case where we can not identify the quantum spin Hall phase with two copies of quantum Hall effect[40].

2.1.2.1 The time-reversal operation and Kramer's degeneracy

Although they both act on spins, magnetic fields and spin-orbit coupling differ from a symmetry point of view : while a magnetic field breaks the time-reversal symmetry, the spin-orbit coupling does not. The time-reversal operation Θ should be antiunitary because of the Schrödinger equation : if $|\psi(t)\rangle$ is a solution of the Schrödinger equation $i\hbar\partial_t\psi = \mathcal{H}\psi$ by complex conjugation, we expect $|\psi^*(-t)\rangle$ to be another solution. As a consequence, if $|\tilde{\alpha}\rangle = \Theta|\alpha\rangle$ is the action of the time-reversal operation on a given state $|\alpha\rangle$ (and resp. with $|\tilde{\beta}\rangle = \Theta|\beta\rangle$), the two relations defining the antiunitarity and the linearity are satisified :

$$\langle\tilde{\alpha}|\tilde{\beta}\rangle = (\langle\beta|\alpha\rangle)^* , \tag{2.6}$$

$$\Theta(\lambda|\alpha\rangle + \mu|\beta\rangle) = \lambda^*|\tilde{\alpha}\rangle + \mu^*|\tilde{\beta}\rangle . \tag{2.7}$$

Furthermore, we expect this time-reversal operation to leave the position operator invariant $\Theta^{-1}x\Theta = x$ and to reverse momenta operator whether it be canonical momentum $\Theta^{-1}p\Theta = -p$ or orbital momentum $\Theta^{-1}J\Theta = -J$. The antiunitarity property of the time-reversal operation allows to write this operation as a product of a unitary transformation U and the complex conjugation K : $\Theta = UK$. In the case of the spin 1/2 particles we are interested in, this time-reversal operation acts on the spin, and we can write it as $\Theta = -i\eta s^y K$. Here the η denotes an arbitrary phase of the operator. This operation corresponds to a π rotation of the spin when applied to each component of the spin operator s^x, s^y, s^z, as expected.

What is specific of half integer spins, is the property of the square of the this time-reversal operation : $\Theta^2 = -Id$. This can be understood as the minus sign associated to a 2π rotation (2 successive π rotations) of a spin $1/2$. Because of this specific value of Θ^2, we know that in the case of a time-reversal symmetric Hamiltonian $\Theta^{-1}\mathcal{H}\Theta = \mathcal{H}$, for every eigenstate $|n\rangle$ of energy E_n, there exists a different state $\Theta|n\rangle \neq |n\rangle$ at the same energy. Indeed, if these two states were equivalent, we could write $\Theta|n\rangle = e^{i\delta}|n\rangle$ and applying Θ a second time leads to $\Theta^2|n\rangle = \Theta e^{i\delta}|n\rangle = |n\rangle$ which is in contradiction with $\Theta^2 = -Id$. This two fold degeneracy, combination of the time-reversal symmetry and of the spin $1/2$ nature of the electrons is called Kramer's degeneracy.

In the case of a lattice model, we can introduce a reduced Bloch Hamiltonian $\mathcal{H}_{\vec{k}}$ on the first Brillouin zone that should satisfy the relation $\Theta^{-1}\mathcal{H}_{\vec{k}}\Theta = -\mathcal{H}_{-\vec{k}}$ (even if the total Hamiltonian is time-reversal symmetric $\Theta^{-1}\mathcal{H}\Theta = \mathcal{H}$). In this case, degeneracy is recovered only at specific points of the Brillouin zone such that $\vec{k}$ and $-\vec{k}$ differ by a reciprocal lattice vector $\vec{G}$. These points are called time reversal invariant momenta (TRIM), pictured in Fig. 2.4 for a square Brillouin zone.

As pictured in Fig. 2.5, we can observe two different kinds of energy spectra when $\vec{k}$ is moved on a line between two TRIMs, depending on whether there is an exchange of the Kramer's pair partners between the two TRIM or not. It is possible to imagine a Fermi energy in the gap below (or above) the two eigenstates at every $\vec{k}$ by slightly changing them only according to the first scenario (left picture). These two pictures hint at the difference between a trivial insulator, with an even number of pair of edge states at every Fermi energy in the gap, and a topological insulator where it is odd.

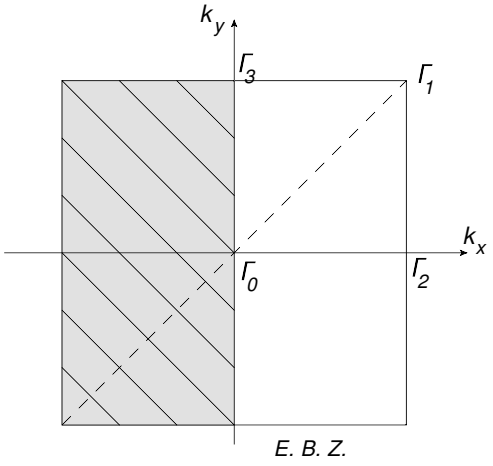

Figure 2.4: Representation of the Brillouin zone, reduced to the effective Brillouin zone. The four time-reversal invariant momenta Γ_i are also represented.

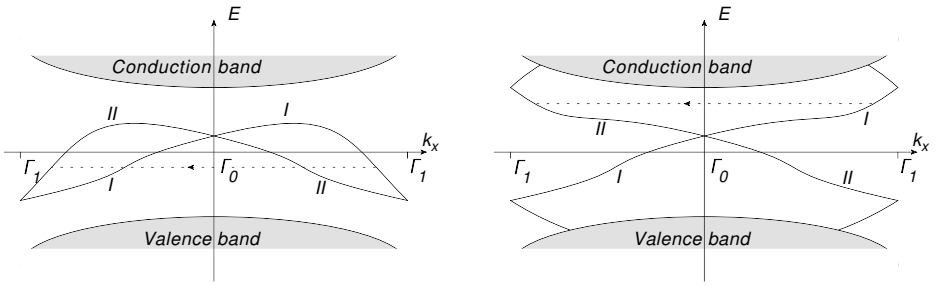

Figure 2.5: Dispersion of the edge states along a line connecting two TRIM for a trivial insulator (left) and for a topological insulator (right). In the two cases, the Kramer's pair are labeled I and II, and is pictured the time-reversal operation between them.

2.1.2.2 The construction of the $\mathbb{Z}_2$ topological invariant

Thanks to the time-reversal symmetry, we can focus on half of the Brillouin zone and define an effective Brillouin zone twice smaller (for example, restrained to the domain where $k_x \geq 0$). The states on the rest of the Brillouin zone can be deduced from those on the effective Brillouin zone through the relation :

$$|u^I_{-\vec{k}}\rangle = e^{i\chi_{\vec{k}}}\Theta|u^{II}_{\vec{k}}\rangle \ , \tag{2.8}$$

$$|u^{II}_{-\vec{k}}\rangle = -e^{i\chi_{-\vec{k}}}\Theta|u^{I}_{\vec{k}}\rangle \ . \tag{2.9}$$

Here the superscripts I and II distinguish the states forming a Kramer's pair at a TRIM. We have explicitly written in these equation the phase-dependance $\chi_{\vec{k}}$ that will be responsible for topological properties when integrated over the Brillouin zone. We should notice that we deduce Eq. (2.9) from Eq. (2.8) by applying the time-reversal operation Θ, this is why the same phase appears in the two equations.

We have seen in Sec.1.2.3 how to integrate the Berry curvature on all the Brillouin zone in the Haldane model. In particular, we parametrized the Hamiltonian as $\mathcal{H}(\vec{k}) = \vec{h}(\vec{k}).\vec{\sigma}$, and when $\vec{h}$ spans the whole Bloch sphere when $\vec{k}$ moves in the Brillouin zone, there is an obstruction to define consistently the phase on each point.

We solved this obstruction by defining the phase on two subspaces with a different gauge in each domain, and the integration reduced to the integration of the transition function between the two gauges at the boundary between the two domains.

Similarly, we will separate our effective Brillouin zone in two parts (for example depending on the sign of k_y) labeled A and B (cf. Fig. 2.6). The phase χ on each domain will be taken to be constant : hence all the winding of this phase will be associated with the transition function, as we have done in the calculation of the Chern number in the Haldane model.

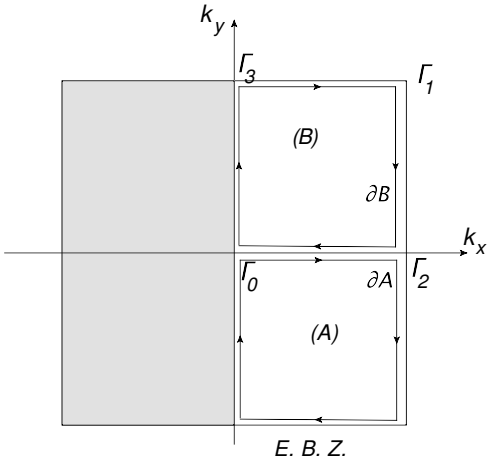

Figure 2.6: Representation of the Brillouin zone and the effective Brillouin zone, with the two domains (A) and (B) where the phase is assumed to be constant.

Consequently, on each subspace, we have the relations $|u^I_{-\vec{k}}\rangle = \Theta|u^{II}_{\vec{k}}\rangle$ and $|u^{II}_{-\vec{k}}\rangle = -\Theta|u^I_{\vec{k}}\rangle$, and at the boundary $A \cap B$, the transition function is a 2 by 2 matrix reading :

$$|u^n_A(\vec{k})\rangle = t^{nm}_{AB}(\vec{k})|u^m_B(\vec{k})\rangle \ . \tag{2.10}$$

where the indices $n, m = I, II$.

This 2 by 2 matrix should be unitary, and defining $\theta(\vec{k})$ such that $\det[t(\vec{k})] = e^{i\theta(\vec{k})}$, the integral of the transition function is :

$$D = \frac{1}{2\pi}\oint_{\partial A} \vec{\nabla}\theta(\vec{k}).d\vec{k} = \frac{1}{2\pi i}\oint_{\partial A} Tr\left[t^\dagger \vec{\nabla} t\right] d\vec{k} \ , \tag{2.11}$$

where $Tr\left[t^\dagger \vec{\nabla} t\right] = \sum_m \langle u^m_B(\vec{k})|t^\dagger \vec{\nabla} t|u^m_B(\vec{k})\rangle$.

We can get rid of the transition function in this trace by using the relation :

$$\vec{\nabla} t_{AB}|u^m_B\rangle = \vec{\nabla}\left(\underbrace{t_{AB}|u^m_B\rangle}_{|u^m_A\rangle}\right) - t_{AB}\vec{\nabla}|u^m_B\rangle \ . \tag{2.12}$$

We introduce the Berry connection $\vec{\mathcal{A}}_A$ and $\vec{\mathcal{A}}_B$ on each subspace A and B as $\vec{\mathcal{A}}_\alpha = +i\sum_{n=I,II}\langle u^n_\alpha|\nabla|u^n_\alpha\rangle$, and we find :

$$D = \frac{1}{2\pi}\oint_{\partial A} d\vec{k}.\left(\vec{\mathcal{A}}_B - \vec{\mathcal{A}}_A\right) . \tag{2.13}$$

Within the domain A, $|u_A\rangle$ is well defined, so we can use Stokes' theorem and write $\oint_{\partial A} d\vec{k}\vec{\mathcal{A}}_A = \int_A d^2k\mathcal{F}_A$, where we defined the Berry curvature $\mathcal{F} = \vec{\nabla}\times\vec{\mathcal{A}}$. It is not possible to apply directly this theorem for the integral of $\vec{\mathcal{A}}_B$ since $\vec{\mathcal{A}}_B$ is *a priori* not well defined on all the domain A, but we can write the integration domain ∂A as $\partial EBZ - \partial B$ (cf. Fig. 2.7).

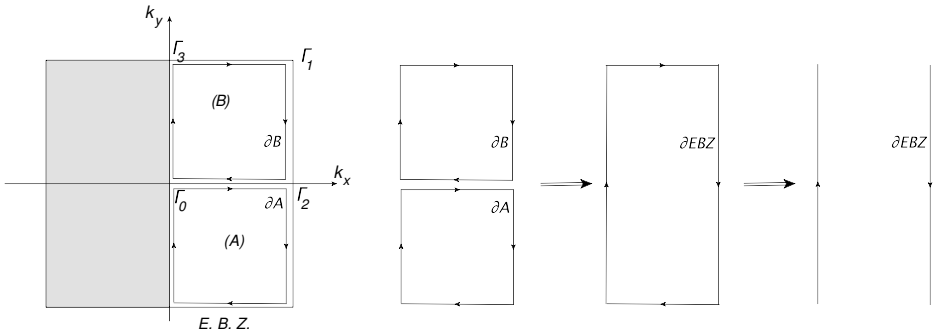

Figure 2.7: Representation of the definition of the contours of the domains A and B, and of the effective Brillouin zone.

We obtain :

$$D = \frac{1}{2\pi}\left(\oint_{\partial EBZ} d\vec{k}\vec{\mathcal{A}} - \int_{EBZ}\mathcal{F}d^2k\right) . \tag{2.14}$$

We have seen in Sec.1.2.3 that an arbitrary change of the phase of one of the two bands on one domain does not affect the Berry curvature $\mathcal{F}$: this allowed us to drop the subscript in the previous equation. However, this arbitrary change of phase could change the value of the Berry connection, and in general, the consequence is to change the integral by an integer. However, because of the time-reversal symmetry $|u^I_{-\vec{k}}\rangle = \Theta|u^{II}_{\vec{k}}\rangle$ and $|u^{II}_{-\vec{k}}\rangle = -\Theta|u^I_{\vec{k}}\rangle$ we can not change the Berry curvature of one band without changing the other. This affects D and changes it only by an even integer. Hence only two inequivalent topological invariants[9] exist :

- if D=0 mod 2, it is possible to choose the phase such that $D = 0$ and we have a trivial insulator, with no winding of the phase around the Brillouin zone ;
- if D=1 mod 2, it is not possible to choose the phase such that $D = 0$. The corresponding phases are the topological insulators.

2.2 3 dimensional topological insulators

After the discovery of quantum Hall effect in 1980, the paradigm was that such topological phases require two ingredients : the breaking of time-reversal symmetry and the 2 dimensionality, but with the discovery of the quantum spin Hall effect and its $\mathbb{Z}_2$ topological invariant it was clear that the breaking of time-reversal symmetry was not crucial to have topological order. The natural step forward was to look after three dimensional generalization of the quantum spin Hall effect, with a topological invariant similar to the $\mathbb{Z}_2$ invariant of the QSH phase.

However it is not possible to define a Chern number in three dimension, this is why the proposals for 3 dimensional quantum Hall effect were indeed 2+1 dimensional as stacked layers of 2 dimensional quantum Hall effect phases[41]. The reason lies in the topology of fiber bundles, and can be seen as an analog of the theorem of the hairy ball, only valid for spheres of *even* dimension. As a consequence we need a different interpretation for the $\mathbb{Z}_2$ invariant, that is not based on Chern classes.

2.2.1 A different interpretation of the $\mathbb{Z}_2$ invariant of the QSH phase

We start with the expression of the $\mathbb{Z}_2$ topological invariant for derived in the Eq. 2.14 :

$$D = \frac{1}{2\pi}\left(\oint_{\partial EBZ} d\vec{k}\vec{\mathcal{A}} - \int_{EBZ} \mathcal{F} d^2k\right) . \tag{2.15}$$

This equation was obtained by dividing the effective Brillouin zone in two domains where the time-reversal operation was assumed to be $|u^I_{-\vec{k}}\rangle = \Theta|u^{II}_{\vec{k}}\rangle$ and $|u^{II}_{-\vec{k}}\rangle = -\Theta|u^I_{\vec{k}}\rangle$.

To obtain a different expression for this topological invariant, we adapt the work done by Fu and Kane[33]. Following them we define the partial Berry connection $\vec{\mathcal{A}}^s = i\langle u^s(\vec{k})|\vec{\nabla}|u^s(\vec{k})\rangle$, and the partial polarization associated to one branch $s = I, II$ for a given k_x as :

$$P^s(k_x) = \frac{1}{2\pi}\oint_{C(k_x)} dk_y \mathcal{A}^s_y , \tag{2.16}$$

where the contour of integration $C(k_x)$ consists of a straight line crossing the effective Brillouin zone at constant k_x. We also define the total polarization $P^{tot}(k_x) = P^I(k_x) + P^{II}(k_x)$ and the time-reversal polarization $P^\theta(k_x) = P^I(k_x) - P^{II}(k_x)$. From the time-reversal operation definition $|u^I_{-\vec{k}}\rangle = \Theta|u^{II}_{\vec{k}}\rangle$ and $|u^{II}_{-\vec{k}}\rangle = -\Theta|u^I_{\vec{k}}\rangle$, we deduce $\vec{\mathcal{A}}^{II}(\vec{k}) = -\vec{\mathcal{A}}^I(-\vec{k})$. With a change of variable $k_y \leftrightarrow -k_y$, we find that $P^{II}(k_x) = P^I(-k_x)$.

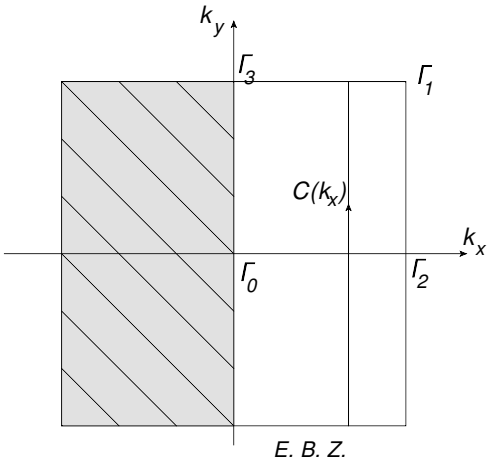

Figure 2.8: Representation of the contour of integration $C(k_x)$ in Eq. 2.16.

We want to express the two terms in the Eq.2.15 as a function of these polarizations. For the first term we find :

$$\frac{1}{2\pi}\int_{\partial EBZ} d\vec{k}\vec{\mathcal{A}} = P^I(0) + P^{II}(0) - P^I(K_x) - P^{II}(K_x)\ . \tag{2.17}$$

where K_x is the value of k_x at the edge of the Brillouin zone. In this case, $K_x = -K_x$ up to a reciprocal lattice vector so $P^{II}(K_x) = P^I(-K_x) = P^I(K_x)$, and we can write this term as $2(P^I(0) - P^I(K_x))$.

The second term is an integral over the whole effective Brillouin zone, and not only its border $\frac{1}{2\pi}\int_{EBZ} d^2k\mathcal{F}$. We express $\mathcal{F} = \partial_{k_x}\mathcal{A}_y - \partial_{k_y}\mathcal{A}_x$ and using the Fubini theorem we find :

$$\begin{aligned}\frac{1}{2\pi}\int_{EBZ} d^2k\mathcal{F} =& \frac{1}{2\pi}\int_{EBZ} dk_x dk_y \partial_{k_x}\mathcal{A}_y + \partial_{k_y}\mathcal{A}_x \\ =& \frac{1}{2\pi}\left(\int dk_x \underbrace{\mathcal{A}_x(K_y) - \mathcal{A}_x(-K_y)}_{=0} - \int dk_y \mathcal{A}_y(K_x) - \mathcal{A}_y(0)\right) \qquad (2.18)\\ =& P^{tot}(0) - P^{tot}(K_x)\ . \qquad (2.19)\end{aligned}$$

Collecting Eq. (2.17) and Eq. (2.19) we can express the topological invariant D as :

$$D = P^\theta(0) - P^\theta(K_x)\ . \tag{2.20}$$

To derive this equation, we divided the effective Brillouin zone into two domains A and B where the phase χ in :

$$|u^I_{-\vec{k}}\rangle = e^{i\chi_{\vec{k}}}\Theta|u^{II}_{\vec{k}}\rangle\ , \tag{2.21}$$

$$|u^{II}_{-\vec{k}}\rangle = -e^{i\chi_{-\vec{k}}}\Theta|u^I_{\vec{k}}\rangle\ , \tag{2.22}$$

was assumed to be constant. However, this expression is still correct when $\chi_{\vec{k}}$ evolves continuously on the Brillouin zone, instead of jumping at the boundary between the domains, since the quantity P^θ is just defined as a relation on the two different branches.

In the more general case where the phase $\chi(\vec{k})$ is not constant on different domains of the effective Brillouin zone, but cis a smooth fuction of $\vec{k}$, the relation coming from the time-reversal operation between the partial Berry's connections $\vec{\mathcal{A}}^{II}(\vec{k}) = -\vec{\mathcal{A}}^{I}(-\vec{k})$ becomes :

$$\vec{\mathcal{A}}^{I}(-\vec{k}) = -\vec{\mathcal{A}}^{II}(\vec{k}) - \vec{\nabla}\chi(\vec{k}) \; . \tag{2.23}$$

To evaluate the partial polarization $P^I(k_x)$, we split the domain of integration depending on the sign of k_y :

$$P^I(k_x) = \frac{1}{2\pi}\int_{-K_y}^{K_y} dk_y \mathcal{A}^I_y(k_x,k_y) = \frac{1}{2\pi}\int_{0}^{K_y} dk_y \mathcal{A}^I_y(k_x,k_y) - \mathcal{A}^I_y(k_x,-k_y) \; . \tag{2.24}$$

Using Eq.2.23 in this equation gives :

$$P^I(k_x) = \frac{1}{2\pi}\left(\int_{0}^{K_y} dk_y \mathcal{A}^I_y(k_x,k_y) + \mathcal{A}^{II}_y(-k_x,k_y) - (\chi(-k_x,K_y) - \chi(-k_x,0))\right) \; . \tag{2.25}$$

Introducing the matrix relating the time-reversed bands of coefficient $w_{\alpha\beta}(\vec{k}) = \langle u^\alpha(-\vec{k})|\Theta|u^\beta(\vec{k})\rangle$:

$$w(\vec{k}) = \begin{pmatrix} 0 & e^{i\chi(\vec{k})} \\ -e^{i\chi(-\vec{k})} & 0 \end{pmatrix} \; , \tag{2.26}$$

we can express the phase $\chi(\vec{k})$ as the Pfaffian of this matrix when it is antisymmetric, which happens at the time-reversal invariant momenta. Indeed, for a 2 by 2 antisymmetric matrix, the Pfaffian is just the upper-right coefficient. It is then possible to write $\exp i\chi(\vec{k}) = Pf[w(\vec{k})]$ when $\vec{k}$ is a TRIM.

We use this property to write $P^I(k_x)$ at the special points where $k_x = 0, K_x$ since the phases χ that appear in the second member of Eq. (2.25) will be located at TRIM :

$$P^I(k_x = 0, K_x) = \frac{1}{2\pi}\left(\int_0^{K_y} dk_y (\mathcal{A}^I(k_x,k_y) + \mathcal{A}^{II}(-k_x,k_y))_y \right. \\ \left. + i\log\frac{Pf[w(k_x,K_y)]}{Pf[w(k_x,0)]}\right) \; . \tag{2.27}$$

Following the same procedure for $P^{II}(\vec{k_x})$ gives the similar result and collecting this results in $P^\theta = P^I - P^{II}$ gives :

$$P^\theta(k_x = 0, K_x) = \frac{1}{2\pi}\left[\int_0^{K_y} dk_y \mathcal{A}_y(k_x, k_y) - \int_{-K_y}^{0} dk_y \mathcal{A}_y(k_x, k_y) + 2i \log \frac{Pf[w(k_x, K_y)]}{Pf[w(k_x, 0)]}\right] . \tag{2.28}$$

where $\mathcal{A} = \mathcal{A}^I + \mathcal{A}^{II}$ is the total Berry connection. We want to rewrite the two first terms of the expression Eq. (2.28) as a function of the w matrix defined in Eq. (2.26). The first step is to calculate :

$$Tr\left[w^\dagger \vec{\nabla}_{\vec{k}} w\right] = \sum_{\alpha\beta} \langle u^\alpha(\vec{k})|\Theta^\dagger|u^\beta(-\vec{k})\rangle \vec{\nabla}_{\vec{k}} \langle u^\beta(-\vec{k})|\Theta|u^\alpha(\vec{k})\rangle . \tag{2.29}$$

Distributing the action of the derivative on $\Theta|u^\alpha(\vec{k})\rangle$ and on $\langle u^\beta(-\vec{k})|$, and using a closure relation, this trace is evaluated as :

$$\begin{aligned} Tr\left[w^\dagger \vec{\nabla}_{\vec{k}} w\right] =& \sum_\alpha \langle u^\alpha(\vec{k})|\Theta^\dagger \vec{\nabla}_{\vec{k}} \Theta|u^\alpha(\vec{k})\rangle \\ &+ \sum_{\alpha\beta} \langle u^\alpha(\vec{k})|\Theta^\dagger|u^\beta(-\vec{k})\rangle \langle \vec{\nabla}_{\vec{k}} u^\beta(-\vec{k})|\Theta|u^\alpha(\vec{k})\rangle , \\ =& \frac{1}{i}\mathcal{A}(\vec{k}) + \sum_\beta \langle \vec{\nabla}_{\vec{k}} u^\beta(-\vec{k})|u^\beta(-\vec{k})\rangle , \qquad (2.30) \\ =& \frac{1}{i}\left(\mathcal{A}(\vec{k}) - \mathcal{A}(-\vec{k})\right) . \qquad (2.31) \end{aligned}$$

Introducing this result in Eq. (2.28), we find :

$$P^\theta(k_x = 0, K_x) = \frac{1}{2\pi i}\left(\int_0^{K_y} dk_y Tr\left[w^\dagger \vec{\nabla}_{\vec{k}} w\right] - 2\log \frac{Pf[w(k_x, K_y)]}{Pf[w(k_x, 0)]}\right) . \tag{2.32}$$

With the definition of w of Eq. (2.26), we show that $Tr\left[w^\dagger \vec{\nabla}_{\vec{k}} w\right] = \vec{\nabla}_{\vec{k}} \log Det[w(\vec{k})]$. Moreover at the TRIM, because the w matrix is antisymmetric we have $Det[w[\vec{k}]] = Pf[w[\vec{k}]]^2$. As a conclusion, it seems that P^θ should vanish.

However, in Eq. (2.32) appears logarithms of complex functions, but the definition of a logarithm in the complex plane is ambiguous. Indeed we want the logarithm to respect $\exp(\log x) = x$, but $\exp(2i\pi) = 1$, as a consequence the logarithm can be defined only up to $2i\pi\mathbb{Z}$. Thus depending on the respective definition of the logarithm in the integral, and the log for the pfaffians, P^θ is only defined modulo 2. The two different values correspond to whether

the Pfaffians at the two TRIM correspond to the same branch of the root of the determinant or not.

In the end, we can write this as :

$$(-1)^{P^\theta(k_x=0,K_x)} = \frac{\sqrt{Det[w[k_x,0]]}}{Pf[w[k_x,0]]}\frac{\sqrt{Det[w[k_x,K_y]]}}{Pf[w[k_x,K_y]]} \ . \tag{2.33}$$

where we suppressed the ambiguity on the square root by assuming that $\sqrt{Det[w[k_x,k_y]]}$ is defined continuously on the effective Brillouin zone.

We have sen in Eq. (2.20) that the topological invariant we want to derive is $D = P^\theta(0) - P^\theta(K_x)$, so using Eq. (2.33) this topological invariant is equal to :

$$(-1)^D = \prod_{i=0}^{3}\delta_i \qquad \text{where} \qquad \delta_i = \frac{\sqrt{Det[w[\Gamma_i]]}}{Pf[w[\Gamma_i]]} \ . \tag{2.34}$$

where the Γ_i are the 4 time-reversal invariant momenta (cf. Fig. 2.4).

If we consider only a product of two δ_i, for example $\delta_0\delta_1$, its physical meaning is what we have seen in Fig. 2.5 : it corresponds to whether or not the Kramers' pair partners are the same at the two TRIM. This product can be changed, for example by a gauge depending on $\vec{k}$, but we have just shown the product of the four δ can not as it is the topological invariant.

2.2.2 Application to 3 dimensional topological insulators

We expressed the $\mathbb{Z}_2$ topological invariant in the case of two-dimensional topological insulator only as a function calculated at the time-reversal invariant momenta (TRIM) instead of an integral over the whole Brillouin zone. As opposed to the Chern number, defined only in even dimension, this definition can be extended directly to three dimensional insulators[8]. In three dimensions, there are 8 distinct TRIM Γ_i defined via the reciprocal lattice vectors $\vec{b}_1$, $\vec{b}_2$ and $\vec{b}_3$ as $\Gamma_{i=n_1n_2n_3} = n_1\vec{b}_1 + n_2\vec{b}_2 + n_3\vec{b}_3$ with $n_i = 0, 1$. For each of these TRIM, we define a parameter $\delta_{n_1n_2n_3} = \pm 1$ consistently with what we have done in Eq. (2.34) :

$$\delta_i = \frac{\sqrt{Det[w(\Gamma_i)]}}{Pf[w(\Gamma_i)]} \ . \tag{2.35}$$

where $w_ij(\vec{k}) = \langle u_i(\vec{k})|\Theta|u_j(\vec{k})\rangle$ is antisymmetric at the TRIM.

With these δ_i it is now possible to construct a $\mathbb{Z}_2$ invariant ν_0 such that :

$$(-1)^{\nu_0} = \prod_{n_i=0,1}\delta_{n_1n_2n_3} \ . \tag{2.36}$$

Fu, Kane and Mele[8] showed that this product of the 8 δ is gauge invariant even if none of them is gauge invariant.

It is also possible to construct three other invariants as :

$$(-1)^{\nu_{i=1,2,3}} = \prod_{n_i=1, n_{j\neq i}=0,1} \delta_{n_1 n_2 n_3} \ . \tag{2.37}$$

If these four invariants are zero, then we are in the topological phase of the trivial insulators. When $\nu_0 = 1$, the number of surfaces states is odd, whereas it is even when $\nu_0 = 0$ (it can be zero). In the case of $\nu_0 = 0$, when one of the other invariant does not vanish, the surfaces states appear as the edge states of stacked QSH phases, and the direction of this stacking is given by the three indices as $\sum_{i\neq 0} \nu_i \vec{b}_i$. The surface states number is only defined modulo 2, and they can be coupled by disorder. In the case of "stacked QSH", with $\nu_0 = 0$, it is likely that the disorder will turn them into trivial insulators by opening a gap coupling the surface states by pairs : they are called "weak topological insulators", as opposed to the $\nu_0 = 1$ "strong" topological insulators where always exists at least one surface state[42][43].

Il faut, messieurs, agir ! Agir et faire !

Anton Tchekov, *Oncle Vania*

Chapter 3

Experimental realizations

3.0.3 Spin-orbit coupling

The spin-orbit coupling is a crucial ingredient for the existence of topological insulators. In this section, I briefly explain where does it come from and how we can treat it. This spin orbit coupling comes from the approximation of the Dirac equation for relativistic particles when their velocity is small compared to the speed of light $v \ll c$. In this case, and at the first order, the Hamiltonian reads :

$$\mathcal{H} = mc^2 + \frac{p^2}{2m} + V(\vec{r}) - \frac{p^4}{8m^3c^2} - \frac{\hbar}{4m^2c^2}\vec{\sigma}.(\vec{p}\times\vec{\nabla}(V)) + \frac{\hbar^2}{8m^2c^2}\Delta V + \dots \quad (3.1)$$

The first term is the rest energy of the particle, the second one its kinetic energy and the third term is a potential energy.

The fourth term $\frac{p^4}{8m^3c^2}$ is relativistic, as it originates from the formula $E^2 = m^2c^4 + p^2c^2$.

The fifth term $-\frac{\hbar}{4m^2c^2}\vec{\sigma}.(\vec{p}\times\vec{\nabla}(V))$ is the spin-orbit coupling we are interested in, and the last term, called the Darwin term, is only included to respect the series expansion.

We can interpretate this spin-orbit coupling term as follows. By a change of the reference frame, the electric field $\vec{E}$ felt by an electron at speed $\vec{v}$ is equivalent to a magnetic field $\vec{B} = \frac{-1}{c^2}(\vec{v}\times\vec{E})$. If we consider that this magnetic field act on the spin of the electron through Zeeman interaction $g\mu_B\vec{\sigma}.\vec{B}$ where $\mu_B = \frac{eh}{2m}$ is the Bohr magneton, this leads to an interaction :

$$\mathcal{H}_{SO} = \frac{-\hbar}{2m^2c^2}\vec{\sigma}.(\vec{p}\times\vec{\nabla}(V)) \; . \quad (3.2)$$

The difference by a factor of two called the Thomas factor originates from the naivety of this interpretation. Refining with a proper calculation for the change of the reference frame leads to the correct factor[44][45], that is anyway integrated by the definition of an effective spin-orbit coupling constant that also includes m and c.

Some remarks are of importance about this expression for the spin-orbit coupling :

- the main contribution to the potential variation $\vec{\nabla}V(\vec{r})$ are not due to an external electric field but to the presence of the atoms on the crystal structure. This explain why we will be looking for heavy atoms, the heavier the atoms, the stronger the spin-orbit coupling, scaling as Z^4 ;

- we can see that this spin-orbit coupling is responsible for a momentum-spin locking : for each direction of propagation of the electron, there is a prefered direction of polarization for the spin minimizing the spin-orbit coupling ;

- this Hamiltonian is time-reversal symmetric, since a time-reversal operation reverse both spin and momentum. Indeed as the time-reversal operator is $\Theta = \exp(i\pi\sigma_y/\hbar)K$, we can check that $\Theta\mathcal{H}_{SO}(\vec{p}) = \mathcal{H}_{SO}(-\vec{p})\Theta$;

- this time-reversal invariance and the spin degeneracy imply the presence of Kramers pairs : for an eigenstate at $\vec{k}$ and spin $\vec{\sigma}$ correspond an eigenstate at $-\vec{k}$ and $-\vec{\sigma}$. Consequently, lifting the spin degeneracy requires a breaking of the inversion symmetry $\vec{k} \leftrightarrow -\vec{k}$. The breaking of the inversion symmetry is due either to a non centro-symmetric crystal (Dresselhauss coupling) or to external asymmetries such as an external electric field, asymmetry of the well, etc (Rashba coupling).

3.1 2 dimensional topological insulators : HgTe quantum wells

As we have seen in the previous chapter, the introduction of spin-orbit coupling turns the graphene into a topological insulator. However, the insulating behavior is not experimentally measurable : the gap created by taking into account this spin-orbit coupling is too small (even if there is no consensus on its magnitude), because graphene is made out of carbon atoms, with too small Z. Indeed, we have seen that the potential variations in the formula of the spin-orbit coupling $-\frac{\hbar}{4m^2c^2}\vec{\sigma}.(\vec{p}\times\vec{\nabla}(V))$ originates from the electronic structure of the atoms in the lattice, and that the heavier the atoms, the stronger the spin-orbit coupling.

Alternatively, the quantum spin Hall effect was also proposed to be seen experimentally in CdTe/HgTe/CdTe quantum wells [7][46]. These semiconductors have been chosen to satisfy different conditions :

- both of them show an important spin-orbit coupling, thanks to massive atoms ;

- their lattice structure is very similar : they are both zincblende lattices, where one type of atom is on a face-centered cubic lattice, and the other at the center of half of the tetrahedra formed by neighboring atoms of the first lattice. Moreover, their lattice constant are very close (6.48 Å for CdTe and 6.45 Å for HgTe) : it is possible to make such a heterojunction without stressing the different lattices too much and changing their band structure ;
- they have inverted band structures : in CdTe, the valence band has p like symmetry, and the conduction band s like ; but in HgTe, because of a stronger spin-orbit coupling, the p like band rises in energy, and become the conduction band.

An inverted band structure is necessary to obtain a phase transition when a critical width of the HgTe layer is reached : when this layer is too thin, the inverted structure can not be felt, and the heterojunction is a trivial semi-conductor as CdTe, but when this width is increased, it should be an inverted semi-conductor as HgTe. We will see that this phase transition is a topological phase transition, turning a trivial insulator into a topological insulator.

3.1.1 Band model and edge states

We consider a quantum well grown in the z-direction, allowing the electrons to evolve freely in a x,y-plane. In the simplest band model, we need to consider only four bands, the ones of opposite parity that touch when the critical width is reached (there are two for each spin). If we consider that the degeneracy between up spins and down spins is lifted, and that time-reversal symmetry is preserved, the effective Hamiltonian can be written as :

$$\mathcal{H}_{eff} = \begin{pmatrix} H(\vec{k}) & 0 \\ 0 & H^*(\vec{k}) \end{pmatrix} . \tag{3.3}$$

In this equation, $H(\vec{k})$ acts on the up spin space, and we deduced the Hamiltonian on the down spin space by time-reversal symmetry. The opposite parity s and p of the two bands of spin up restrains $H(\vec{k})$ so we expect that the terms on the diagonal are even functions of $\vec{k}$ whereas the terms between the different parity bands should be odd function of $\vec{k}$. Using the rotational symmetry in the $k_x - k_y$ plane, we can express this effective Hamiltonian as the lowest order in $\vec{k}$ as :

$$\begin{aligned} H(\vec{k}) &= \epsilon(\vec{k})Id + d_i(\vec{k})\sigma^i , & (3.4)\\ d_x(\vec{k}) &= Ak_x , & (3.5)\\ d_y(\vec{k}) &= Ak_y , & (3.6)\\ d_z(\vec{k}) &= M - B(k_x^2 + k_y^2) . & (3.7) \end{aligned}$$

The overall energy $\epsilon(\vec{k})$ can be dropped in the study of topological invariants as it is just a shift of the energies. The important parameter is the mass parameter M, and in experimental devices, it changes sign when the width of HgTe reaches the critical value of $d_c = 6.3$ nm.

Considering only the up spin (the down spin behavior is deduced by time-reversal symmetry), the bulk dispersion relation is straightforward : $E(\vec{k}) = \epsilon(\vec{k}) \pm \sqrt{(M - Bk^2)^2 + A^2k^2}$, and we can check that it is indeed an insulator, with a band gap $\Delta = 2M$ at the origin.

However, we are interested in edge states. To find them, we focus on an interface between the plane of the electrons and the vacuum, for example, we consider a semi-infinite sample where $y > 0$ and the vacuum when $y < 0$. We look for plane-wave in the x-direction, exponentially decaying in the y-direction, which corresponds to an envelop function of the form $\exp(ik_x x + \lambda y)$. We can solve for λ through the substitution $k_y \leftrightarrow \lambda$ and find that at a given energy E and wave vector k_x there exist 4 different values of λ satisfying the eigenvalue equation :

$$\lambda^2 = k_x^2 + \underbrace{\frac{A^2 - 2BM}{2B^2}}_{F} \pm \sqrt{F^2 - \frac{M^2 - E^2}{B^2}} \ . \tag{3.8}$$

At $E = 0$ and $k_x = 0$, this reduce to the four values :

$$\lambda_{1,2} = \frac{-A \pm \sqrt{A^2 - 4MB}}{2B} \quad ; \quad \lambda_{3,4} = -\lambda_{1,2} \ . \tag{3.9}$$

The corresponding eigenstates are spinors representing the respective weight of the eigenstate on the two different bands. For λ_1 and λ_2, this spinor is $\begin{pmatrix} 1 \\ -1 \end{pmatrix}$, while it is $\begin{pmatrix} 1 \\ 1 \end{pmatrix}$ for $\lambda_{3,4}$. With this values of the λ, we try to obtain edge states that satisfy the boundary conditions.

To obtain edge states, we have to satisfy the limit conditions $|\Psi|^2 \to 0$ when $y \to \infty$. In HgTe/CdTe quantum wells, the A and B parameter do not change significally with the width of the HgTe layer, and both are negative. Edge states exist only for λ real, corresponding to the condition $A^2 > 4MB$. If this condition is satisfied, the only relevant states correspond to $\lambda < 0$ and they differ depending on the sigh of M. The second limit condition is given at the interface.

- When $M > 0$, the two negative values for λ are λ_1 and λ_4, and we can express the edge state as :

$$\Psi(x, y) = \begin{pmatrix} \alpha e^{\lambda_1 y} + \beta e^{\lambda_4 y} \\ -\alpha e^{\lambda_1 y} + \beta e^{\lambda_4 y} \end{pmatrix} \ . \tag{3.10}$$

  We can chose two types of boundary condition at the interface $y = 0$: open boundary condition $\Psi(x, 0) = 0$ or annihilation of the current

at the interface $\partial_y \Psi(x,y)|_{y=0} = 0$ but in both cases, the result is that $\alpha = \beta = 0$, which means that there is no edge state.

- On the opposite, when $M < 0$, we have to chose λ_1 and λ_2 which correspond to the same eigenvector, so we can satisfy the boundary condition at the interface. In this case, the edge state is written as :

$$\Psi(x,y) = \left(\frac{2}{\lambda_1 + \lambda_2} - \frac{1}{2\lambda_1} - \frac{1}{2\lambda_2} \right) \left(e^{\lambda_2 y} - e^{\lambda_1 y} \right) \begin{pmatrix} 1 \\ -1 \end{pmatrix} . \quad (3.11)$$

This corresponds to a wave function with a density probability exponentially increasing from the edge on a length scale λ_1, then exponentially decreasing on the length λ_2 (cf. Fig. 3.1) : we have an edge state. Moreover, when $E \neq 0$, the wave vector associated to the up-spin edge state k_x will be non zero ; by applying the time-reversal symmetry, there is an edge state for the down spin, with wave vector $-k_x$.

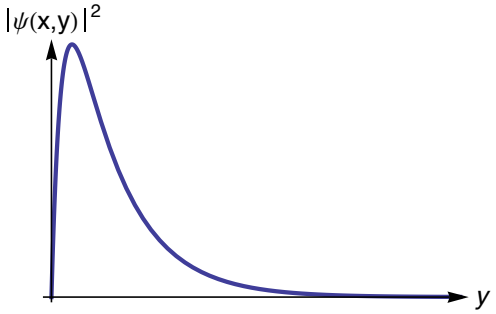

Figure 3.1: Presence probability of the edge state as a function of the distance to the edge (arbitrary units).

This simple model shows us how varying the width of the HgTe layer in the quantum well can change the nature of the phase, from a trivial insulator to a topological insulator, with two edge states, corresponding to counter propagating electrons of opposite spins.

3.1.2 Experimental realization and transport measurements

Within a year after the theoretical proposal for QSHE on HgTe/CdTe quantum wells, the group led by Molenkamp was able to design the corresponding devices, and demonstrate the presence of QSHE [12][47].

To understand their result, we just have to know that this quantum spin Hall phase is characterized by two edge states of opposite velocities for opposite spins. These two edge states can not be backscattered by an impurity as long as the impurity does not allow spin flip : if the spin is preserved during the scattering, so is the velocity. This absence of backscattering means that there

is no loss of the chemical potential of a given direction of the spin along an edge, transport is then ballistic, and we can use the Landauer-Büttiker formalism as explained in Sec. 1.1.2.

3.1.2.1 Two-terminals devices

The two-terminal conductance has first been used in HgTe/CdTe quantum wells to show the existence of the edge states in an insulator : in the case of a trivial insulator, the longitudinal conductance will vary from a positive value when the Fermi energy is in one of the bulk bands to a zero value in the gap, where there is no available states. In the quantum spin Hall phase, there are two edges states available to conduct the current, and each one of them has a conductance of e^2/h, so the drop in conductance should stop at the non zero-value of $2e^2/h$.

The measurements done in 2007 by Molenkamp *et al.* [12] show the different values of the resistance in the gap, as a function of the Fermi energy, for different values of the HgTe layer in the quantum wells (Fig3.2).

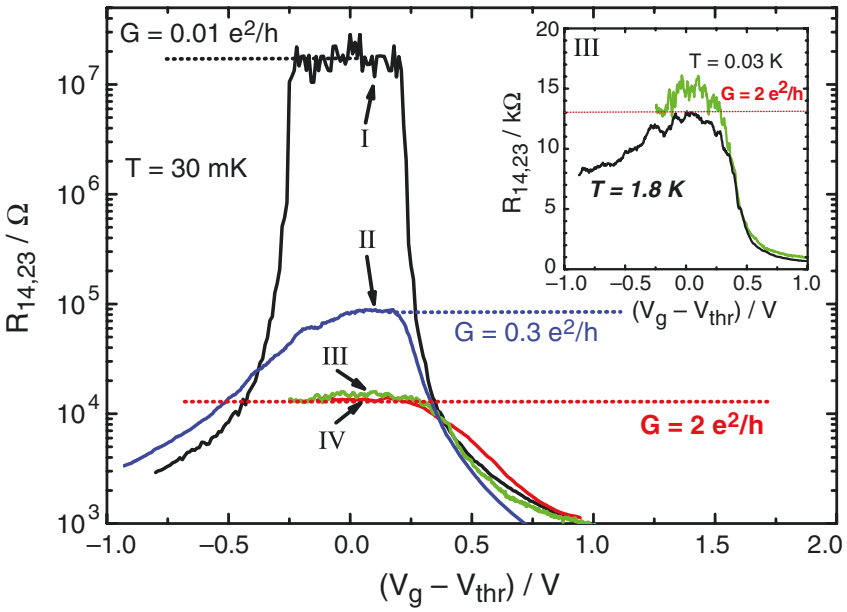

Figure 3.2: Experimental measurement of the longitudinal resistance of HgTe/CdTe quantum wells[12] as a function of the Fermi energy. The curve labeled I corresponds to a trivial insulator (the width of the HgTe layer is thinner than the critical width). Curves II,III and IV correspond to QSH phases. The II curve is done for a longer sample, losing the ballistic behavior of the edge states thus increasing resistance.

As we can see in the Fig.3.2, there is a plateau at the value of $2e^2/h$ showing the presence of two edge states. However, the same plateau can be seen in any other experiment where two perfectly conducting channels coexist, for example in a quantum Hall system with a filling factor of 2 (the filling factor is the number of Landau levels in Sec. 1.1). To discriminate the quantum spin Hall effect from other system with two edge states, further experiments have been done, using a Hall bar geometry.

3.1.2.2 4 and 6-terminals devices

4 and 6 terminal devices have been used to probe the absence of chemical potential drop along the edge of a quantum Hall system, or similarly to show that a perfect conducting channel has an infinite conductance if we suppress the contact resistances (the one responsible for the finite value of e^2/h).

Using a 6-terminal device for a quantum spin Hall system allows to probe a whole set of resistances $R^{\alpha\beta}_{\gamma\delta}$ obtained as the voltage drop between the leads α and β divided by the current I that flows from the γ to the δ leads.

Using the Landauer-Büttiker formalism, we express the current flowing from the lead α to the Hall bar as a function of the chemical potential of each lead through a conductance matrix : $I_\alpha = \sum_\beta G_{\alpha\beta} V_\beta$.

The conductance matrix is constrained by Kirchoff's laws, as $\sum_\beta G_{\alpha\beta} = 0$ to ensure the conservation of the charge, and $\sum_\alpha G_{\alpha\beta} = 0$ because the chemical potentials are defined up to an additive constant. In the case of perfectly transmitted channels, the coefficient on the diagonal $G_{\alpha\alpha}$ are the number of conducting channels going out of the lead α times the quantum of conductance $G_{\alpha\alpha} = n_\alpha e^2/h$, the non diagonal coefficients $G_{\alpha\beta}$ are the opposite of the number of channels coming from the lead β to the lead α : $G_{\alpha\beta} = n_{\beta\alpha} e^2/h$.

For example, for a 6-terminals device, in the case of two chiral edge states in the quantum Hall effect, this matrix is :

$$G^{QHE} = \begin{pmatrix} 2 & 0 & 0 & 0 & 0 & -2 \\ -2 & 2 & 0 & 0 & 0 & 0 \\ 0 & -2 & 2 & 0 & 0 & 0 \\ 0 & 0 & -2 & 2 & 0 & 0 \\ 0 & 0 & 0 & -2 & 2 & 0 \\ 0 & 0 & 0 & 0 & -2 & 2 \end{pmatrix} . \tag{3.12}$$

We can build similarly the matrix corresponding to counter propagating edge states of quantum spin Hall effect, in this case there are still two edge states coming out of each leads, but the incoming ones are associated to different leads, and we obtain :

$$G^{QSH} = \begin{pmatrix} 2 & -1 & 0 & 0 & 0 & -1 \\ -1 & 2 & -1 & 0 & 0 & 0 \\ 0 & -1 & 2 & -1 & 0 & 0 \\ 0 & 0 & -1 & 2 & -1 & 0 \\ 0 & 0 & 0 & -1 & 2 & -1 \\ -1 & 0 & 0 & 0 & -1 & 2 \end{pmatrix} . \tag{3.13}$$

This conductance matrix formalism shows why the same result is obtained for 2-terminal devices as in both cases $G = \begin{pmatrix} 2 & -2 \\ -2 & 2 \end{pmatrix}$, and why we expect a different signature with a higher number of leads. To gain access to the resistivity $R^{\alpha\beta}_{\gamma\delta}$, we set $I_\gamma = -I_\delta = I$ and $I_\epsilon = 0$ for $\epsilon \neq \gamma, \delta$, and we invert the conductance matrix, using the Kirchoff's laws. This provides the value of the chemical potential in each lead, which is what we needed to have the resistances $R^{\alpha\beta}_{\gamma\delta}$.

In the case of quantum Hall effect, we find that these resistances can take only two values, 0 and $h/(2e^2)$ in both four and six terminals measurements, but in the case of quantum spin Hall effect many more values with specific fractions of h/e^2 can be reached by changing the leads where flows the current and where are measured the chemical potentials (cf Fig.3.3). As we can see in Fig. 3.4 where these values are the dashed lines, the experimental values[48] are in good agreement with the theory.

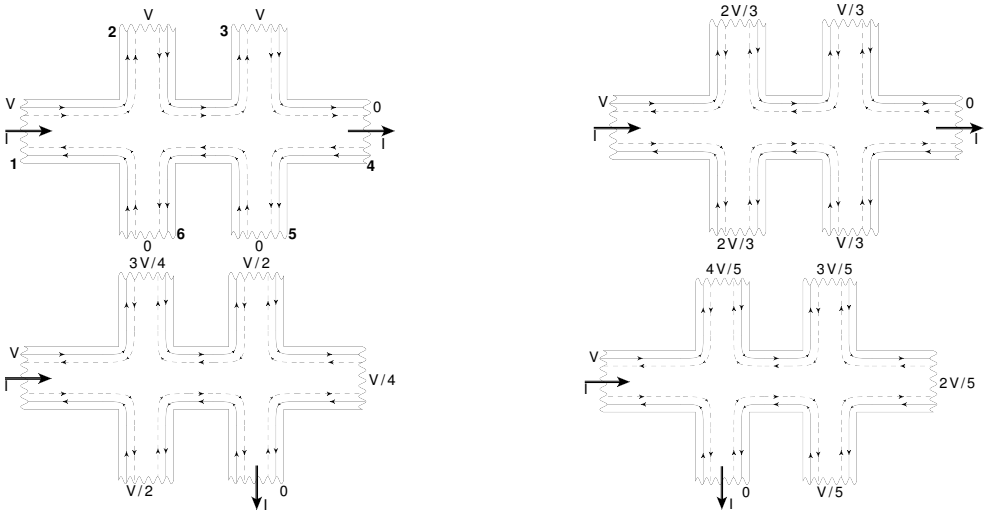

Figure 3.3: Schematic representation of the six-terminal measurements. Top left : a measurement for quantum Hall effect at filling factor $\nu = 2$. The three others show the different values of the chemical potentials when the current leads are changed in the case of a quantum spin Hall phase.

The experimental proof of the edge states transport in quantum spin Hall

effect, as well as their helical nature (they are of opposite velocity for opposite direction of the spin) was the trigger of the research in the field of topological insulators[49][50].

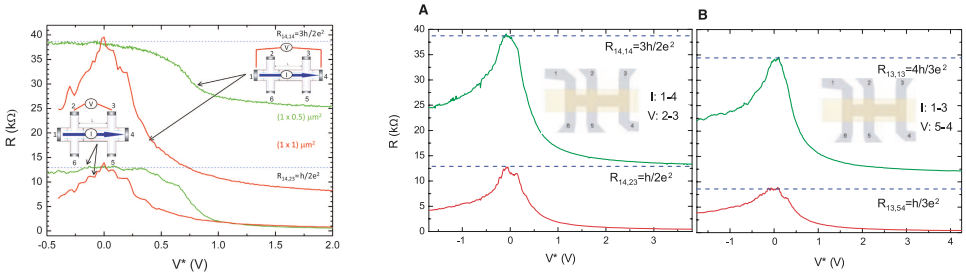

Figure 3.4: Experimental plots of different 4 terminal resistances [48]. The dashed lines correspond to the theoretically expected values. The drop for high values of the voltage means that we enter the bulk band, and the quantum well is no longer insulating.

3.1.3 Experimental realizations of 3D topological insulators

3.1.3.1 ARPES experiments

The theoretical propositions for 3 dimensional topological insulators were first looked among materials with strong spin-orbit coupling such as $Bi_{1-x}Sb_x$[51] where the band theory predicts a non zero ν_0. The transport measurements we use in 2 dimensional samples to show their topological insulator properties are difficult to use in the case of 3DTI because the extra dimension can be seen as a multiplication of the conducting channels. Moreover, this extra dimension allows for diffusive processes as opposed to the ballistic edge states of quantum spin Hall effect as we will see in Ch. 5. However, there are other ways to probe the existence of surface states, and one of them is the angle-resolved photo-electron spectroscopy (ARPES).

In an ARPES experiment, a laser beam is shined on the surface of the sample and through photo-electric effect some electrons are emitted. By conservation of energy, and measurement of the electron momentum, the dispersion relation is probed. The surface states are distinguished from the bulk states by varying the energy of the incoming photons : the change in energy can be absorbed only if there is a component of the electron transverse to the surface to absorb the extra energy.

The first ARPES experiments were done[13][52] on $Bi_{1-x}Sb_x$ and showed the presence of an odd number of Dirac cones as surface states (Fig. 3.5), as expected[53].

This first experimental proof of topological insulators in three dimensions lead physicists to find other materials, with a simpler band structure, and

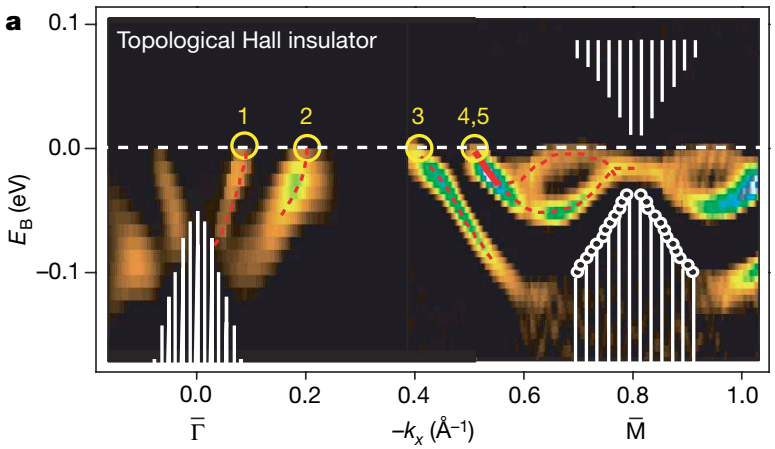

Figure 3.5: ARPES experiment showing the presence of 5 surface states in $Bi_{1-x}Sb_x$. The white stripes correspond to the bulk bands.

possibly a larger gap. It was shown[11] that a family of compounds (Bi_2Se_3, Bi_2Te_3 and Sb_2Te_3) presents a unique surface state. Moreover, the fact that they are stoichiometric compounds, instead of an alloy in the case of $Bi_{1-x}Sb_x$ allows a growth with higher purity. Simulations of the expected dispersions in these materials are plotted in Fig. 3.6.

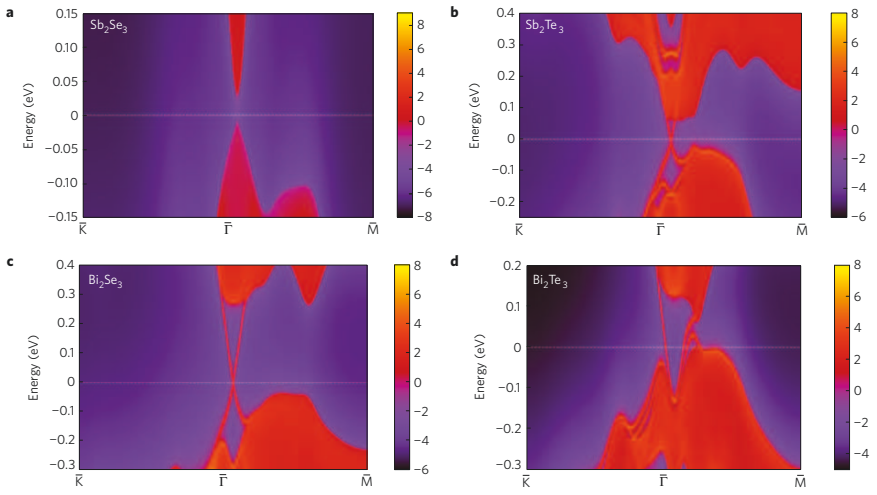

Figure 3.6: Dispersion relation from *ab initio* calculations for the Bi_2Se_3 family of compounds, showing that three of them are topological insulators with a single surface state[11].

These works also demonstrated that these surface states obey a linear dispersion relation as expected : because of the strong spin-orbit coupling, the

lowest order in $\vec{k}$ time-reversal symmetric Hamiltonian possible is a Hamiltonian where the momentum and the spin are coupled, for example $\mathcal{H} \propto \vec{k}.\vec{\sigma}$. This Hamiltonian is time-reversal symmetric, as a time-reversal operation would reverse both the quantum number of spin and the momentum. Indeed, in the plot in Fig.3.6, the dispersion is linear.

ARPES experiments soon followed, focusing on Bi_2Se_3 and Bi_2Te_3. Besides the dispersion relation of the surface (and bulk) states, ARPES experiments can also probe the spin of the extracted electron[54][55][56][57]. The experimental plots presented in Fig. 3.7 show the unicity of the surface state, and the winding of the electron spin around the Fermi surface.

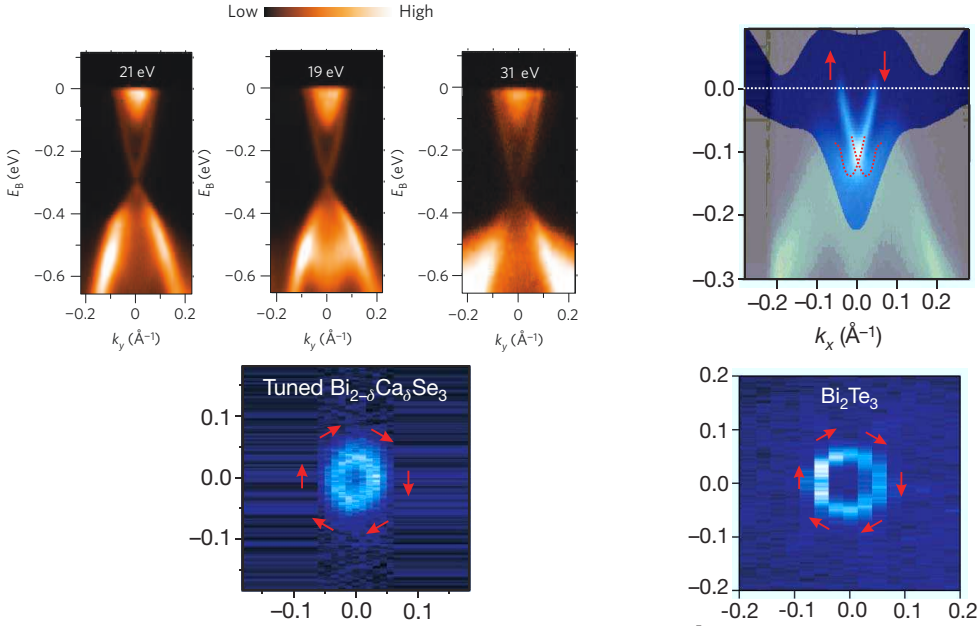

Figure 3.7: ARPES experiments results for Bi_2Se_3 and Bi_2Te_3. The top left[58] shows the dispersion relation of Bi_2Se_3 along one direction ; the brightest areas being the bulk contribution. We can check the linear dispersion of the surface state. Top right : the same results apply for Bi_2Te_3. The grey ares correspond to bulk states[59]. Bottom : the winding of the spin projection around the Fermi surface, left for doped Bi_2Se_3, right for Bi_2Te_3[59].

In these experimental plots, we can notice the unicity of the surface state, showing a linear dispersion and a spin-momentum coupling. These two ingredients are characteristic of Dirac fermions. We can also observe a gap of order of 0.1 eV, larger than in the $Bi_{1-x}Sb_x$ alloy.

3.1.3.2 Scanning tunneling spectroscopy

In addition to the ARPES experiment another technique allows to probe the surface states of a sample, the scanning tunneling microscopy (STM). In a STM experiment, a conducting tip is used to scan a surface, when a voltage bias is applied between the tip and the surface to characterize : electrons can tunnel from the tip to the surface. The tunneling probability is a function of the distance of the tip from the surface, the applied voltage and of the local density of states of the sample, so this method can be used to measure the latest.

The first comparison between ARPES and STM experiments was done in Bi_2Te_3 [15][60], and the integrated density of states derived from ARPES experiment is in good agreement with the STM measurements (cf Fig. 3.8).

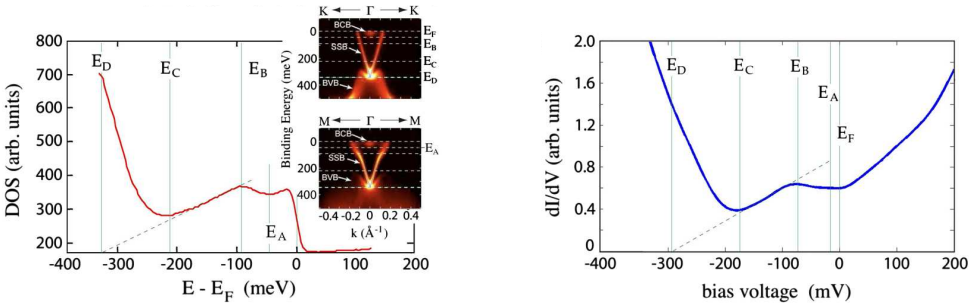

Figure 3.8: Comparison of the integrated density of states obtained from ARPES experiment (left) and from STM experiment (right)[15].

3.1.3.3 Hexagonal warping of the surface state

We can also notice in the inset of the left figure of Fig. 3.8 that there is a deviation of the surface state dispersion from the expected linear behavior. This was seen in ARPES experiments [61], with sections of the conic dispersion at different energies : the Fermi surface evolves from a pure circle to a hexagon and to a snowflake-like shape when the Fermi energy is increased away from the Dirac point.

This has also been confirmed in STM experiments where the density of states is studied on samples with atomic steps at the surface. These steps are obtained when the crystal is cleaved and their height is of the order of a unit cell of the crystal, which in the case of the Bi_2Te_3 consist of 5 atomic layers. In the case of a pure Dirac dispersion, the absence of backscattering implies the absence of stationary state between two steps[62][63]. However, when the Fermi energy reaches the point where the Fermi surface turns from concave to convex, we see the apparition of a stationary state (cf. Fig 3.10), proving the departure from the pure Dirac cone[15].

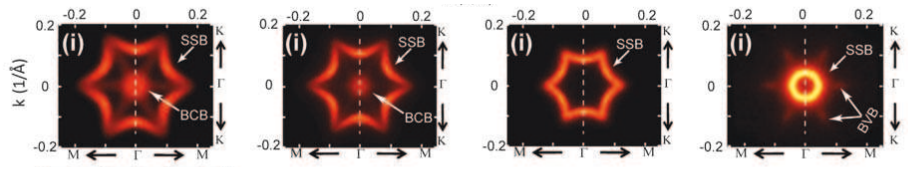

Figure 3.9: Fermi surface of the surface state when the Fermi energy decreases from left to right. SSB (resp. BVB and BCV) refers to the surface state band (resp. bulk valence band and bulk conductance band)[61].

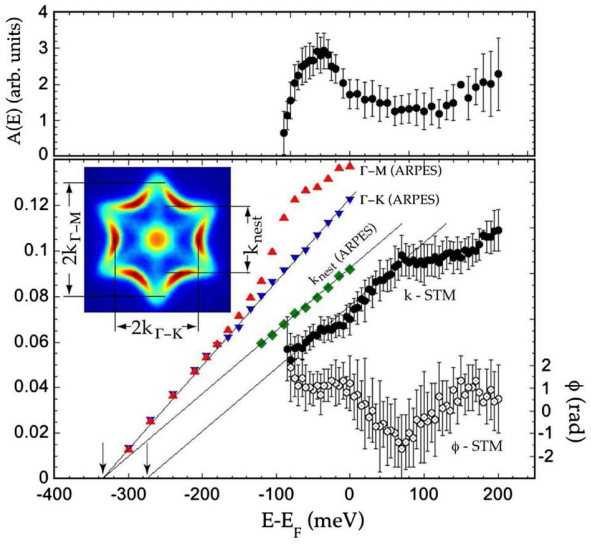

Figure 3.10: The STM experiment results where the amplitude of the presence of a stationary state is plotted as a function of the Fermi energy (top pannel)[15].

The existence of this hexagonal warping of the surface state can be explained theoretically[64] as the combination of the trigonal warping coming from the crystalline structure of the Bi_2Te_3 and the time-reversal symmetry. Taking into account these two symmetries leads to an additional term to the Hamiltonian cubic in momentum which tilts the spin out of the surface plane $\mathcal{H}_W \propto (k_+^3 + k_-^3)\sigma^z$. The corresponding dispersion and projection of the spin are in good agreement with the theoretical description.

This hexagonal warping is also present, even if smaller in amplitude, in Bi_2Se_3 for the same physical reasons. This hexagonal warping is a special feature of topological insulator, since the time-reversal symmetry does not constrain a single Dirac cone in the case of graphene. In graphene, the higher order in $\vec{k}$ terms are also cubic, but only imply a trigonal warping. The implications of this special feature of topological insulator in terms of diffusive

transport are the main object of the Ch. 7 of this thesis.

3.1.3.4 Transport measurements

As we can see in the different ARPES plots I have presented, even if the gap is relatively large, the Fermi energy always lies near from one of the bulk bands (in the plots, the energy is measured with respect to the Fermi energy)[65]. In terms of transport, this means that because of disorder, we are always in presence of conduction from the bulk[66][67][68][69], which is a disadvantage when we want to characterize surface states. The Fermi energy can be changed by chemical doping, e.g. replacing some of the atoms by Ca atoms or vacancies, but this breaks the transitional invariance of the crystal and thus creates some disorder potential[70]. Another way to reduce the bulk conductivity is to improve the bulk to surface ratio, which can be done by using very thin samples, made of a small number of atomic planes[71][72][73][74][75][76][77][78][66][79][80]. Moreover, thin films allow to gate the whole sample more easily[81][82][83].

For example, in Bi_2Se_3 nanoribbons, the presence of a negative magnetoresistance (cf. Fig3.11) has been observed, as expected from the theory explained in Ch. 6.

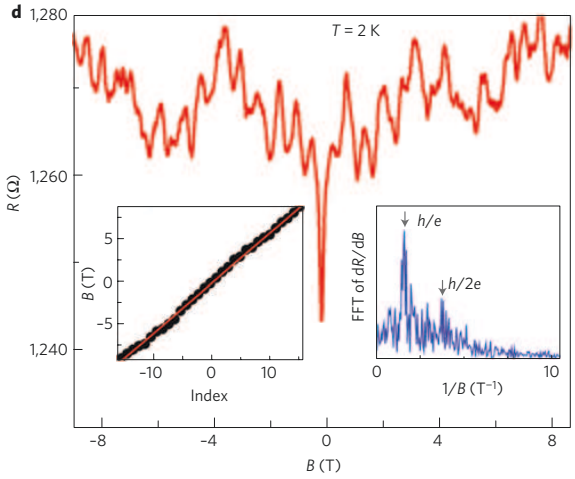

Figure 3.11: Magnetotransport experiment in a Bi_2Se_3 nanoribbon[84].

A similar effect has also been observed in a different kind of topological insulator : strained HgTe. Bulk HgTe is a semimetal, where the conduction and the valence bands touch each other. However, the presence of a stress can open a gap and turns it into a topological insulator. Experimentally, this stress is obtained by depositing the HgTe layers on top of CdTe ; the small lattice constant mismatch is responsible for a distorsion of the HgTe lattice. The

topological insulator strained HgTe has been seen experimentally[16], results are shown in Fig. 3.12.

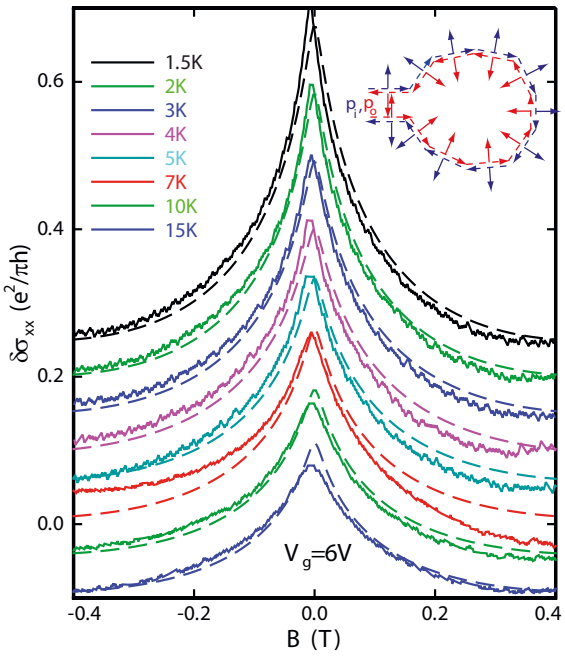

Figure 3.12: Magnetotransport experiment in strained HgTe[16].

Part II

Helical edge states Andreev reflection

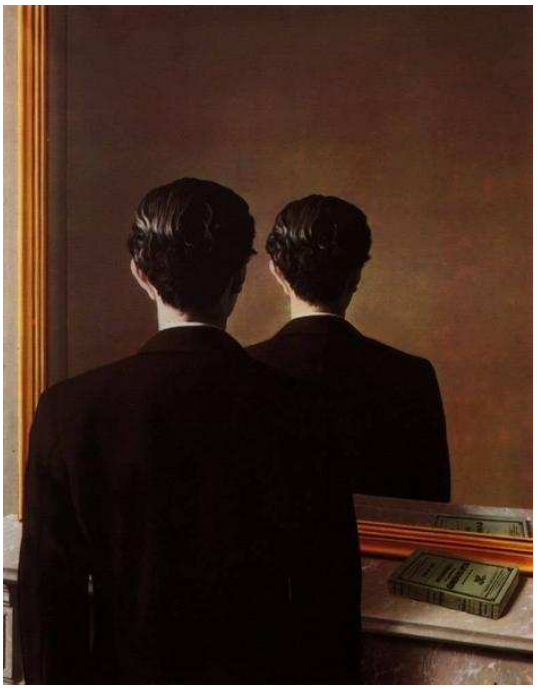

Magritte, La reproduction interdite

A game with shifting mirrors.

Jorge Luis Borges, *Ficciones*

Chapter 4

Cooper pair injection in a QSH edge state

We have seen that the edge states of a quantum spin Hall system, consist in two counter-propaging ballistic channels. If a superconducting region is created in an edge, for example by proximity effect of a superconducting probe, it becomes possible to transfer Cooper pairs into the edge[85]. Cooper pairs are pairs of electrons bound together by an attractive interaction[86][87], in S-pairing superconductors, these electrons have opposite momenta and spins. Because of the conservation of the total spin during the tunneling process from the superconductor to the edge, the two electrons of the same Cooper pair have opposite spins in the edge. The helical nature of the edge states then ensures that the electrons must travel in opposite direction of the edge, hence, this system should provide a perfect Cooper pair splitter. As a comparison, in a standard metal, the electrons can travel in the same direction since it is the total spin that is preserved during the injection and not necessary the total momentum (a rugged interface breaking the translational symmetry). In this chapter, we are going to study this injection of Cooper pairs in a helical edge state.

4.1 Model

To model the propagation of the edge states, we will first assume that the edge is along the x-axis. We will also assume, without any loss of generality, that the electrons moving from left to right at velocity v_F have spin up, and electrons moving from right to left have spin down. Down spin electrons also move at the velocity v_F because of time-reversal symmetry. In the absence of the superconducting probe, and introducing the field operators $\psi_\uparrow$ (resp. $\psi_\downarrow$) associated to the up-spin (resp. down-spin) electrons, the kinetic Hamiltonian

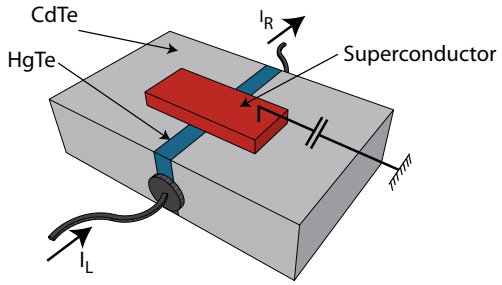

Figure 4.1: Schematic representation of the proposed experimental setup. The Quantum Spin Hall phase is realized in a HgTe/CdTe junction. Transport trough this QSH phase is measured by a standard two terminals setup with normal electrodes. Between these two electrodes, a superconducting electrode is deposited over a length l on one side of the sample.

reads :

$$H_0 = -i\hbar v_F \int_{-\infty}^{\infty} dx \ \left(\psi_\uparrow^\dagger \partial_x \psi_\uparrow - \psi_\downarrow^\dagger \partial_x \psi_\downarrow\right). \tag{4.1}$$

This Hamiltonian shows the ballistic properties of the edge states provided there is no coupling between the two channels. Moreover the velocity is the same at every energy thanks to the linear dispersion : hence the eigenstates satisfy $\psi_\uparrow(x,t) = \psi_\uparrow(x - v_F t, 0)$ and $\psi_\downarrow(x,t) = \psi_\downarrow(x + v_F t, 0)$. To model the superconducting region, we consider an effective pairing potential $\Delta(x)$ which can be related to the pairing potential Δ_0 of the probe through the formula $\Delta(x) = t(x)^2/\hbar\Delta_0$ where $t(x)$ is the tunneling amplitude from the probe to the QSH edge state. This provides the effective Hamiltonian :

$$H = H_0 + \hbar \int_0^l dx \ \left(\Delta^*(x)\psi_\downarrow(x)\psi_\uparrow(x) + \text{H.c.}\right). \tag{4.2}$$

To determine the scattering matrix between the channels, or to express the current operators, we will focus only on the value at the boundaries of this superconducting region, what happens further in the leads being determined by the ballistic propagation of the edge states.

4.2 Cooper pair injection and scattering

We have seen that at a normal metal/superconducting interface (N/S junction), it is possible to inject Cooper pairs from the superconductor into the normal metal. This injection is possible when the potential of the superconductor μ_S is larger than the Fermi energy E_F in the metal. When $\mu_S < E_F$, the Cooper pairs are absorbed from the metal.

An incident electron (resp. hole) from the normal metal, with an energy E below the superconducting gap ($\mu_S - \Delta < E < \mu_S + \Delta$) can not be transmitted

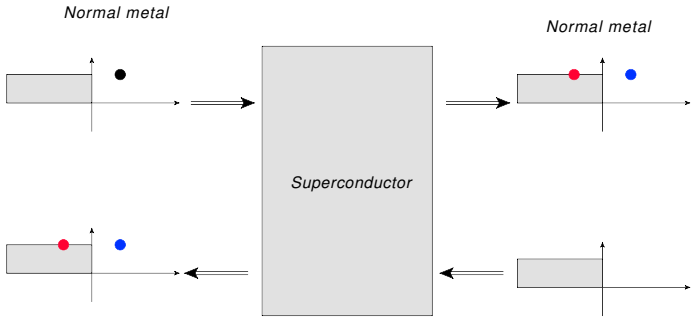

Figure 4.2: Scattering processes at a N/S/N junction. An incoming electron (black) can be reflected or tunnel as an electron (blue), or form a Cooper pair and be either reflected or transmitted as a hole (red). For simplicity reasons, we assumed that the three regions are at equilibrium $\mu_L = \mu_S = \mu_R$ and neglected the temperature dependance $T = 0$.

in the superconductor as a quasi-particle (resp. quasi-hole) because its energy lies in the gap. However, it can be transmitted as a Cooper pair of energy μ_S with another electron (resp. hole) of energy $2\mu_S - E$. The two electrons (resp. holes) must have opposite spins and opposite momenta to form a Cooper pair, consequently this absorption (resp. injection) of a Cooper pair can be effectively described as the retroreflection of the electron (resp. hole) as a hole (resp. electron) of opposite momentum and spin. This retroreflection is known as the *Andreev reflection*[88][89][90].

The study of a normal metal/superconductor/normal metal (N/S/N) junction shows the presence of different processes. If we neglect the Cooper pair absorption, an incoming electron can be reflected at the first interface, or it can tunnel into the second lead. Because of Cooper pair absorption, it can be retroreflected as a hole (Andreev reflection) if it pairs with an electron of the opposite lead, or it can tunnel as a hole (non-local Andreev reflection) when the second electron originates from the same lead (cf Fig. 4.2). These Andreev processes correspond to a transfer of charge $2e$ between the metals and the superconductor, as opposed to the transmission or the reflection as an electron where no charge are transferred.

This effective image of Andreev reflection must be taken with precaution : in a N/S/N junction, the Andreev reflection does not necessarily happen at the interface, since it is the absorption of a Cooper pair formed of electrons originating from different leads we expect the absorption to occur in all the superconducting region.

Now, if we consider a junction of two quantum spin Hall phases with a superconductor (QSH/S/QSH), some of these processes are forbidden by the helicity of the edge states. If we consider that up-spin excitations have to travel from left to right, and down-spin from right to left an incoming electron

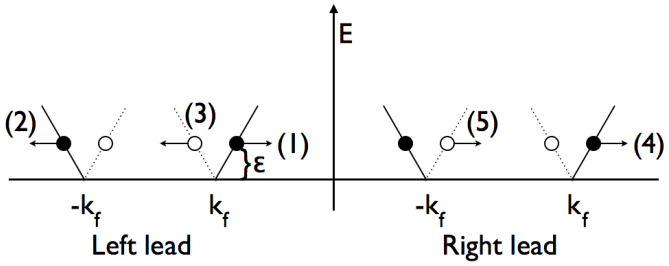

Figure 4.3: Scattering processes. With Fermi liquid leads, an incident electron (1) can be backscattered as an electron (2), reflected as a hole (local Andreev reflection) (3), transmitted as an electron (4) or transmitted as a hole (non local Andreev process) (5). In the QSH edge state, helicity conservation prevents electronic backscattering (2) and hole transmission (5). For a wide superconductor, electron transmission (5) vanishes and only Andreev reflection (3) remains.

is either transmitted or Andreev reflected. The reflection is suppressed because the QSH/S interface can not cause spin-flip of the electron, and the non-local Andreev reflection is impossible since there is no pair of electrons originating from the same lead with opposite spins.

Moreover, in the case of a superconducting region of length $l \gg \xi$ the coherence length, the transmission of a subgap electron vanishes, the conservation of energy then ensures that even if there are defects or a mismatch at the boundary between the QSH edge state and the superconducting region, there will be *perfect* Andreev reflection.

It is important to stress that this perfect Andreev reflection does not occur at the interfaces : in the stationary regime, every possible Cooper pair has been absorbed (or injected) by the superconductor because of its length. If we start with Fermi seas at different potentials μ_L and μ_R for each lead, then the particles flowing out of the superconductor will be Fermi seas at potentials $2\mu_S - \mu_R$ at the right lead, and $2\mu_S - \mu_L$ at the left lead : we observe an effective perfect Andreev reflection at each interface.

As we have seen the equivalence between the Andreev reflection and the injection/absorption of Cooper pairs, we will now on use these two images indifferently.

The study of the injection/absorption of Cooper pairs in a quantum spin Hall edge is equivalent to a scattering problem where electrons can be either transmitted or Andreev reflected. We will in the next section derive the transmission and Andreev reflection amplitudes as a function of the energy of the incoming electron, for the general case of superconducting region of length l.

4.3 Transmission and reflection amplitudes

To determine the amplitude of Andreev reflection and of the transmission, we first use the time-reversal constraint : because of time-reversal symmetry, we expect the amplitudes concerning incoming up-spins electrons, originating from the left reservoir to be related to the down-spins electrons of the right reservoir. Then we will derive these amplitudes in the case of a constant pairing potential.

4.3.1 Time-reversal constraint

The Hamiltonian of Eq. (4.2) can be written as :

$$\mathcal{H} = \int_{-\infty}^{\infty} dx \left[-i\hbar v_F \left(\psi_\uparrow^\dagger \partial_x \psi_\uparrow - \psi_\downarrow^\dagger \partial_x \psi_\downarrow \right) + \hbar \left(\Delta^*(x) \psi_\downarrow(x) \psi_\uparrow(x) + \text{H.c.} \right) \right] , \tag{4.3}$$

where we assumed that the pairing potential vanishes outside the superconducting region ($\Delta(x) = 0$ for $x \leq 0$ or $x \geq l$). It is possible to perform a Bogoliubov transformation to express this Hamiltonian as matrix product. In this case, this transformation reduces to consider eigenvectors of the form $(\Psi_\uparrow \Psi_\downarrow^\dagger)$ instead of $(\Psi_\uparrow \Psi_\downarrow)$ and we can write the Hamiltonian as :

$$\mathcal{H} = \hbar \int_{-\infty}^{\infty} dx \begin{pmatrix} \Psi_\uparrow(\vec{r}) & \Psi_\downarrow^\dagger(\vec{r}) \end{pmatrix} \left[-iv_F \sigma_z \partial_x + \Delta(x) \sigma_x \right] \begin{pmatrix} \Psi_\uparrow^\dagger(\vec{r}) \\ \Psi_\downarrow(\vec{r}) \end{pmatrix} , \tag{4.4}$$

where the σ matrices are Pauli matrices. As a consequence, we are looking for eigenvectors of the matrix :

$$H = -iv_F \partial_x \sigma^z + \Delta(x) \sigma^x . \tag{4.5}$$

This expression of the matrix operator H shows that the problem is doubly degenerate, as we could expect from the time-reversal symmetry. Indeed, if ϕ is an eigenstate of H, then the state defined as $\sigma^x \phi^*$ is also an eigenstate with the same eigenvalue. Conserving only the component of $\sigma^x \phi^*$ orthogonal to ϕ allows to consider a orthogonal basis of eigenvectors ϕ and Φ :

$$\Phi = \sigma_x \phi^* - \langle \phi | \sigma_x \phi^* \rangle \phi . \tag{4.6}$$

On general ground, an eigenstate can be parametrized according to :

$$\phi(x) = \begin{cases} e^{ikx} \binom{1}{0} + r(k) e^{-ikx} \binom{0}{1} & \text{for } x \leq 0 , \\ t(k) e^{ikx} \binom{1}{0} & \text{for } x \geq l . \end{cases} \tag{4.7}$$

The first line corresponds to the solution on the left hand side of the superconducting region, with the superposition of an incoming up-spin electron

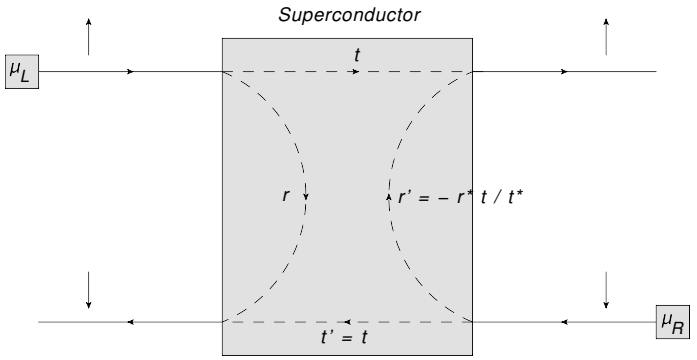

Figure 4.4: Scattering amplitudes for an electron originating from the left t and r, and for an electron originating from the right t' and r'. because of the time-reversal symmetry, these different amplitudes are related.

going from the left to the right and the Andreev reflected part with amplitude $r(k)$, of opposite spin and going from right to left. The second line is just the component of the wavefunction of the excitation transmitted to the other end of the superconducting region, with amplitude $t(k)$. This parametrization of the eigenstate thus gives the tunneling amplitude $t(k)$ and the Andreev reflection amplitude $r(k)$ for electrons originating from the left reservoir.

The calculation of the second eigenstate Φ defined in Eq. (4.6) leads to :

$$\Phi(x) = t^*(k) \times \begin{cases} t(k)e^{-ikx}\binom{0}{1} & \text{for } x \leq 0 \ , \\ e^{-ikx}\binom{0}{1} - \frac{r^*(k)t(k)}{t^*(k)}e^{ikx}\binom{0}{1} & \text{for } x \geq l \ . \end{cases} \tag{4.8}$$

Absorbing $t^*(k)$ in the normalization of the state shows that it corresponds to the process of a down-spin electron originating from the right reservoir partially transmitted and Andreev reflected. The corresponding amplitudes are $t(k)$ for the transmission, and $-\frac{r^*(k)t(k)}{t^*(k)}$ for the Andreev reflection. As expected, the time-reversal symmetry constrain the amplitudes for electrons originating from the right reservoir to be expressed as a function of the amplitudes associated to the left reservoir (cf Fig. 4.4).

We use the relation $\epsilon = \hbar v_F k$ to parametrize the incoming electrons as a function of their energy instead of their momentum. The scattering process we have just derived then reduces to :

$$\begin{aligned} \psi_{\uparrow,out}(\epsilon) &= t(\epsilon)\psi_{\uparrow,in}(\epsilon) - \frac{r^*(\epsilon)t(\epsilon)}{t^*(\epsilon)}\psi^\dagger_{\downarrow,in}(-\epsilon) \ , \\ \psi^\dagger_{\downarrow,out}(-\epsilon) &= r(\epsilon)\psi_{\uparrow,in}(\epsilon) + t(\epsilon)\psi^\dagger_{\downarrow,in}(-\epsilon) \ . \end{aligned} \tag{4.9}$$

We will now derive only the values of the two quantities of interest $t(\epsilon)$ and $r(\epsilon)$ for a given geometry of the superconducting region.

4.3.2 Derivation of the amplitudes for a constant potential

We have seen that the presence of both S-pairing in the superconducting region and helicity of the edge states is responsible for the suppression of normal reflection and Andreev transmission, leading to only transmission or Andreev reflection. This Andreev reflection consists in the reflection of an electron in a hole of opposite spin and *vice-versa*.

From now on we will count the energies with respect to the chemical potential of the superconducting region $\mu_S = 0$. The number of particles is not conserved during this scattering (because of the injection/absorption of Cooper pairs where electrons are reflected in holes) but the introduction of the fields :

$$\chi_+(x,\omega) = \psi_\uparrow(x,\omega) \quad , \quad \chi_-(x,\omega) = \psi^\dagger_\downarrow(x,-\omega) \ , \tag{4.10}$$

maps the problem into a problem of classical scattering on a standard potential instead of a pairing potential. The equations of motions derived from the Hamiltonian read :

$$\left(-i\omega + v_F \frac{d}{dx}\right) \chi_+(x,\omega) = -i\Delta^*(x)\chi_-(x,\omega) \ , \tag{4.11}$$

$$\left(-i\omega - v_F \frac{d}{dx}\right) \chi_-(x,\omega) = -i\Delta(x)\chi_+(x,\omega) \ . \tag{4.12}$$

To solve these equations, we split the space in three regions $x \leq 0$, $0 \leq x \leq l$ and $x \geq l$ corresponding to the regions at the left, under and at the right of the superconducting barrier. We further assume that the pairing potential is constant under the barrier $\Delta(x) = \Delta$. The resolution of these equations by plane waves reads in the superconducting region :

$$\chi_+(x,\omega) = A_+ e^{ikx} + A_- e^{-ikx} \ , \tag{4.13}$$

$$\chi_-(x,\omega) = B_+ e^{ikx} + B_- e^{-ikx} \ , \tag{4.14}$$

with the dispersion relation

$$k(\omega) = \frac{\sqrt{\omega^2 - |\Delta|^2}}{v_F} \quad \text{if } |\omega| \geq |\Delta| \ , \tag{4.15}$$

$$= i\frac{\sqrt{|\Delta|^2 - \omega^2}}{v_F} \quad \text{otherwise} \ . \tag{4.16}$$

An imaginary wave vector corresponds to the tunneling crossing, with an evanescent wave functions that does not vanish at the second interface, even for energies smaller than the gap. Using continuity conditions at the boundaries of the superconducting region $x = 0, l$ allows to express the coefficient $A_\pm$ and

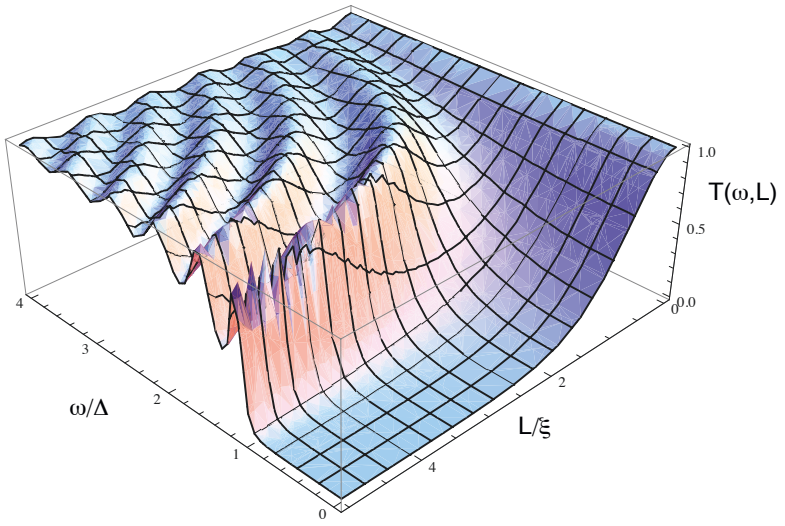

Figure 4.5: Transmission probability through the superconducting barrier, as a function of its length l in units of the superconducting length ξ and of the energy of the incoming electron ω in units of the pairing potential Δ.

$B\pm$ as a function of the incoming fields $\chi_+^{in}(\epsilon) = \chi_+(x=0,\epsilon)$ and $\chi_-^{in}(\epsilon) = \chi_-(x=l,\epsilon)$:

$$\chi_+(x,\epsilon) = \frac{F(l-x,\epsilon)}{F(l,\epsilon)}\chi_+^{in}(\epsilon) + \frac{-2i\Delta\sin(kx)}{F(l,\epsilon)}\chi_-^{in}(\epsilon)\ , \tag{4.17}$$

$$\chi_-(x,\epsilon) = \frac{-2i\Delta^*\sin(k(l-x))}{F(l,\epsilon)}\chi_+^{in}(\epsilon) + \frac{F(x,\epsilon)}{F(l,\epsilon)}\chi_-^{in}(\epsilon)\ , \tag{4.18}$$

where the function F is defined by $F(x,\epsilon) = (v_F k(\epsilon)+\epsilon)e^{-ikx}+(v_F k(\epsilon)-\epsilon)e^{ikx}$.

With this expression of the field inside the superconducting region, it is possible to derive the transmission and Andreev reflection amplitude by looking at these quantities at the boundaries $x = 0, l$:

$$t(\epsilon) = \frac{F(0,\epsilon)}{F(l,\epsilon)} \tag{4.19}$$

$$r(\epsilon) = \frac{-2i\Delta^*\sin(kl)}{F(l,\epsilon)} \tag{4.20}$$

We can check that the probabilities $T(\epsilon) = |t(\epsilon)|^2$ and $R(\epsilon) = |r(\epsilon)|^2$ sum to 1, $T(\epsilon) + R(\epsilon) = 1$ which expresses the conservation of energy.

The transmission probability $T(\epsilon)$ is plotted in Fig. 4.5 as a function of the energy of the incoming electron ϵ and the length of the superconducting region l. In the limit of long barriers $l \to \infty$, for electrons with energy in the gap $|\epsilon| \leq |\Delta|$, the transmission probability vanishes whereas the reflection probability goes to 1: we realize a perfect Andreev reflection.

On the other hand, in the limit of very small barrier $l \to 0$, we recover perfect transmission at every energy, as expected in the absence of the superconductor. The crossover occurs on a length scale corresponding to the superconducting length $\xi = v_F/\Delta$, which can also be interpreted as the penetration length of the subgap excitations. Finally, we observe oscillations arising from multiple scattering of the excitation at the two barriers $x = 0, l$.

4.4 Supercurrent and current-current correlations

4.4.1 Supercurrent

The current in the right and left lead are counted positive from left to right and then defined as :

$$I_L(t) = -ev_F(\psi^\dagger_\uparrow\psi_\uparrow - \psi^\dagger_\downarrow\psi_\downarrow)(x=0,t)\ , \tag{4.21}$$

$$I_R(t) = -ev_F(\psi^\dagger_\uparrow\psi_\uparrow - \psi^\dagger_\downarrow\psi_\downarrow)(x=l,t)\ . \tag{4.22}$$

We express these currents as a function of the field operators incoming or outgoing of the superconductors as :

$$I_L(t) = -ev_F(\psi^\dagger_{\uparrow,in}\psi_{\uparrow,in} - \psi^\dagger_{\downarrow,out}\psi_{\downarrow,out})(t)\ , \tag{4.23}$$

$$I_R(t) = -ev_F(\psi^\dagger_{\uparrow,out}\psi_{\uparrow,out} - \psi^\dagger_{\downarrow,in}\psi_{\downarrow,in})(t)\ . \tag{4.24}$$

With the scattering matrix derived previously in Eq.4.9, it is possible to express the outgoing fields as a function only of the incoming fields. This scattering matrix is defined for every energy, as opposed to the time, and we assume to be in a stationary regime, so it is easier to derive the temporal Fourier transform of the currents. Moreover the incoming fields are considered to be at equilibrium in the reservoirs which allows to write $\langle(\psi^{in}_\uparrow)^\dagger(\epsilon)\psi^{in}_\uparrow(\epsilon')\rangle = \frac{h}{v_F}n_\uparrow(\epsilon)\delta(\epsilon-\epsilon')$ (and similarly for the down spin) where $n_\uparrow$ (resp. $n_\downarrow$) is the equilibrium distribution in the left (resp. right) reservoir with a chemical potential $\mu_L = eV_L$ (resp. $\mu_R = eV_R$).

For the current in the left lead, this leads to the operator :

$$\begin{aligned} I_L(\omega) = -\, ev_F \int \Big[&\psi^\dagger_{\uparrow,in}(\epsilon)\psi_{\uparrow,in}(\epsilon+\hbar\omega) - (r(-\epsilon)\psi_{\uparrow,in}(-\epsilon) + t(-\epsilon)\psi^\dagger_{\downarrow,in}(\epsilon)) \\ &\Big(r^*(-\epsilon-\hbar\omega)\psi^\dagger_{\uparrow,in}(-\epsilon-\hbar\omega) + t(-\epsilon-\hbar\omega)\psi_{\downarrow,in}(\epsilon+\hbar\omega)\Big)\Big]\, d\epsilon\ . \end{aligned} \tag{4.25}$$

There are two different contributions to the current in this expression : the contribution of the voltage bias between the two leads $I = \frac{e^2}{h}(V_L - V_R)$

reflecting the existence of a single ballistic channel in each direction, and secondly the current injected by the superconductor I_S. Hence the presence of the superconductor is described by the supercurrent operator defined as :

$$I_S(t) = I_R(t) - I_L(t) = (-ev_F) \sum_{\sigma=\uparrow,\downarrow} \left[\psi^\dagger_{\sigma,out}(t)\psi_{\sigma,out}(t) - \psi^\dagger_{\sigma,in}(t)\psi_{\sigma,in}(t) \right]. \tag{4.26}$$

Similarly we express its Fourier transform as a function of the incoming fields :

$$\begin{aligned} I_S(\omega) = (-ev_F) \int_{-\infty}^{\infty} \frac{d\epsilon}{2\pi\hbar} \Big[& A_{\varepsilon,\omega}\ \psi^\dagger_{i,\uparrow}(\epsilon)\psi_{i,\uparrow}(\epsilon+\hbar\omega) \\ & + B_{\varepsilon,\omega}\ \psi_{i,\downarrow}(-\epsilon)\psi^\dagger_{i,\downarrow}(-\epsilon-\hbar\omega) + \quad C_{\varepsilon,\omega}\ \psi_{i,\downarrow}(-\epsilon)\psi_{i,\uparrow}(\epsilon+\hbar\omega) \\ & + D_{\varepsilon,\omega}\ \psi^\dagger_{i,\uparrow}(\epsilon)\psi^\dagger_{i,\downarrow}(-\epsilon-\hbar\omega) \Big], \end{aligned} \tag{4.27}$$

with

$$A_{\varepsilon,\omega} = t^*(\epsilon)t(\epsilon+\hbar\omega) - r^*(\epsilon)r(\epsilon+\hbar\omega) - 1, \tag{4.28}$$

$$B_{\varepsilon,\omega} = -t^*(\epsilon)t(\epsilon+\hbar\omega) + \frac{r(\epsilon)t^*(\epsilon)}{t(\epsilon)} \frac{r^*(\epsilon+\hbar\omega)t(\epsilon+\hbar\omega)}{t^*(\epsilon+\hbar\omega)} + 1, \tag{4.29}$$

$$C_{\varepsilon,\omega} = -t^*(\epsilon)r(\epsilon+\hbar\omega) - r(\epsilon)t(\epsilon+\hbar\omega)\frac{t^*(\epsilon)}{t(\epsilon)}, \tag{4.30}$$

$$D_{\varepsilon,\omega} = -r^*(\epsilon)t(\epsilon+\hbar\omega) - r^*(\epsilon+\hbar\omega)t^*(\epsilon)\frac{t(\epsilon+\hbar\omega)}{t^*(\epsilon+\hbar\omega)}. \tag{4.31}$$

Expressing the equilibrium of the incoming fields with the reservoir, and the conservation of energy $R(\epsilon) + T(\epsilon) = 1$, the zero-frequency component of the supercurrent simplifies towards :

$$\langle I_S \rangle = \frac{2e}{h} \int R(\epsilon) \left(n_\uparrow(\epsilon) + n_\downarrow(-\epsilon) - 1 \right) d\epsilon \,. \tag{4.32}$$

This equation shows that the supercurrent is made by injecting or absorbing Cooper pairs naturally : first the multiplying factor of 2 in front of the quantum of conductance corresponds to the total charge $2e$ of a Cooper pair. Secondly, the integral counts the number of Cooper pairs injected : the Andreev reflection probability $R(\epsilon)$ is also the probability to inject/absorb a Cooper pair, as we have seen in Sec. 4.2, and the term between the brackets $n_\uparrow(\epsilon) + n_\downarrow(-\epsilon) - 1$ accounts for the existence of occupied (resp. available) states of opposite spins and energy in the edge to be absorbed as (resp. to inject) a Cooper pair.

At zero bias $\mu_L = \mu_R$ the equation for the supercurrent leads to the differential conductance :

$$\left(\frac{\partial \langle I_S \rangle}{\partial V} \right)_{V=0} = \frac{4e^2}{h} R(\epsilon = 0) \,. \tag{4.33}$$

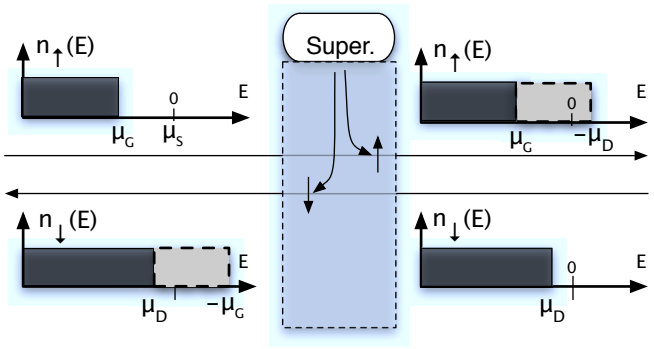

Figure 4.6: Schematic representation of the Cooper pair injection by the superconductor in the QSH edges. The $T = 0$ distribution function of the incoming electrons from the reservoirs at chemical potential μ_G, μ_D are represented. In the distribution function for the electrons leaving the junction, the grey area correspond to the states accessible for the injection of Kramers pair by the superconductor. The case of small junction correspond to an imperfect injection of pairs : the associated partitioning noise is associated with the appearance of cross-correlation of noise in the injected current on both side of the junction. For large junction, all the accessible electronic states are injected in the QSH edges : the injected current on both sides are maximal, but perfectly noiseless.

This differential conductance goes from 0 in the absence of superconductor $l \to 0$, to the maximal value of $4e^2/h$ in the limit $l \gg \xi$ of long superconducting region. This value of $4e^2/h$ corresponds to two metallic channels in parallel with perfect Andreev reflection at the interface with a superconductor (2 times an interface where a charge 2e is transmitted).

4.4.2 Current-current correlators

Having derived the mean-value of the supercurrent, we now consider the second cumulant, the noise of the current. This amounts to consider for example $\langle I_S(\omega) I_S(\omega') \rangle$. Expressing each current as a function of the incoming fields only, terms containing 4 fermionic fields operator appear. To relate these products to the equilibrium distribution of the reservoir we apply the Wick's theorem, expressing the mean value of a product of 4 terms as a combination of mean values of product of two terms :

$$\langle abcd \rangle = \langle ab \rangle \langle cd \rangle + \langle ad \rangle \langle bc \rangle - \langle ac \rangle \langle bd \rangle \ . \tag{4.34}$$

The minus sign in front of the third term comes from the anticommutation rule for the fermionic operators ; it should be replaced by a plus sign in the case of bosonic operator (for example in quantum optics).

Applying the Wick's theorem in our problem, we obtain the current-current correlator :

$$\left\langle I_S(\omega) I_S(\omega') \right\rangle = 2\pi S(\omega)\ \delta(\omega+\omega'), \tag{4.35}$$

where:

$$\begin{aligned} S(\omega) =& \frac{e^2}{h}\int_{-\infty}^{\infty} d\epsilon\ A_{\varepsilon,\omega}A_{\varepsilon+\omega,-\omega}\ n_\uparrow(\epsilon)(1-n_\uparrow(\epsilon+\hbar\omega)) \\ &+ \frac{e^2}{h}\int_{-\infty}^{\infty} d\epsilon\ B_{\varepsilon,\omega}B_{\varepsilon+\omega,-\omega}\ n_\downarrow(-\epsilon-\hbar\omega)(1-n_\downarrow(-\epsilon)) \\ &+ \frac{e^2}{h}\int_{-\infty}^{\infty} d\epsilon\ C_{\varepsilon,\omega}D_{\varepsilon+\omega,-\omega}\ (1-n_\downarrow(-\epsilon))(1-n_\uparrow(\epsilon+\hbar\omega)) \\ &+ \frac{e^2}{h}\int_{-\infty}^{\infty} d\epsilon\ D_{\varepsilon,\omega}C_{\varepsilon+\omega,-\omega}\ n_\uparrow(\epsilon)n_\downarrow(-\epsilon-\hbar\omega)\ . \end{aligned} \tag{4.36}$$

These expressions provide the noise correlator at finite frequency. If we are interested in the low-frequency noise, this expression simplifies at zero frequency into :

$$\begin{aligned} S(\omega\to 0) &= \frac{8e^2}{h}\int R(\epsilon)\left(n_\uparrow(1-n_\uparrow)+n_\downarrow(1-n_\downarrow)\right)(\omega)\,d\epsilon \\ &+ \frac{8e^2}{h}\int R(\epsilon)\,T(\epsilon)\left((n_\uparrow+n_\downarrow-1)(\omega)\right)^2 d\epsilon\,. \end{aligned} \tag{4.37}$$

where for simplicity we noted $n_\uparrow = n_\uparrow(\epsilon)$ and $n_\downarrow = n_\downarrow(-\epsilon)$ The first term is the thermal contribution of the reservoirs : in the case of zero temperature, the equilibrium distribution take the values 0 or 1, so this first term vanishes. Moreover, when the bias voltage V goes to zero, the second term vanishes, and the noise satisfies the Johnson-Nyquist relation $S0 = 4k_BT(\langle\partial I_S\rangle/\partial V)_{V=0}$ The second term represents the non equilibrium contribution to the superconducting current noise associated with Andreev reflection/ normal transmission partitioning, since it vanishes in the case of a perfectly transmitted or perfectly reflected process. Since only Andreev reflexion is associated with Cooper pair emission or absorption from the superconductor, the partitioning between Andreev reflection processes and normal transmission is at the origin of the excess noise in the superconducting current.

4.4.2.1 Excess noise

To study the excess noise coming from the Andreev reflection/normal transmission partionning, we focus on the zero-temperature limit. In the case of small biases $\mu_L = \mu_r = V$, only partially transmitted electrons will contribute to the noise, and for the pairing potential profile we used $\Delta(x) = \Theta(x)\Theta(l-x)$, the response of this noise to the bias is :

$$\frac{\partial S}{\partial \mu} = \frac{16e^2}{h}\,\frac{\sinh^2(l/\xi)}{\cosh^4(l/\xi)}\,. \tag{4.38}$$

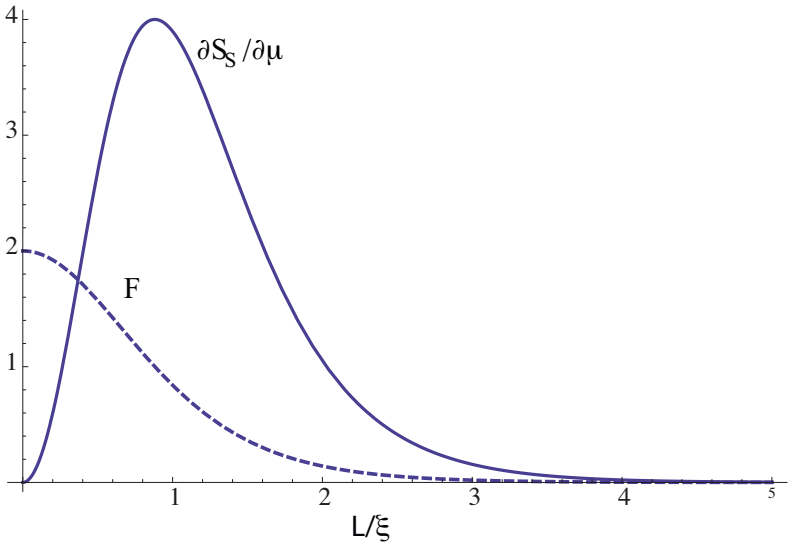

Figure 4.7: Noise response $\frac{\partial S}{\partial \mu}$ in units of e^2/h and Fano factor $F = S/2e\langle I_S\rangle$ (dashed curve) as a function of l/ξ.

As we can see on the Fig.4.7, two regimes correspond to a vanishing noise : in the case of a very short superconducting region, we neglect the presence of the superconductor, and we recover two independent channels, noiseless because they are at equilibrium with the reservoir. This is the expected behavior since there is no partitioning when when the transmission probability is 1. The regime of long superconducting region can be understood as a regime where every possible absorption or injection of Cooper pairs have been performed. In stationary regime, this is equivalent to a conversion from supercurrent to quasi particle current through the perfect Andreev reflection.

As expected, the maximum noise is observed when the length of the superconducting region equals the superconducting length $l = \xi$, where the reflection and transmission probabilities are equal to $1/2$.

We also derived the Fano factor $F = S/2e\langle I_S\rangle$ and found that $F = 2T(\epsilon = 0)$ (dashed curve of Fig.4.7), consistent with the charge $2e$ of the Cooper pairs transmitted between the QSH edge states and the superconductor.

A strong test of the helical properties of the edge states is obtained by considering transport when $\mu_G = -\mu_D \neq 0$. In this case, at zero temperature the superconducting current as well as its excess noise vanish since the electron distribution sent from the reservoirs is such that no Cooper pair can be emitted within the superconductor thus leading to the simultaneous vanishing of the superconducting current and its fluctuations. However, if normal

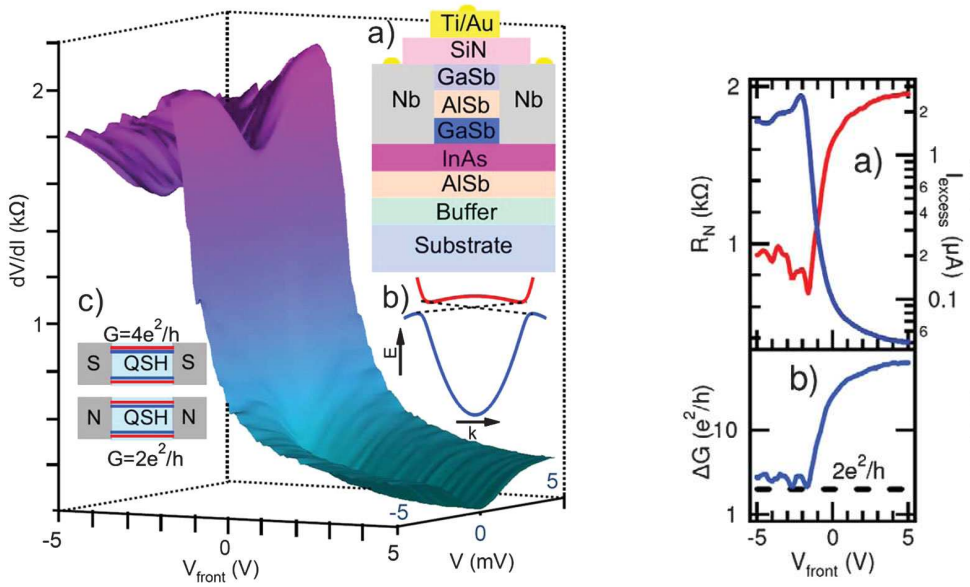

Figure 4.8: Left : Experimental plot of the resistance of a S/QSH/S junction, as a function of the Fermi energy of the QSH phase V_{front}, and the bias voltage between the two superconductors V. Inset a) shows the a cross section of the device. Inset b) shows a typical dispersion relation, the plain lines representing bulk states, the dashed lines the helical edge states[91]. Right : Experimental plots extracted from the left panel[91]. Inset a) shows the value of the normal resistance (blue) as a function of the Fermi energy, controlled by V_{front}. For $V_{front} < 2$ V, the insulating regime is reached. Inset b) is a plot of the excess conductance ΔG as a function of the Fermi energy. When the Fermi energy is in the gap, we observe fluctuations of ΔG around $2e^2/h$.

backscattering (or non local Andreev transmission) is possible, the partitionning between reflected and transmitted electrons will produce noise, increasing with the value of $\mu_G = -\mu_D$.

4.5 Experimental application

This link between Andreev reflection and helical edge states has been used[91] to show the helical properties of the edge states of InAs/GaSb quantum wells. Their experimental setup, inset a) of the left panel Fig. 4.8 is made of a GaSb/InAs quantum well, contacted by 2 superconducting Nb probes. Helical edge states have been reported in such quantum wells, and there are represented by the dashed lines in the inset b).

The top gate Ti/Au allows to tune the Fermi energy in the insulating regime.

We observe in the left panel of Fig. 4.8 the crossing from the normal metal regime to insulating regime when V_{front} decreases below 0V. In the insulating regime, we observe a zero-bias conductivity peak (ZBCP). This ZBCP is related to the Andreev reflection probability as only Cooper pairs can be injected in the QSH phase. We expect this peak in conductivity when the two superconductors are at the same potential, if not, the absorption by a superconducting lead of a Cooper pair injected by the other is forbidden because of the energy mismatch.

Since we have a single channel to transport Cooper pairs of charge $2e$, we expect the total conductance to be $R(E_F) \times 2e^2/h$, where $R(E_F)$ is the Andreev reflection probability at the the Fermi energy, measuring the efficiency of the Cooper pair injection. Extracting the excess conductance $\Delta G(V_{front}) = G(V_{front}, V = 0) - G(V_{front}, V \gg \Delta_s/e)$ from the measurement of the left panel Fig. 4.8, we obtain the plot of the inset b) of the right panel Fig. 4.8, and we observe that in the insulating regime, $\Delta G = 2e^2/h$. This is strong indication that there is perfect Andreev reflection at the interface between the InAs/GaSb quantum well and the Nb superconducting probe : there are helical edge states in the quantum well.

Part III

Diffusion of Dirac fermions at the surface of the topological insulators

xkcd.com

- Sheldon, what the hell are you doing ?
- The same thing I've been doing for three days. Trying to figure out why electrons behave as if they have no mass when traveling through a graphene sheet.

The Big Bang Theory

Chapter 5

Diffusion of Dirac fermions

5.1 Introduction

5.1.1 Dirac fermions

We have seen that topological insulators are a new phase of matter characterized by an insulating bulk and conducting edge or surface states, explaining why the transport experiments could be described only by what happens at the edge or the surface[92]. In this chapter, we are interested in 3 dimensional topological insulators, and we have seen in Ch.3 that their surface states are described by massless Dirac fermions with a Hamiltonian $\mathcal{H} \propto \vec{\sigma}.\vec{p}$.

We remind that this can be understood as the combination of three phenomena : the dependance in momentum of the surface states, the momentum-spin locking and time-reversal symmetry :

- when the dispersion bands of the surface states cross, the lowest-order dependance of the momentum should be linear. If one wants to remain in the topological insulator regime, the Fermi energy should remain in the small gap opened between the bulk conductance and valence bands, this is why we can neglect highest-order terms in a first approximation
- because of the momentum-spin locking, we know that the Hamiltonian should exhibit a term linking spin and momentum, and the time-reversal symmetry implies that in this term, the spin should appear to a odd power.

Finally, the isotropy of the problem explains the same coefficient in front of the two terms.

These Dirac fermions are not specific to topological insulators since they also appear in graphene, a pure 2 dimensional crystal of carbon atoms. The experimental realization of graphene in 2004 [93] raised interest in the study of the transport properties of Dirac fermions[94], as their behavior differs from the non-relativistic case (here their energy increases as the momentum, not the

square of the momentum), we expect their transport properties to be distinct. In particular, in the case of real materials, we can not create perfectly clean samples : in every crystal, impurities such as vacancies or different atoms break the translational invariance. In the limit of a good sample, where the number of impurities is small (we will define in Sec.5.1.3 what this "small" number is), we can consider that the electrons scatter on the impurities, like a pinball : it is the diffusive regime. For pedagogical purpose we will remind in this chapter the result for the diffusion of Dirac fermions[95][96], and the corresponding derivation of the conductivity, the quantum correction to the conductivity, and the universal conductance fluctuations in the case of Dirac fermions in Ch. 6. These results are applicable to both graphene and topological insulators surface states.

However, there are important differences between the two dimensional metal that is graphene, and the topological insulator surface states :

- in the expression of the Hamiltonian $\mathcal{H} \propto \vec{\sigma}.\vec{p}$, the σ matrix relates to the magnetic spin only for the surface states (it relates to a sublattice partition in graphene), so magnetic fields effect should be different ;
- in the case of graphene, there is an even number of Dirac cones (precisely 4, 2 for the spin degeneracy, and 2 for the valley degeneracy) whereas there is an odd number for topological insulators. This means that in the limit of a strong disorder that do not close the gap, graphene would be localized as opposed to topological insulator surface states : there is at least one surface state that cannot couple to another, and remains conductive[97] ;
- the time-reversal symmetry that is crucial in 3 dimensional topological insulators affects the Dirac cones differently. In topological insulator, the cone must respect this symmetry, whereas in graphene, a cone is projected into the cone of the other valley by time-reversal operation ;
- as a consequence, the departure to Dirac physics at high Fermi energy is different : the Dirac cones of graphene present a triangular warping whereas the warping is hexagonal for topological insulators.

We will study in Ch. 7 the specificities of topological insulators surface states, in particular this hexagonal warping, and the effects of a magnetic field.

5.1.2 Regime of coherent transport

At macroscopic scales, electronic transport through a material is described by the Ohm's law $U = RI$. In this equation, the constant R relating the number of electron I crossing the sample per unit of time when a difference of potential U is applied, is called the resistance and is a function of the material used and the size of the sample. To express the dependance in the size of the

Figure 5.1: Left : principle of the diffraction of the light by a circular hole, right : diffraction pattern observed. Pictures from *Atlas de phénomène d'optiques*, Springler-Verlag

sample one has to introduce the resistivity r, a constant of the material, and gets in the case of a sample of length l and transverse surface S a resistance $R = rl/S$. This formula provides the traditional result for the composition of resistances whether it be in series or in parallel. However, at very small scales, for example at the order of the atom, the classical world as we know it no longer exists, and we have to take into consideration the quantum mechanics, where electrons can no longer be described as particles but also present a wave behavior characterized by the Fermi wavelength λ_F.

A specificty of wave physics is that t is possible to observe interferences, for example with light in a diffraction experiment : when a laser beam is sent through a tiny hole, the result on a screen behind the hole shows an alternating scheme of bright parts and shadows. When the laser beam is changed by a bulb light, the interference pattern disappears, the reason being that all the photons coming out of the laser beam are in the same quantum state (same direction and same frequency), and they exit the laser cavity with the same phase, they are said to be coherent. The photons coming from a light bulb present a wide range of different frequencies and directions, they are said to be incoherent. The phase of the incoherent photons is random on the screen whereas it is deterministic in the case of coherent light, this is why we can see the interference patterns, which are a reminiscence of the information of the phase.

Similarly, to see interference effects with electrons, we need to conserve their phase coherence. There is a variety of phenomena responsible for the loss of the phase coherence, for example interactions between the electrons, or interactions between the electrons and the vibration of the atoms of the lattice (called phonons) for example. These inelastic processes where an electron can exchange energy modify the phase of the electron, and the repetition of many events of this type leads to the introduction of a length, called *coherence length*, giving an estimation of the length an electron can travel before losing memory of its initial phase.

The *mesoscopic* regime of coherent transport corresponds to the regime

where we can treat the electrons as particles that can interfere. This corresponds to the regime where the size of the sample L is comparable with the phase coherence length L_ϕ, and $\lambda_F \ll L$ in order to treat the electrons as particles.

5.1.3 Diffusive transport

In the nature it is merely impossible to have *clean* crystals : even in the cleanest atmosphere, the presence of residual impurities at random positions creates a random disorder potential that scatters particles. Since the scattering is elastic, there is no exchange of energy between the electron and the scatterer, so it does not affect the coherence length. To characterize the strength of this disorder, it is useful to introduce the mean-free path traveled by an electron between two scattering events l_e. With a semi-classical picture, we can see the movement of the electron as a particle bouncing on the impurities, moving by nearly l_e between each scattering event ; in the limit where $l_e \to 0$, this random walk is called a diffusion. If we want to remain in this semi-classical picture, this length l_e has to be larger than the Fermi wavelength λ_F : the Fermi wavelength can be seen as the size of the cloud where the electron can be found, if this size is similar to l_e, this cloud sees different scattering events at the same time and the picture of the bouncing ball is no longer valid. The mean-free path should also be smaller than the size of the sample to have a large number of scattering events, and if we want to remain in the coherent regime, it should also be smaller than L_ϕ. In the end we have this scale between all the lengths :

$$\lambda_F \ll l_e \ll L, L_\phi \ . \tag{5.1}$$

This scale between all the lengths also provides a relation between the Fermi energy and the disorder strength. As long as $\lambda_F \ll l_e$, the disorder strength is smaller than the Fermi energy, this is the weak disorder regime in opposition to the strong disorder regime where the mean-free path is comparable with the Fermi wavelength. The works presented in this thesis were done in the weak-disorder regime, in particular the diagrammatic technique presented in Sec. 5.3 is a series expansion in order of λ_F/l_e.

5.1.4 Model

Dirac fermions

We have seen in Ch. 3 that the massless Dirac fermions we want to describe obey an equation $\mathcal{H} \propto \vec{\sigma}.\vec{p}$. In the case of topological insulators surface states, the simplest Hamiltonian describing the ARPES experimental plots is $\mathcal{H} = \hbar v_F(k_x\sigma^y - k_y\sigma^x)$. Without any loss of generality, we perform a rotation around the spin z-axis and we will use for the Dirac fermions the kinetic Hamiltonian :

$$\mathcal{H}_0 = \hbar v_F(k_x\sigma^x + k_y\sigma^y) \ . \tag{5.2}$$

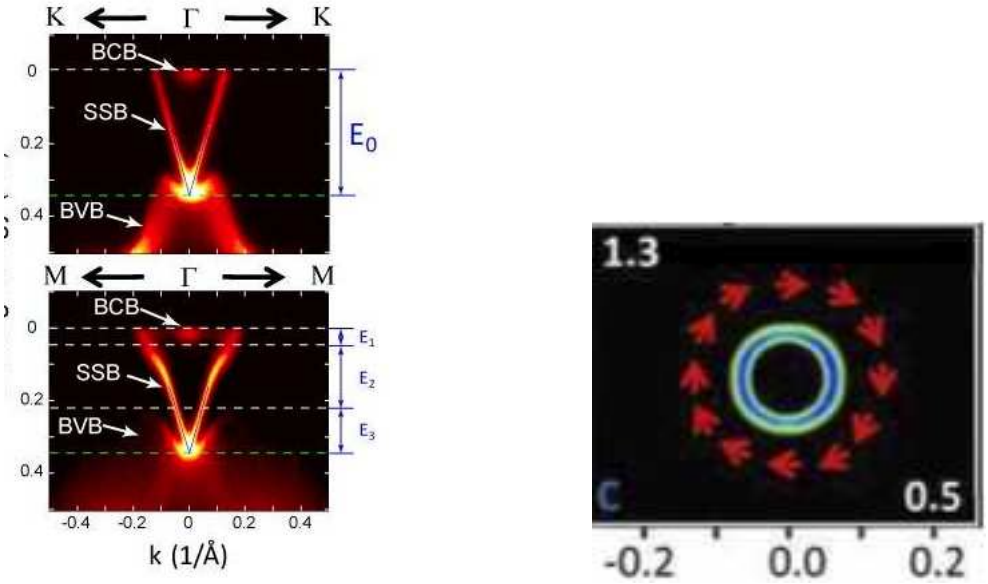

Figure 5.2: Left : ARPES data showing the linear dispersion of the topological insulator Bi_2Te_3 surface states labeled SSB, BVB and BCB being the bulk bands [61]. Right : ARPES data showing the Fermi surface of topological insulator Bi_2Te_3 surface state, with projection of the spin in red arrows for every direction [98].

The dispersion relation shows the linear behaviour of the the massless Dirac fermions, and also the momentum-spin locking observed experimentally (cf. Fig.5.2). In the Hamiltonian, the spins points toward the center of the Fermi surface instead of winding around the surface, but as expected, we recover the same physics if we perform a rotation of the spins around the z-axis.

Disorder

To introduce the disorder responsible for diffusion in our study, we use a standard model where the impurity potential profile is described as a scalar gaussian disorder potential $V(\vec{r})$, characterized by its mean value and its second cumulant. We introduce the notation $\langle ... \rangle$ to describe the mean-value of a quantity averaged over many realizations of the disorder (e.g. different samples). In our model, we define the zero of energies such that $\langle V(\vec{r}) \rangle = 0$, and the second cumulant can be written as $\langle V(\vec{r}) V(\vec{r'}) \rangle = \gamma \delta(\vec{r} - \vec{r'})$. This value of the second-cumulant shows that we do not consider any correlation in space between different scatterer positions, this is why this model is called uncorrelated gaussian disorder. This corresponds to localized scatterers centers for non magnetic impurities that do not couple to the spin of the electron. Besides its simplicity in calculations, this model is useful in the sense that it is a

limit of dilute impurities at concentration n_{imp} at positions $\vec{r_i}$ with a potential $v_0\delta(\vec{r}-\vec{r_i})$, when the density goes to infinity keeping $n_{imp}v_0^2 = \gamma$ constant [32].

5.2 Boltzmann equation

5.2.1 Hamiltonian diagonalization, density of states

Starting from the kinetic Hamiltonian given before we have :

$$\mathcal{H} = \hbar v_F(k_x\sigma^x + k_y\sigma^y) = \begin{pmatrix} 0 & \hbar v_F k_- \\ \hbar v_F k_+ & 0 \end{pmatrix} , \tag{5.3}$$

where $k_\pm = k_x \pm ik_y$.

This Hamiltonian is easy to diagonalize, and we get $E = \pm\hbar v_F k$. This confirms the linear dispersion relation, and justifies the notation v_F for the Hamiltonian parameter as it is the Fermi velocity, constant for Dirac fermions, as opposed to the usual case where it varies as a function of the Fermi energy. The eigenvectors are a tensorial product of an external spatial component corresponding to a plane wave of wavevector $\vec{k}$ and a spin component given by :

$$|\vec{k}\rangle^\pm = |\vec{k}\rangle_{ext.} \otimes |\vec{k}\rangle_s^\pm , \tag{5.4}$$

$$|\vec{k} = (k,\theta)\rangle_s^\pm = \frac{e^{i\vec{k}.\vec{r}}}{\sqrt{2}} \begin{pmatrix} 1 \\ \pm e^{i\theta} \end{pmatrix} . \tag{5.5}$$

This dependance of the spinorial part of the eigenvector on the direction θ of the wavevector is of importance in the study of the scattering as we will see later. This dependance is also responsible for the rotation of the polarization around the Fermi surface: the polarization of the spin $\vec{s}$ in the x,y plane is the vector ${}_s\langle\vec{k}|\vec{\sigma}|\vec{k}\rangle_s$. For the eigenvector of positive energy $E = \hbar v_F k$, we find that the polarization is given by the vector $\vec{s} = \cos\theta\vec{e_x} + \sin\theta\vec{e_y}$ and thus is locked to the direction given by the momentum.

Since we are only interested in the insulating regime of the topological insulators and do not consider the bulk contributions, we assume the gap between the bulk bands to be large enough to ensure that the Fermi energy lies in it. In the regime of weak disorder described in Sec. 5.1.3, we assume that the Fermi energy is the second largest scale of energy of the problem after the gap.

Having the (linear) dispersion relation, we can derive the density of states $\rho(E) = \sum_\pm \int \frac{d\vec{k}}{(2\pi)^2}\delta(E - E_\pm(\vec{k}))$ and obtain the relation :

$$\rho(E) = \frac{|E|}{2\pi\hbar^2 v_F^2} . \tag{5.6}$$

There is a large density of state far from the Dirac point where lies the Fermi energy in the regime of weak disorder, so the surface states correspond

Figure 5.3: Left : projection of the spin for different eigenvectors around the Fermi surface. Right : representation of the different scale of energies in the regime of weak disorder. The dotted line around the Fermi energy line correspond to the states relevant to transport. The energies are counted with respect to the Dirac point.

to a good metal. This means that the Fermi energy is large enough, and since the transport is due to excitations near the Fermi surface, we can focus only on the state near this positive Fermi energy and neglect the eigenstates of negative energies(cf Fig. 5.3).

5.2.2 Elastic scattering time

These eigenstates are scattered one into the other by the presence of the disorder potential. Using the Fermi golden rule, the elastic mean-free time between two scattering events reads :

$$\frac{1}{\tau_e(E_F)} = \langle \int \frac{d\vec{k'}}{(2\pi)^2} \quad \frac{2\pi}{\hbar} |\langle \vec{k'}|V|\vec{k}\rangle|^2 \delta(E(\vec{k'}) - E_F)\rangle \ . \tag{5.7}$$

Using the relation $\langle V(\vec{r})V(\vec{r'})\rangle = \gamma\delta(\vec{r}-\vec{r'})$ for the second cumulant of the disorder, and introducing the density of states, we obtain the elastic scattering time as a function of the strength of the disorder γ, the greater the disorder, the shorter the mean-free time :

$$\frac{\hbar}{\tau_e(E_F)} = \pi\rho(E_F)\gamma \ . \tag{5.8}$$

We observe that there is a factor of difference of 2 compared to the usual relation $\hbar/(2\tau_e) = \pi\rho\gamma$ in the case of non relativistic electrons. This comes from the anisotropy of the scattering probability from a wavevector $\vec{k}$ to a wavevector $\vec{k'}$ on the Fermi surface. Even if the scalar potential is isotropic, this scattering is not : because of the spinorial nature of the excitation, the scattering amplitude is proportional to the overlap between the two spinors, and we have seen that there is a dependance of the spinor in the direction of

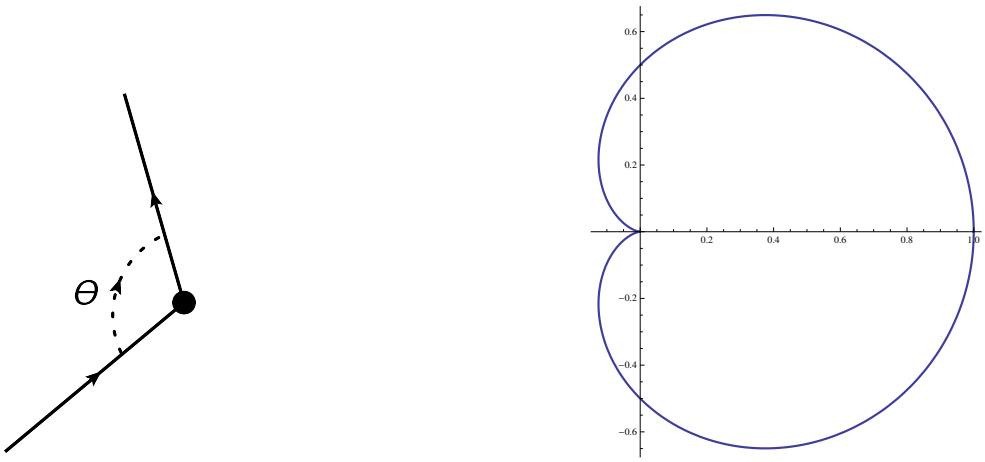

Figure 5.4: Polar plot of the spinor overlap $g(\vec{k},\vec{k'})$ (proportional to the scattering probability) as a function of the relative angle θ between incoming and outgoing wave vector given by Eq. (5.9).

the wavevector. In this case we obtain a scattering probability proportional to the spinor overlap :

$$g(\vec{k},\vec{k'}) = |_s\langle\vec{k'}|\vec{k}\rangle_s|^2 = \frac{1}{2}\left(1+\cos(\theta-\theta')\right) \ , \tag{5.9}$$

where θ and θ' are the polar angle corresponding to the direction of the wave vectors $\vec{k}$ and $\vec{k'}$ on the Fermi surface. We can see in Fig. 5.4 that the scattering is anisotropic, but there is no dependance in the direction of the wavevectors, only a dependance in the relative angle of the scattering.

During the integration over all the available wave-vectors, the cosine term averages out, and we obtain 1/2, whereas in the case of non relativistic electrons, the overlap $g(\vec{k},\vec{k'})$ is constant and equal to 1.

We also notice in Fig. 5.4 the absence of backscattering as the probability $g(\vec{k},-\vec{k})$ vanishes. This comes from the combination of the spin 1/2 nature of the Hamiltonian and its time-reversal symmetry : if an eigenstate goes at $\vec{k}$ with a spin $\vec{\sigma}$, the eigenstate going at $-\vec{k}$ has a spin $-\vec{\sigma}$. However, the scalar nature of the potential preserves the time-reversal symmetry and thus does not allow spin flips, ensuring the absence of backscattering as opposed to magnetic impurities.

5.2.3 Classical conductivity

The conductivity is derived by solving the integro-differential Boltzmann equation, which gives the effect of an electric field $\vec{E}$ on the local density of state

at a given wavevector $f(\vec{k})$:

$$-e\vec{E}.\frac{\partial f}{\partial \vec{k}} = \langle \int \frac{d\vec{k'}}{(2\pi)^2} \quad 2\pi |\langle \vec{k'}|V|\vec{k}\rangle|^2 \delta(E(\vec{k'}) - E_F) \left[f(\vec{k'}) - f(\vec{k}) \right] \rangle \ . \quad (5.10)$$

To solve it, we assume that the local density of states $f(\vec{k})$ responds linearly to the electric field, and look to the first order terms in the electric field. We use the ansatz $f(\vec{k}) = n_F(E(\vec{k})) + \frac{\partial n_F}{\partial E}\bar{f}(\theta)$ where θ accounts for the direction of the wavevector $\vec{k}$. Using the value of the spinor overlap $|\langle \theta'|\theta\rangle|^2 = (1+\cos(\theta'-\theta))/2$ we solve the equation in $\bar{f}$ assuming the electric field is along the x-axis and find :

$$\bar{f}(\theta) = 2ev_F\tau_e \cos\theta E_x \ . \quad (5.11)$$

We can derive the electric current along the x-axis caused by the electric field $j_x = \int \frac{d\vec{k}}{(2\pi)^2} e\frac{1}{\hbar}\frac{dE}{dk_x}\bar{f}(\theta)\delta(E(\vec{k}) - E_F)$ and dividing by the electric field we find the classical Drude conductivity :

$$\sigma_{xx} = e^2 v_F^2 \tau_e \rho(E_F) \ . \quad (5.12)$$

Using the Einstein equation $\sigma = e^2\rho D$, it is possible to determine the diffusion constant $D = v_F^2\tau_e$ and the corresponding transport time τ_{tr} defined as $D = \frac{v_F^2\tau_{tr}}{d}$ where d is the dimensionality of the problem, here $d = 2$. In this case, there is a doubling of the transport time compared to the elastic scattering time due to the anisotropy of the scattering : we have seen that the probability for a given state to be scattered into another direction is not the same in every direction, even if the disorder is isotropic. Starting from a given direction $\vec{k}$, after a single scattering event, the probability of going in the direction $\vec{k'} = -\vec{k}$ is strongly reduced. After two scattering events, this probability is proportional to the convolution of two $g(\vec{k}, \vec{k'})$:

$$g^{(2)}(\vec{k}, \vec{k'}) = \int_0^{2\pi} \frac{dt}{\pi} \frac{1+\cos(t-\theta)}{2} \frac{1+\cos(\theta'-t)}{2} \ . \quad (5.13)$$

The normalization factor in the integral of π comes from the normalization of the scattering probability as $\int_{\vec{k'}} g(\vec{k}, \vec{k'}) = \pi$.

We can check on the plot of Fig. 5.5, that the scattering probability becomes of the same order of magnitude for every direction after two scattering events, so we can consider we have lost memory of the initial direction of propagation and we have entered a diffusive regime.

5.3 Standard diagrammatic technique

In the precedent section, we have seen that we can derive the value of the classical conductivity from the Hamiltonian of the problem. However, solving the Boltzmann equation does not provide any information about the corrections

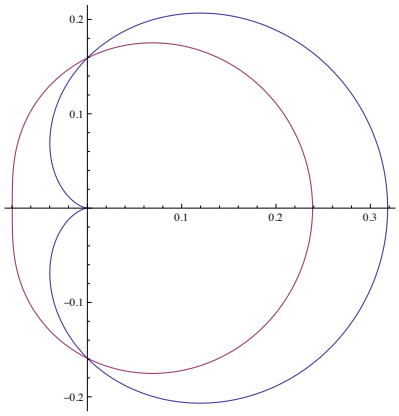

Figure 5.5: Polar plots of the single scattering spinor overlap $g(\vec{k},\vec{k'})$ (blue) and double scattering spinor overlap $g^{(2)}(\vec{k},\vec{k'})$ (red) as a function of the relative angle θ between incoming and outgoing wave vector given by Eq. (5.9) and Eq. (5.13).

coming from the quantum nature of the excitations : the interferences responsible for the quantum correction to conductivity or the universal conductance fluctuations are not taken into account.

In a conductance measurement experiment, we measure the current flowing through a material as a function of the voltage bias applied. Because of the disorder, there is a large number of paths that the electron can travel from one end to another, each with a given complex amplitude a_i. The total amplitude is thus $\sum_i a_i$, but the probability from going from one end to the other is given by the modulus square of the amplitude : $P = \sum_{i,j} a_i a_j^*$. A different way to see this equation is that the current is created by particle-hole excitations, and that we need to consider all the different paths followed by the particle and the hole. In classical mechanics, we would just have the simple sum $P_{class} = \sum_i a_i a_i^*$, but this simpler expression does not take into account the quantum interferences.

The indices for the sum run over a infinite number of different paths, each with a different weight given by the amplitude probability. We use the standard diagrammatic technique as in [32] in order to simplify this infinite sum and consider only the most significant terms. This diagrammatic technique is relevant only in the regime of weak disorder since it corresponds to a perturbative approach, where the perturbative parameter is the strength of the disorder.

5.3.1 Kubo formula

The starting point of our study will be the Kubo formula giving the conductivity tensor of a sample, as a function of the microscopic parameters of the

Hamiltonian :

$$\sigma_{\alpha\beta} = \frac{\hbar}{2\pi\Omega} \Re Tr \left(j_\alpha G^R j_\beta G^A \right) \ . \tag{5.14}$$

In this equation, Ω is the volume of the sample, j_α is the current operator along the direction α, and $G^{R/A}$ represent respectively the propagation of the electron (resp. hole) like excitation in the sample. This equation is derived from a linear response of the sample to a potential vector, assuming that the Fermi energy is much larger than the temperature, and that the study is done in the weak disorder regime $k_F l_e \gg 1$. For the interested reader, a derivation of this Kubo formula can be found in [32].

For a given realization of the disorder, this Kubo formula gives the corresponding value of the conductivity. Consequently, the conductance is a function of the realization of the disorder, and becomes a random variable of the disorder. The relevant physical quantity is thus the probability distribution of this random variable that we characterize by its first and second cumulant.

Moreover, this description allows to understand the transition from the mesoscopic to the classical regime : if we divide a sample of length L in N samples of size L_ϕ where the interference effects are visible $N = (L/L_\phi)^d$, the variance of the conductivity scales as $\frac{\sqrt{\langle (G - \langle G \rangle)^2 \rangle}}{\langle G \rangle} = \frac{1}{\sqrt{N}} = (L_\phi/L)^{d/2}$. For a large sample, this variance vanishes, and the conductivity is equal to its mean-value, this property is called self-averaging, and justifies the classical regime of Ohm's law.

Noting $\langle ... \rangle$ the average over many realizations of the disorder we first focus on $\langle \sigma \rangle$, and since this quantity is the mean-value of a product, we first calculate the product of the mean-values which we call the *bare* conductivity, then add the remaining part, the contribution of the *diffuson*.

5.4 Calculation of the Green's functions

5.4.1 Ballistic Green's function

The Green's functions are a very general tool used in physics to solve a linear problem $\mathcal{L}X = F$ where $\mathcal{L}$ is a linear operation, X the unknown variable and F a known variable. If X_1 and X_2 are solution of $\mathcal{L}X = F_i$, then $X_1 + X_2$ is a solution of $\mathcal{L}X = F_1 + F_2$. When dealing with variables that are functions of a variable, it is convenient to express the function F as an integral of Dirac functions, and look for the solution as the integral of all the solution of the problem when F is a Dirac function.

In quantum mechanics, the eigenvalue problems we want to solve is the following $\mathcal{H}X = EX$, so we look for the Green's functions of the problem as solutions of $(E - \mathcal{H})G(\vec{r}, \vec{r'}) = \delta(\vec{r} - \vec{r'})$. However, in our problem, we do not know precisely $V(\vec{r})$ for a given realization of the disorder, so we will first focus on the ballistic Green's function by focusing only on the kinetic Hamiltonian.

Moreover, the spatial invariance of the problem assures that $G(\vec{r},\vec{r'}) = G(\vec{r}-\vec{r'})$. Finally, the kinetic Hamiltonian is diagonal in $\vec{k}$-representation, so it will be easier to do a spatial Fourier transform and express G in this representation :

$$(E - \hbar v_F \vec{k}.\vec{\sigma}) G^0(\vec{k}) = Id \; . \tag{5.15}$$

Using the algebra of the Pauli matrices, it is easy to derive the solution :

$$G^0(\vec{k}) = (E - \hbar v_F \vec{k}.\vec{\sigma})^{-1} = \frac{E + \hbar v_F \vec{k}.\vec{\sigma}}{E^2 - \hbar^2 v_F^2 k^2} \; . \tag{5.16}$$

We can refine this Green's function by taking into account the finite lifetime of the particles, introducing an imaginary part to the energy $E \to E \pm i\eta$. In the regime of weak disorder, this imaginary part is small compared to the Fermi energy $\eta \ll E$. The $\pm$ sign in front of this finite lifetime for the Green's function depends on whether we consider the electron-like excitation propagation (plus sign) or the hole-like (minus sign).

5.4.2 Disorder averaged Green's function

The ballistic Green's function obeys the equation $(E - \mathcal{H}_0)G^0 = Id$, similarly, the Green's function in presence of disorder should obey the equation $(E - \mathcal{H})G = Id$, so to calculate it explicitly, we consider the disorder as a perturbative parameter, with the series expansion :

$$(E - \mathcal{H}_0 - V)G = Id = \left((G^0)^{-1} - V\right) G \; , \tag{5.17}$$

$$(G^0)^{-1} G = Id + VG \; . \tag{5.18}$$

This equation $G = G^0 + G^0 V G^0 + G^0 V G^0 V G^0 + ...$, is easier to understand in the real space. Expressed in this representation, the Green's function $G(\vec{r}-\vec{r'})$ should be understood as a propagation from $\vec{r'}$ to $\vec{r}$ and the series expansion equation is written :

$$G(\vec{r}-\vec{r'}) = G(\vec{r}-\vec{r'}) + \int_{\vec{r_1}} G(\vec{r_1}-\vec{r'}) V(\vec{r_1}) G(\vec{r}-\vec{r_1}) + ... \tag{5.19}$$

This means that in presence of disorder, traveling from $\vec{r'}$ to $\vec{r}$ can be done directly, encountering no scatterer, or encountering scatterers any number of time.

To calculate the mean-value of this Green function, we use the properties of the gaussian disorder introduced earlier : $\langle V(\vec{R})\rangle = 0$, $\langle V(\vec{r})V(\vec{r'})\rangle = \gamma\delta(\vec{r}-\vec{r'})$ and the other cumulants vanish. In the series expansion $G = G^0 + G^0 V G^0 + G^0 V G^0 V G^0 + ...$, we apply the Wick's theorem which allows us to express the mean value for the product of V as a sum of disorder correlators. Because only the second cumulant does not vanish, we only keep in the sum the terms

Figure 5.6: Diagrammatic representation of the equation for the Green's function. The double line represents the naked Green function, and the doted line an interaction with the disorder. Left : all the terms contributing to the Green's function. Right : the terms that do not contribute to the disorder averaged Green's function have been removed.

where the potential appears an even number of times. In the reciprocal space of the k-representation, we have :

$$\langle G(\vec{k})\rangle = G^0(\vec{k}) + \left\langle \int_{\vec{q},\vec{q'}} G^0(\vec{k})V(\vec{q})G^0(\vec{k}-\vec{q})V(\vec{q'})G^0(\vec{k}-\vec{q}+\vec{q'}) \right\rangle + ... \quad (5.20)$$

We will now on use the notation $\int_{\vec{k}} = \int \frac{d\vec{k}}{(2\pi)^2}$ to simplify the equations. All the diagrams accounting for this expression of G (cf. right picture of Fig. 5.6) can be separated in two groups, depending on how the impurity lines connect to the Green's functions. If it is possible to separate the diagram in two diagrams that are not connected *via* an impurity line (for example the last diagram in the right picture of Fig. 5.6), the diagram is called reducible, else it is called irreducible. This means that every reducible diagram can be seen as a product of irreducible diagrams connected by ballistic Green's function. Noting Σ the sum of all the irreducible diagrams also called *self-energy*, we express the Eq. (5.20) as a recursive equation :

$$\langle G(\vec{k})\rangle = G^0(\vec{k}) + G^0(\vec{k}) \sum_{n=1}^{\infty} \left[\Sigma(\vec{k})G^0(\vec{k})\right]^n = G^0(\vec{k}) + G^0(\vec{k})\Sigma(\vec{k})\langle G(\vec{k})\rangle \ . \quad (5.21)$$

Using the value of the ballistic Green's function, we solve this Dyson equation and find :

$$\langle G(\vec{k})\rangle = \frac{(E-\Sigma(\vec{k}))Id + \hbar v_F \vec{k}.\vec{\sigma}}{(E-\Sigma(\vec{k}))^2 - \hbar^2 v_F^2 k^2} \ . \quad (5.22)$$

5.4.2.1 Self-energy

The calculation of the self-energy requires the calculation of the sum of an infinity of terms (all the irreducible diagrams). However, in the regime of weak disorder, the disorder is treated as a perturbation, so we have a natural perturbative parameter as the strength of the disorder compared to the Fermi energy $\sqrt{\gamma}/E$ or more conveniently $1/(k_F l_e)$, and this sum is dominated by

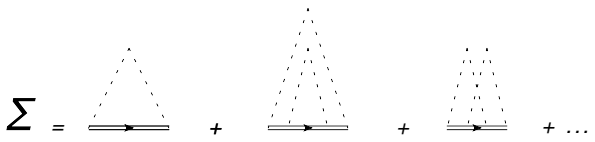

Figure 5.7: Diagrammatic representation of the self-energy.

the first term, with a single pair of scattering events, the others terms being subdominant. This first term is :

$$\Sigma_1(\vec{k}) = \int_{\vec{q}} \langle V(\vec{q})V(-\vec{q})\rangle G^0(\vec{k}-\vec{q}) \ . \tag{5.23}$$

The calculation of this first term of the self energy shows that it is a complex number. The real part does not have a physical meaning, it can be reabsorbed by a proper definition of the energy that is not relevant for the physics studied. The imaginary part of the energy has a physical meaning, it corresponds to a finite lifetime for the ballistic states, and is also denoted as the elastic scattering time :

$$Im\ \Sigma_1 = \frac{-\hbar}{2\tau_e} = \frac{-\pi\rho(E_F)\gamma}{2} \ . \tag{5.24}$$

However, to calculate this self energy, we made the assumption that the finite lifetime for the ballistic Green's function as seen in Sec. 5.4.1, for example originating from the inelastic scattering, enters in the energy E_F through a small positive imaginary part $E_F \to E_F + i\eta$. This corresponds to particle-like excitations, but for the holes, this is not correct and we should take $E_F - i\eta$. In the end, we obtain two different Green's functions averaged over the disorder, one for the particle like excitation, called the retarded Green's function G^R, and one for the hole-like, called the advanced Green's functions G^A :

$$\langle G^{R/A}(\vec{k},E)\rangle = \frac{E^{R/A}Id + \hbar v_F \vec{k}.\vec{\sigma}}{(E^{R/A})^2 - \hbar^2 v_F^2 k^2} \qquad \text{where} \qquad E^{R/A} = E \pm i\left(\eta + \frac{\hbar}{2\tau_e}\right) \ . \tag{5.25}$$

This addition rule for the inverse of finite life times is known as the Matthiessen rule, and allows to take into account other scattering mechanisms (magnetic impurities for example). Here, we only consider a scalar disorder as a source of scattering, and we are in the mesoscopic physics regime where τ_e is much smaller than the lifetime, so we assume $E^{R/A} = E \pm i\frac{\hbar}{2\tau_e}$.

5.5 Diffuson

To calculate the mean-value of the conductivity, the first step is to use the approximation $\langle G^R G^A\rangle = \langle G^R\rangle\langle G^A\rangle + ...$ This means that during the propagation, we have only consider the propagations of the electron and the hole with

Figure 5.8: Example of contributions coming from the coupling of the two Green's functions through the disorder. Left : example of contribution that average out. Right : one of all the terms we need to consider to obtain the diffuson.

independent scattering events. For example, terms as $\langle G^0 V(\vec{q}) G^0 G^0 V(-\vec{q}) G^0 \rangle$ that are present in the conductivity are not taken into account in this approximation and are hidden in the dots.

In these terms, the retarded and advanced Green's functions have to exchange momentum at each scattering event, because the potential is uncorrelated $\langle V(\vec{r}) V(\vec{r'}) \rangle = \gamma \delta(\vec{r} - \vec{r'})$, this is why each scatterer has to be seen the same number of time by each Green's function. Moreover, during the propagation, the retarded (resp. advanced) Green's function acquire a phase of order $k_F l_r$ (resp. $k_F l_a$) where l_r (resp. l_a) is the length of the path followed by the electron (resp. hole) like excitation. If the two paths differ, the difference of length should be at least of order l_e, which is an order of value of the length between two scattering events, then the difference of phase will be of order $k_F l_e \gg 1$, meaning that these contributions vanish when we average over different realizations of the disorder. In the end, we have to consider only the contributions where the two excitations encounter the same sequence of scatterers where they exchange momentum.

We will introduce the *diffuson* noted Γ^D as the sum of all the terms of this kind, as we are interested in terms $\langle G^R(\vec{k}) \rangle \langle G^A(\vec{k} - \vec{q}) \rangle \Gamma^D(\vec{q}) \langle G^R(\vec{k'}) \rangle \langle G^A(\vec{k'} - \vec{q}) \rangle$. We can write a recursive equation on Γ^D :

$$\Gamma^D(\vec{q}, \omega) = \gamma Id \otimes Id + \int_{\vec{k}} \gamma \langle G^A(\vec{k} - \vec{q}, E_F - \omega) \rangle \otimes \langle G^R(\vec{k}, E_F) \rangle \Gamma^D(\vec{q}, \omega) \ . \quad (5.26)$$

This just means that we are building recursively all the terms by adding all the scatterers one after the other, the integration over the momentum ensuring that we count every amount of momentum exchanged in the scattering. The tensorial product $\otimes$ is a notation to remind that we are considering the propagation of two spin 1/2 particles. By inverting this relation we obtain the formal relation $\Gamma^D = \gamma (Id \otimes Id - \gamma P^D)^{-1}$.

5.5.1 $P^D(\vec{q},\omega)$

This quantity of crucial interest in the calculation of the diffuson term is defined by the relation :

$$P^D(\vec{q},\omega) = \int \frac{d\vec{k}}{(2\pi)^2} \langle G^R(\vec{k},E_F)\rangle \langle G^A(\vec{k}-\vec{q},E_F-\omega)\rangle \ . \tag{5.27}$$

To calculate it, we use the expression for the mean-values of the Green's functions derived in Eq. (5.25) $\langle G^{R/A}(\vec{k},E)\rangle = \frac{E^{R/A}+\hbar v_F \vec{k}.\vec{\sigma}}{(E^{R/A})^2-\hbar^2 v_F^2 k^2}$ where $E^{R/A} = E \pm i\hbar/\tau_e$. We focus on the conductance at zero frequency, so we consider $\omega = 0$ and the calculations are done in the following manner :

- we drop the dependance in $\vec{q}$ and $\hbar/\tau_e$ in the upper part of the fraction, since they are dominated by $\vec{k}$ and E_F :

$$P^D(\vec{q},\omega=0) = \int \frac{d\vec{k}}{(2\pi)^2} \frac{E+\hbar v_F \vec{k}.\vec{\sigma}}{(E^R)^2-\hbar^2 v_F^2 k^2} \frac{E+\hbar v_F \vec{k}.\vec{\sigma}}{(E^A)^2-\hbar^2 v_F^2 (k-q)^2} \ , \tag{5.28}$$

- then we perform a polar transformation, and integrates the radial part *via* the residue theorem,

$$\begin{aligned} P^D(\vec{q},\omega=0) = \int \frac{dk}{2\pi}\frac{d\theta}{2\pi} & \frac{E+\hbar v_F k(\cos\theta\sigma^x+\sin\theta\sigma^y)}{(E^R)^2-\hbar^2 v_F^2 k^2} \\ & \frac{E+\hbar v_F k(\cos\theta\sigma^x+\sin\theta\sigma^y)}{(E^A)^2-\hbar^2 v_F^2 (k^2+q^2-2k\cos\theta q_x+\sin\theta q_y)} \end{aligned} \tag{5.29}$$

$$\begin{aligned} = \int \frac{d\theta}{2\pi} & (Id+(\cos\theta\sigma^x+\sin\theta\sigma^y))^2 \times \frac{2i\pi}{-2E} \\ & \frac{E}{(E^A)^2-(E^R)^2+2E\hbar v_F(\cos\theta q_x+\sin\theta q_y)-\hbar^2 v_F^2 q^2} \ , \end{aligned} \tag{5.30}$$

- after a series expansion in $\tau_e v_F \vec{q}$, the integration of the angular part is obvious and we find that :

$$\begin{aligned} P^D(\vec{q},\omega=0) = \frac{1}{2\gamma} \Bigg[& \left(1-\frac{\tau_e^2 v_F^2 q^2}{2}\right) Id\otimes Id + \frac{1}{2}\left(1-\frac{\tau_e^2 v_F^2 q^2}{4}\right)\vec{\sigma}\otimes\vec{\sigma} \\ & -iv_F\tau_e\frac{1}{2}\ \vec{q}.(\vec{\sigma}\otimes Id + Id\otimes\vec{\sigma}) - \frac{\tau_e^2 v_F^2}{4}(\vec{\sigma}.\vec{q})\otimes(\vec{\sigma}.\vec{q})\Bigg] + o(\tau_e^2 v_F^2 q^2). \end{aligned} \tag{5.31}$$

We can now plot easily the spectrum of $Id\otimes Id - \gamma P^D$ as a function of $q = \|\vec{q}\|$ and find (Fig. 5.9) that at long distance (meaning small q), there is

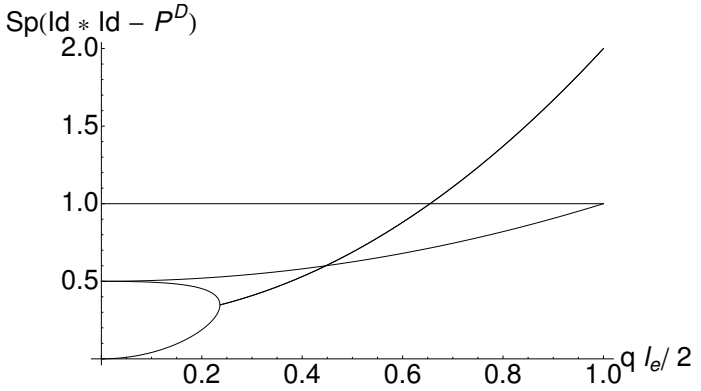

Figure 5.9: Spectrum of $Id \otimes Id - \gamma P^D(\vec{q}, \omega = 0)$ as a function of $q = \|\vec{q}\|$.

only one mode whose eigenvalue vanishes. This mode is thus the only massless diffusive mode and is the singlet one, whereas the other triplet mode are massive (their eigenvalues are non zero). These names of singlet and triplet correspond to the fact that we are considering the propagation of two spin $1/2$ excitations, G^R and G^A, so the natural basis is composed of a singlet state and three triplet. However, this denomination must be considered carefully, indeed, the spin is not a correct quantum number because of the spin-momentum locking, at different momenta, the natural basis of the spin changes. The singlet/triplet is then correct only in the diffusive limit $q = 0$; but we extend it when $q \neq 0$, even if the terms in the second line of the equation Eq. (5.31) induce a departure of the eigenstates from traditional singlet and triplet states.

As we will see in the section 6.4, we expect the presence of a single diffusive mode instead of the four that could be present. This reduction of the number of diffusive mode is due to the symmetries of the problem, in this case, because of the spin $1/2$ nature of the surface states, the time-reversal operation Θ squares to the opposite of the identity $\Theta^2 = -Id$. This corresponds to a given universality class in the Anderson problem (either unitary or symplectic, in this case symplectic) where the number of diffusive mode is fixed to 1.

To describe the diffusion at long distance, it is thus necessary to keep only the singlet mode so we approximate the diffuson structure factor by its limit $\vec{q} \to 0$:

$$\Gamma^D(\vec{q}) = \gamma \frac{1}{Dq^2\tau_e} \frac{1}{4} \left[Id \otimes Id + \sigma^x \otimes \sigma^x - \sigma^y \otimes \sigma^y + \sigma^z \otimes \sigma^z \right] . \tag{5.32}$$

We can notice that except the spinorial nature of this diffuson expressed between the brackets, we observe the same expression for the diffuson structure factor as in the case of non relativistic electrons in $\frac{1}{Dq^2\tau_e}$, as expected since the diffuson should obey a diffusion equation. However, the importance of the diffuson in the diffusion process does not come only from this diffusive mode, but

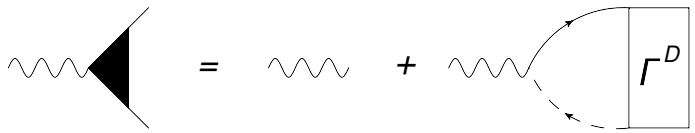

Figure 5.10: Diagrammatic representation of the current operator renormalization.

also from a renormalization of the current operator, and this renormalization is due to one of the massive modes.

5.5.2 Renormalization of the current operator

By definition, the current operator is obtained by introducing electric potential *via* the substitution $\vec{p} \to \vec{p} - e\vec{A}$, and deriving the Hamiltonian with respect to the potential, $j_\alpha = \frac{\delta \mathcal{H}}{\delta A_\alpha}$. In the case of Dirac fermions we obtain that the current operator is given by the density of spin, $j_\alpha = -ev_F\sigma^\alpha$.

The renormalization of the current operator is obtained by including a vertex correction, in the form of an additionnal diffuson to the current operator, $J_\alpha = j_\alpha + j_\alpha P^D \Gamma^D$ as represented in the diagram of the figure 5.10. We can check that it is equivalent to :

$$J_\alpha = j_\alpha \otimes \frac{1}{\gamma}\Gamma^D \ . \tag{5.33}$$

In this case, the diffusive mode will have no contribution, even at $q = 0$ because of the sum on the Pauli matrices. However, the triplet modes of the diffuson structure factor Γ^D do contribute and we obtain a renormalized current operator $J_\alpha = 2j_\alpha$.

We observe the apparition of the same factor of two, seen in the Sec.5.2.3, due to the anisotropy of the scattering. It corresponds to the difference between the elastic scattering time and the transport time corresponding to diffusive transport. Because of the anisotropy of the scattering, we need to observe two scattering events to lose memory of the initial wavevector (cf. Fig. 5.5).

5.5.3 Classical conductivity

To calculate the mean-value of the classical conductivity, or Drude conductivity, we need to add all the diagrams where the particle-like excitation and the hole-like excitation exchange momentum during scattering events. In addition to the simple diagram where they do not exchange momentum, we need to count all the "ladder" diagrams where they follow the same scattering sequence, which is the diffuson (Fig.5.11). In the end, this calculation is similar to the plugging of a current operator to the renormalized current operator.

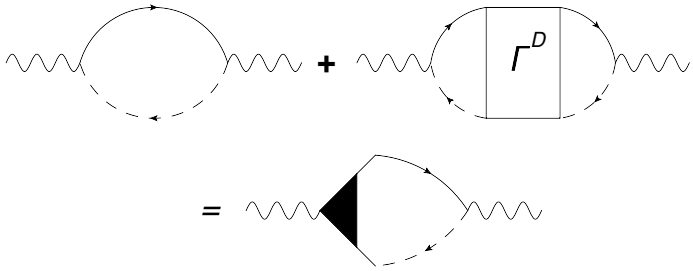

Figure 5.11: Diagrammatic representation of the calculation of the classical conductivity.

Namely we will have the equation :

$$\langle \sigma^{Dr}_{\alpha\beta} \rangle = \langle \frac{\hbar}{2\pi\Omega} \Re Tr \left(j_\alpha G^R j_\beta G^A \right) \rangle \tag{5.34}$$

$$= \frac{\hbar}{2\pi} tr \left(J_\alpha P^D(\vec{q}=0) j_\beta \right) \ . \tag{5.35}$$

In this equation, Tr means a trace over all quantum numbers (momenta and spins), whereas tr is a trace only on the spins, the integration over the momenta being calculated in P^D. Using the relation between the elastic scattering time and the strength of the disorder $\hbar/\tau_e = \pi\rho(E_F)\gamma$, we can express the conductivity tensor as a function of the scattering time and finds for the longitudinal conductivity the same result as Eq. (5.12) :

$$\langle \sigma^{Dr}_{\alpha\beta} \rangle = \frac{\hbar}{2\pi} e^2 v_F^2 2 \frac{\delta_{\alpha\beta}}{\gamma} = e^2 \rho(E_F) v_F^2 \tau_e \delta_{\alpha\beta} \ . \tag{5.36}$$

In agreement with what has been done in the Sec.5.2.3, this gives a diffusion constant $D = v_F^2 \tau_e$, hence a transport time twice larger than the elastic scattering time.

Good good good good vibrations

The Beach Boys

Chapter 6

Quantum correction to the conductivity and universal conductance fluctuations

So far, we have considered only classical transport, in the sense that the interference effects coming from the wave nature of the excitations have not been taken into account. The Boltzmann equation and the diagrammatic calculations at the level of approximation considered previously, even if they have been treated within quantum mechanics framework (Fermi golden rule or Green's functions) do not explain the weak-anti localization behavior seen experimentally.

In these experiments, the resistivity of a sample (graphene or the surface of a 3d topological insulator) is measured as a function of a transverse magnetic field. What is observed in this case is a decrease of the resistivity (or an increase of the conductivity) when the magnetic field vanishes, with a characteristic magnetic field corresponding to a quantum of flux through the whole surface of the sample. Since this field is very small, the reason for this change in the resistivity can not be explained classically ; this does not come from a curving of the trajectories of the particles by the magnetic field. In fact, the surface states we study are not charge neutral, and in presence of a magnetic field, they acquire a phase : we need to refine our diagrammatic approach to take into account the quantum interferences originating from this additional phase, responsible of this dip in resistivity at zero field.

6.1 The cooperon

The terms responsible for this effect are called *cooperon* and their origin lies in the fact that in our approximation for the diffuson, when we neglected all the diagrams where the electron and hole do not encounter the same scatterers in the same order, we neglected crossed diagrams that do not average out.

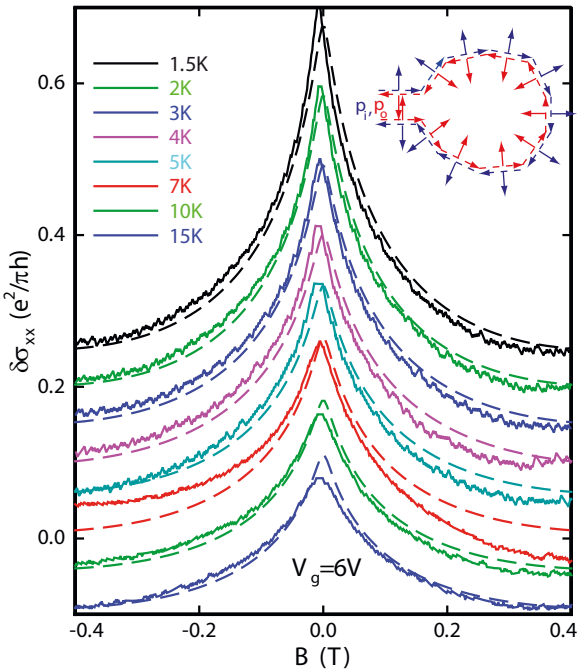

Figure 6.1: Experimental measurement of the weak anti-localization correction on the topological insulator strained HgTe [16].

Indeed, if a diffuson forms a loop, it is possible to reverse the path of one of the branches as long as the time-reversal symmetry is preserved. In this case, the argument on the difference of the length of the two paths drops and no phase is accumulated so these diagrams do contribute to the conductivity. In our study, the time reversal symmetry is preserved since a time reversal operation consists in changing signs for both the momenta and the spins. However, the introduction of a transverse magnetic field will break it, and in absence of time-reversal symmetry it becomes impossible to reverse one of the branch of the diffuson. The contribution of the cooperon then vanishes, explaining the change in the resistivity seen experimentally.

More precisely, we need to calculate diagrams of the form depicted in Fig. 6.3. A different representation of the cooperon shows that its structure is very similar to the diffuson's, as expected since it is a diffuson with one of the branch time-reversed.

The equation for the cooperon's structure factor reads :

$$\Gamma^C(\vec{Q}) = \gamma Id \otimes Id + \int_k \gamma \langle G^A(\vec{Q}-\vec{k})\rangle \otimes \langle G^R(\vec{k})\rangle \Gamma^C(\vec{Q}) \,, \qquad (6.1)$$

which can be written as $\Gamma^C = (Id \otimes Id - \gamma P^C(\vec{Q})^{-1})$ with the appropriate P^C, and Γ^C is then solved similarly than for Γ^D.

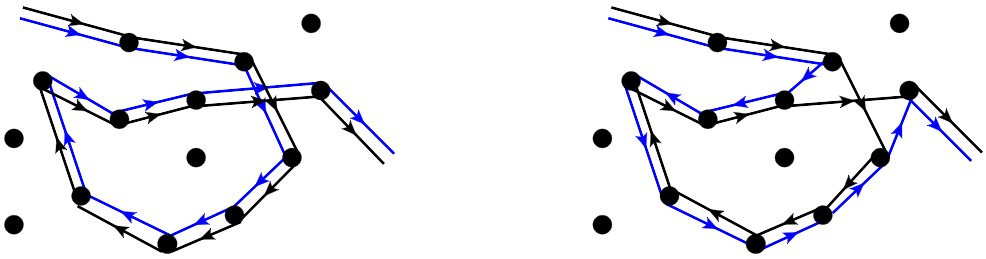

Figure 6.2: Representation in real space of a diffuson (left) forming a loop with the corresponding cooperon (right).

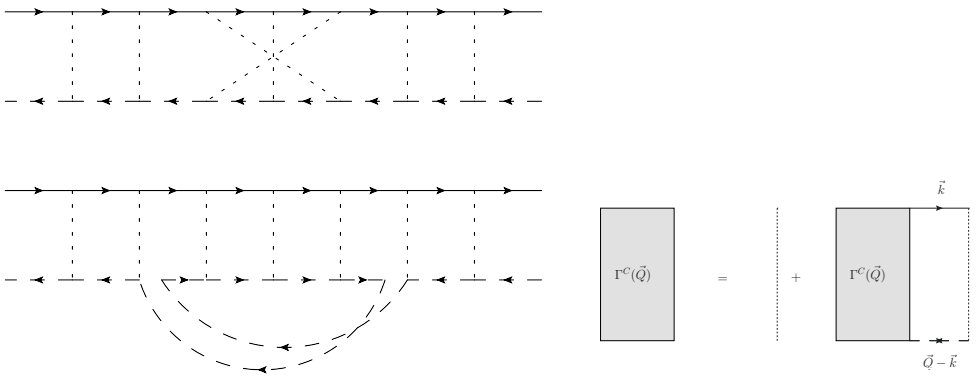

Figure 6.3: Left : Diagrammatic representation of the cooperon structure factor in the middle part, stressing it similarity with the diffusons at each end. Right : Recursive equation obeyed by the cooperon structure factor

Furthermore, we can use adequately additional symmetries coming from the reversal of, for example, the momentum and the spin on the hole like excitation. In the calculation of P^C, we can write the advanced Green's function around $-\vec{k}$ as a Green's function around $\vec{k}$ by absorbing the minus sign in a new definition of the $\vec{\sigma}$ matrix :

$$\langle G^A(\vec{Q}-\vec{k})\rangle = \frac{E+\hbar v_F(\vec{Q}-\vec{k}).\vec{\sigma}}{(E^A)^2-\hbar^2 v_F^2(Q-k)^2} = \frac{E+\hbar v_F(\vec{k}-\vec{Q}).\tilde{\sigma}}{(E^A)^2-\hbar^2 v_F^2(k-Q)^2}\ . \qquad (6.2)$$

In this expression we have $\tilde{\sigma}=-\vec{\sigma}$, and the calculation of $P^C=\int_{\vec{k}}\langle G^A(\vec{Q}-\vec{(}k))\rangle\langle G^R(\vec{k})\rangle$ is the same than the calculation of P^D in Sec. 5.5 and similarly to Eq. 5.31 we obtain :

$$P^C(\vec{q},\omega=0)=\frac{1}{2\gamma}\left[\left(1-\frac{\tau_e^2 v_F^2 q^2}{2}\right)Id\otimes Id-\frac{1}{2}\left(1-\frac{\tau_e^2 v_F^2 q^2}{4}\right)\vec{\sigma}\otimes\vec{\sigma}\right.$$
$$\left.-iv_F\tau_e\frac{1}{2}\ \vec{q}.(\vec{\sigma}\otimes Id-Id\otimes\vec{\sigma})+\frac{\tau_e^2 v_F^2}{4}(\vec{\sigma}.\vec{q})\otimes(\vec{\sigma}.\vec{q})\right]+o(\tau_e^2 v_F^2 q^2). \qquad (6.3)$$

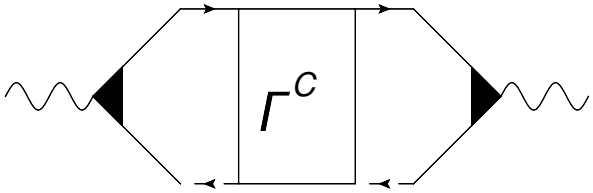

Figure 6.4: Diagrammatic representation of the calculation of the quantum correction to conductivity.

The calculation of the cooperon structure factor Γ^C is slightly more subtle because we need to take into account the direction of propagation of the Green's function in the recursive equation. Since it must be done "backwards", this correspond to take the transpose of the matrices. The composition of the minus sign from $\tilde{\sigma}$ and the transpose corresponds to add a minus sign to σ^x and σ^z matrix of the advanced Green's function branch, but the minus sign does not affect the σ^y matrix since $-(\sigma^y)^T = \sigma^y$. In the end, from Eq. (5.32), the cooperon structure factor can be approximated when $Q \longrightarrow 0$:

$$\Gamma^C(\vec{Q}) = \gamma \frac{1}{DQ^2\tau_e} \frac{1}{4} \left[Id \otimes Id - \sigma^x \otimes \sigma^x - \sigma^y \otimes \sigma^y - \sigma^z \otimes \sigma^z \right] . \qquad (6.4)$$

Again, we observe that except for the spinorial nature of the cooperon structure factor, it presents the same dependance in Q as in the non relativistic case $\frac{1}{DQ^2\tau_e}$, since it obeys a diffusion equation.

We also observe that the cooperon structure is a traditional singlet $\Gamma^C \propto [Id \otimes Id - \sigma^x \otimes \sigma^x - \sigma^y \otimes \sigma^y - \sigma^z \otimes \sigma^z]$ as opposed to the diffuson structure factor $\Gamma^D \propto [Id \otimes Id + \sigma^x \otimes \sigma^x - \sigma^y \otimes \sigma^y + \sigma^z \otimes \sigma^z]$. Indeed, the diffuson structure is associated with the diffusion of a particle-like excitation and a hole-like excitation ; the cooperon is associated with the diffusion of two excitations of the same nature, allowing for a traditional expression of the singlet.

6.2 Quantum correction to conductivity

The quantum correction to conductivity (or weak anti-localization) $\langle \Delta\sigma \rangle = \langle \sigma \rangle - \langle \sigma^{Dr} \rangle$ originating from the cooperon contribution is obtained similarly to the diffuson correction by calculating (cf Fig.6.4) :

$$\langle \Delta\sigma_{\alpha\beta} \rangle = \frac{\hbar}{2\pi} Tr \left[G^A(\vec{k}) J_\alpha G^R(\vec{k}) \Gamma^C(\vec{Q} = \vec{k} + \vec{k'}) G^R(\vec{k'}) J_\beta G^A(\vec{k'}) \right] . \qquad (6.5)$$

The Tr part is an integration over the momenta $\vec{k}$ and $\vec{k'}$ or similarly the momenta $\vec{k}$ and $\vec{Q}$ as long as the condition $\vec{Q} = \vec{k} + \vec{k'}$ is preserved. The expression for Γ^C shows that the dominant part of the integration comes from

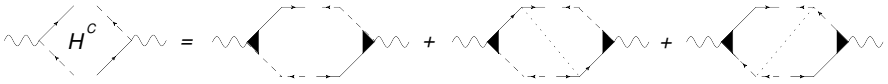

Figure 6.5: Diagrammatic representation of the three Hikami boxes.

for small Q. As the Green's functions are regular around $\vec{k}$, we drop their dependance in $\vec{Q}$. It is then possible to write this correction to conductivity as follows :

$$\langle \Delta\sigma_{\alpha\beta} \rangle = \frac{\hbar}{2\pi} tr \left[\int_{\vec{Q}} \Gamma^C(\vec{Q}) H_0 \right] , \tag{6.6}$$

where we have noted $H_0 = \int_{\vec{k}} G^A(\vec{k}) J_\alpha G^R(\vec{k}) \otimes G^R(-\vec{k}) J_\beta G^A(-\vec{k})$ the first *Hikami box* (cf Fig. 6.5).

6.2.1 Calculation of the Hikami box

The calculation of this first Hikami box is done in the same way as was done the calculation of P^D, without the difficulty of searching for a series expansion in $\vec{q}$. From now on we focus only on the longitudinal terms of the conductivity tensor, and for the longitudinal conductivity σ_{xx} we find :

$$H_0 = e^2 v_F^2 \rho(E_F) \left(\frac{2\tau_e}{\hbar} \right)^3 \frac{\pi}{16} \left[3\sigma^x \otimes \sigma^x + \sigma^y \otimes \sigma^y - 4Id \otimes Id \right] . \tag{6.7}$$

It is possible to draw several other diagrams than this first Hikami box to take into account the contribution of the cooperon to the conductivity. However, only two of these diagrams, depicted in Fig. 6.5 are of the same order in the perturbative parameter $\frac{1}{k_F l_e}$. These two diagrams write as :

$$H_1 = \gamma \int_{\vec{k},\vec{q}} G^A(\vec{k}) J_x G^R(\vec{k}) G^R(-\vec{q}) \otimes G^R(-\vec{k}) G^R(\vec{q}) J_x G^A(\vec{q}) , \tag{6.8}$$

$$H_2 = \gamma \int_{\vec{k},\vec{q}} G^A(-\vec{q}) G^A(\vec{k}) J_x G^R(\vec{k}) \otimes G^R(\vec{q}) J_x G^A(\vec{q}) G^A(-\vec{k}) . \tag{6.9}$$

Using the relation $\hbar/\tau_e = \pi\rho(E_F)\gamma$ we find that :

$$H_1 = H_2 = e^2 v_F^2 \rho(E_F) \left(\frac{2\tau_e}{\hbar} \right)^3 \frac{\pi}{16} \left[Id \otimes Id - \sigma^x \otimes \sigma^x \right] . \tag{6.10}$$

Collecting the results of Eq. (6.7) and Eq. (6.10), we obtain the "dressed" Hikami box for cooperons as the sum of the three Hikami boxes :

$$H^C = e^2 v_F^2 \rho(E_F) \left(\frac{2\tau_e}{\hbar} \right)^3 \frac{\pi}{16} \left[\sigma^x \otimes \sigma^x + \sigma^y \otimes \sigma^y - 2Id \otimes Id \right] . \tag{6.11}$$

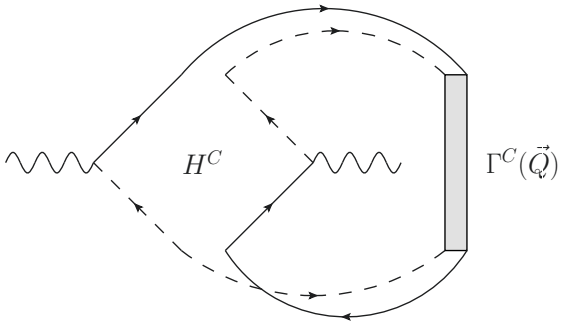

Figure 6.6: Diagrammatic representation of the calculation of the quantum correction to conductivity.

6.2.2 Quantum correction to conductivity

The quantum correction can now be computed by using the formula giving the cooperon structure factor in Eq. (6.4) and the dressed Hikami box for cooperon in Eq. (6.11) and we find :

$$\langle \Delta\sigma_{xx} \rangle = \frac{\hbar}{2\pi} tr \left[\int_{\vec{Q}} \Gamma^C(\vec{Q}) H_0 \right] \tag{6.12}$$

$$= \frac{e^2}{\pi\hbar} \int_{\vec{Q}} \frac{1}{Q^2} \, . \tag{6.13}$$

At first sight, the careful reader could notice that the integral does not converge, but in reality, this integral is a sum over all available momenta, and the domain of integration is restricted by both IR and UV cut-offs. Since the cooperon is a pure quantum interference effect, it disappears if the phase coherence is lost : this is the IR cut-off at $1/L_\phi$. In this restriction we assumed that the length of the sample L is larger than the coherence length, if not we need to change L_ϕ by L. Moreover, the cooperon has been approximated in the diffuse limit, on a length larger than the elastic scattering length, ensuring the UV cut-off at $1/l_e$ [1]. With these cut-offs on the integration domain, this correction reads :

$$\langle \Delta\sigma_{xx} \rangle = \frac{e^2}{2\pi^2\hbar} \ln\left(\frac{L_\phi}{l_e}\right) \, . \tag{6.14}$$

This correction is called weak antilocalization for two reasons : it is a weak correction since it is of the order of magnitude of the quantum of conductance e^2/h, compared to the classical part, much larger in the mesoscopic regime of

[1] Rigorously, we should consider the transport time τ_{tr} instead of the elastic scattering time τ_e, but since it appears only as a cut-off in the integration, it is not relevant for the physics.

weak disorder ; and it is an increase of the conductance, meaning that it is easier to travel through the sample : electrons seem less localized in absence of the magnetic field than when it is present. This difference from the more usual weak localization correction is also a consequence of the time-reversal symmetry, associated to the spin 1/2 nature of the Dirac fermions : in non-relativistic electron without spin $\mathcal{H} = \frac{\hbar^2 k^2}{2m}$, there is still time-reversal symmetry, ensuring the presence of a quantum correction to conductivity. However, for spinless, non-relativistic electrons, the scatterring probability is isotropic, and we observe backscattering processes, whereas it is impossible for the Dirac fermions since the scattering amplitude is the spin overlap, and a $\vec{k}, \vec{\sigma}$ backscattered as $-\vec{k}, \vec{\sigma}$ would break the time-reversal symmetry.

The conductivity is related to the probability of going from one end of the sample to the other $P(\vec{r}, \vec{r'})$. In presence of backscattering, the probability of return to the origin $P(\vec{r}, \vec{r'} = \vec{r})$ is enhanced, leading to an increase of the resistivity. The absence of backscattering in the case of Dirac fermions reduces the probability of return to the origin, thus electrons are less localized and then increase the conductivity.

We observe exactly the same expression for the weak anti-localization correction in the case of non-relativistic electrons submitted to a strong spin-orbit coupling[99], and we will see in Sec. 6.4 how we can explain this equality.

6.2.2.1 Transverse magnetic field

The breaking of time reversal symmetry by the introduction of a transverse magnetic field leads to a dephasing that kills the contribution of the cooperon. To calculate this effect, we need to know the contribution of the cooperon to the probability of return to the origin of a diffusive path. This is done in the case of non-relativistic electron in [32], and this derivation still holds for Dirac fermions. The effect of the magnetic field $\vec{B} = \vec{\nabla} \times \vec{A}$ can be neglected on the trajectories of excitations (the field is not large enough to bind them) but not in the phase of the Green's function. This corresponds, in the spatial representation of the Green's function, to add an extra phase :

$$G^{R/A}(\vec{r}, \vec{r'}, \vec{B}) = G^{R/A}(\vec{r}, \vec{r'}, \vec{0}) e^{i\phi(\vec{r}, \vec{r'})} , \tag{6.15}$$

where the phase ϕ is defined as $\phi(\vec{r}, \vec{r'}) = \frac{-e}{\hbar} \int_{\vec{r}}^{\vec{r'}} \vec{A}.d\vec{l}$. In the case of the cooperon, the two phases of the retarded and advanced Green's functions do not cancel out, as opposed to the diffuson. This changes the equation obeyed by the cooperon to be :

$$\left(-i\omega - D \left[\nabla_{r'} + i \frac{2e}{\hbar} \vec{A}(\vec{r'}) \right]^2 \right) \Gamma^C(\vec{r}, \vec{r'}, \omega) = \frac{\gamma}{\tau_e} \delta(\vec{r} - \vec{r'}) . \tag{6.16}$$

This problem can me mapped to a Schrödinger equation through the substitution $\hbar/2m \leftrightarrow D$ and $e \leftrightarrow 2e$. In the case of a uniform transverse magnetic field,

we obtain the Landau levels $E_n = \hbar\omega_C(n + 1/2)$, where ω_C is the cyclotron pulsation $\omega_C = \hbar eB/m$.

The integrated probability of return to the origin of the cooperon as a function of the time t and the magnetic field B is written as $Z^C(t, B) = \sum_n e^{-E_n t}$[32], and by analogy with a partition function we obtain :

$$Z^C(t, B) = \frac{BS/\Phi_0}{\sinh(4\pi BDt/\Phi_0)} . \tag{6.17}$$

In the case of Dirac fermions, the quantum correction to conductivity is then expressed as an integral over time of this return probability $\Delta\sigma \propto \int dt Z^C(t, B) e^{-\frac{t}{\tau_\phi}}$, and constraining the integration domain at a minimum time of τ_e gives :

$$\Delta\sigma(B) = \frac{e^2}{2\pi^2\hbar}\left[\Psi(\frac{1}{2} - \frac{B_e}{B}) - \Psi(\frac{1}{2} - \frac{B_\phi}{B})\right] . \tag{6.18}$$

where Ψ is the Digamma function and the characteristic fields $B_X = \hbar/(4eD\tau_X)$ have been introduced. Using the relation $\Psi(1/2 + x) \simeq \ln x$ when $x \longrightarrow 0$, we retrieve the result derived in the absence of the magnetic field.

6.3 Universal Conductance Fluctuations for Dirac fermions

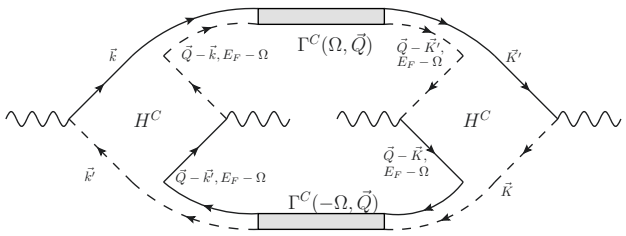

Figure 6.7: Diagram for the conductance fluctuations with Cooperons.

We have seen in Sec. 5.3 that the physical quantity relevant to the physics is the distribution probability of the conductance. Consequently, when a conductance is measured for different realizations of disorder, the departure from the mean-value can also be measured. Changing the realization of disorder can for example be done experimentally by changing the sample or applying an external magnetic field. The remarkable thing is that these fluctuations have the same amplitude of order $(e^2/h)^2$ even for different in nature experiments, and also that this amplitude does not depend on the size of the sample : it is the regime of universal conductance fluctuations.

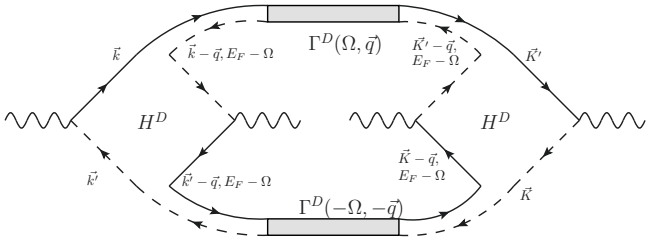

Figure 6.8: Diagram for the conductance fluctuations with Diffusons.

To derive the conductance fluctuations $\langle\delta\sigma^2\rangle = \langle\sigma^2 - \langle\sigma\rangle^2\rangle$, we need to take into account two kinds of diagrams containing either cooperons or diffusons. The Hikami box for cooperons has been calculated previously in Eq. (6.11). Proceeding similarly with the diffuson instead of cooperon structure factor we obtain the Hikami box for diffusons :

$$H^D = \rho(E_F)\left(\frac{2\tau_e}{\hbar}\right)^3 \frac{\pi}{16}\left[2Id\otimes Id + \sigma^x\otimes\sigma^x + \sigma^y\otimes\sigma^y\right]. \tag{6.19}$$

We have already performed an integration over the momentum (arising from the Kubo formula) in these expressions for the Hikami boxes. Hence we only need to plug a diffuson (resp. cooperon) structure factor between two H^D (resp. H^C). Summing these two diagrams (Fig. 6.8 and Fig. 6.7) and performing the spin trace, we obtain :

$$\langle\delta\sigma^2\rangle_1 = 8\left(\frac{e^2}{h}\right)^2 \frac{1}{V}\int_{\vec{q}}\frac{1}{q^4}\,. \tag{6.20}$$

The second part of the conductance fluctuations come from the diagrams represented in Fig. 6.9 that we have not yet considered. In the expression of the conductivity $\sigma = e^2\rho D$, we can separate the conductance fluctuations as the fluctuations originating from fluctuations of the diffusion constant D from the fluctuations originating from fluctuations of the density of states ρ. We have just calculated the first ones in Eq. (6.20), and the fluctuations due to fluctuations of the density of states require the determination of two additional Hikami boxes (one for Diffusons and one for Cooperons) :

$$\tilde{H}^D = \rho(E_F)\left(\frac{2\tau_e}{\hbar}\right)^3 \frac{\pi}{16}\left[Id\otimes Id + \sigma^x\otimes\sigma^x\right], \tag{6.21}$$

$$\tilde{H}^C = \rho(E_F)\left(\frac{2\tau_e}{\hbar}\right)^3 \frac{\pi}{16}\left[Id\otimes Id - \sigma^x\otimes\sigma^x\right]. \tag{6.22}$$

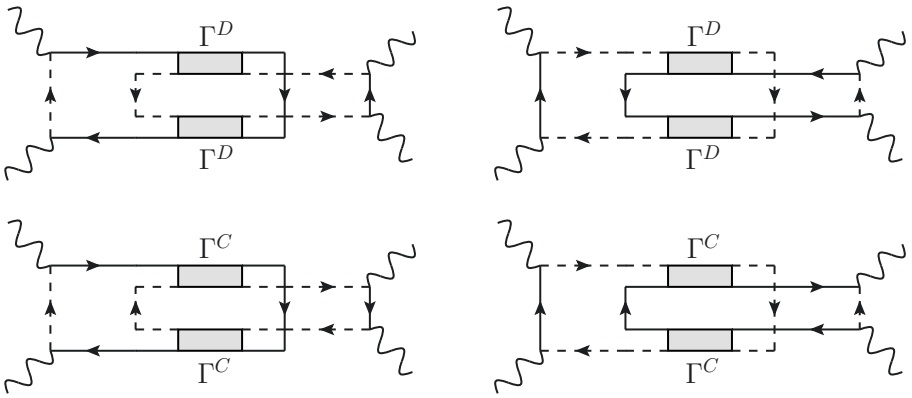

Figure 6.9: Diagrams for the second contribution to conductance fluctuations

The final result after contraction in spin space of these diagrams is :

$$\langle \delta\sigma^2 \rangle_2 = 4 \left(\frac{e^2}{h}\right)^2 \frac{1}{V} \int_{\vec{q}} \frac{1}{q^4} \, . \tag{6.23}$$

Summing the two contributions originating from fluctuations of the diffusion constant(6.20) and fluctuations of the density of states (6.23), we finally get the result :

$$\langle \delta\sigma^2 \rangle = \langle \delta\sigma^2 \rangle_1 + \langle \delta\sigma^2 \rangle_2 = 12 \left(\frac{e^2}{h}\right)^2 \frac{1}{S} \int_{\vec{q}} \frac{1}{q^4} \, . \tag{6.24}$$

Defining the phase coherent $L_\phi = \sqrt{D\tau_\phi(T)}$ and thermal lengthscales $L_T = \sqrt{\hbar D/T}$, we can focus on different regimes : for $L \ll L_\phi, L_T$, a proper regularization of the integral in (6.24) leads to the universal value

$$\langle \delta\sigma^2 \rangle = \frac{12}{\pi^4} \left(\frac{e^2}{h}\right)^2 \sum_{n_x=1}^{\infty} \sum_{n_y=0}^{\infty} \frac{1}{(n_x^2 + n_y^2)^2} \simeq 0.185613 \left(\frac{e^2}{h}\right)^2 . \tag{6.25}$$

This result is independent of the diffusion coefficient D and thus independent of the strength of the disorder, explaining the universality of these fluctuations. On the other hand, in the other limits [32]

$$\langle \delta\sigma^2 \rangle \simeq \frac{3}{\pi} \left(\frac{e^2}{h}\right)^2 \left(\frac{L_\phi}{L}\right)^2 \text{ for } L_\phi \ll L, L_T, \tag{6.26}$$

$$\simeq \frac{2}{3} \left(\frac{L_T}{L}\right)^2 \left(\frac{e^2}{h}\right)^2 \ln\left(\frac{L}{L_T}\right) \text{ for } L_T \ll L \ll L_\phi, \tag{6.27}$$

$$\simeq \frac{2}{3} \left(\frac{L_T}{L}\right)^2 \left(\frac{e^2}{h}\right)^2 \ln\left(\frac{L_\phi}{L_T}\right) \text{ for } L_T \ll L_\phi \ll L. \tag{6.28}$$

there is a dependance in D : the thermal length and the coherence length being defined as a function whereas the sample length is fixed.

6.3.1 Introduction of a transverse magnetic field

The introduction of a transverse magnetic field induces the suppression of the diagrams where a cooperon appears, which will reduce by a factor of two the amplitude of the fluctuations. This crossover is described as [32] :

$$\langle \delta\sigma(B)^2 \rangle = \frac{1}{2}\langle \delta\sigma(0)^2 \rangle \left[1 + \frac{B_\phi}{B}\Psi'(\frac{1}{2} + \frac{B_\phi}{B}) \right] \tag{6.29}$$

where Ψ is the Digamma function and $B_\phi(b) = \hbar/4eD(b)\tau_\phi$.

6.4 Symmetry classes and diffusion

As we have seen in Sec. 6.2.2 the quantum correction to conductivity, is in the case of Dirac fermions a weak antilocalization, which means that the resistance decreases when the magnetic field is suppressed. In the case of spinless, non-relativistic electrons we observe the opposite effect, called weak localization. However, this weak anti-localization is not specific to Dirac fermions : it has also been observed for non-relativistic electrons submitted to spin-orbit coupling. Surprisingly, even if the calculations are different in the case of non relativistic electrons with spin-orbit coupling than for the case of Dirac fermions with scalar disorder, the amplitude of the correction, as well as the amplitude of the conductance fluctuations are the same.

There are similarities between these two experiments: in the case of non-relativistic electrons with random spin-orbit coupling, the Green's functions are ballistic, and the anisotropy arises from the spin-orbit coupling to the impurities. For the Dirac fermions, the Green's functions are not diagonal in the spin-space, but the coupling to the impurities is. Moreover, both cases show a coupling between the momentum and the spin *via* the spin-orbit coupling. To show explicitly the similarity between these two experiments, we need to show that they correspond to the same physics.

The problem of diffusive waves in a random potential is the problem of Anderson localization[100]. There are universality classes to describe the transition to localization in the case of strong disorder. These universality classes depend on both the symmetry of the sample preserved by the disorder and the effective dimensionality of the diffusion. For topological insulators, these classes are only relevant for the surface states since the bulk is not a metal ; however we need to take into account the reduced dimensionality.

However these symmetry classes do not only describe the transport in the case of strong disorder, but they are also relevant to describe the perturbative regime of weak disorder : for a given universality class, the only parameter

necessary to describe all the transport experiments is the diffusion coefficient, and knowledge of this coefficient and of the symmetry class is enough to determine the value of the quantum correction to conductivity and the amplitude of the conductance fluctuations.

In the case of metals, there are only three classes : the orthogonal, the symplectic and the unitary class. The class of a system is fully determined by the time-reversal operation Θ :

- If the Hamiltonian is time-reversal symmetric and $\Theta^2 = Id$, it is the orthogonal class. This is for example the case of non-relativistic electron with a scalar disorder.

- If the Hamiltonian is time-reversal symmetric and $\Theta^2 = -Id$, it is the symplectic class. This happens for example in the case of relativistic electrons, such as in graphene and topological insulator surface states. It is also the case of non-relativistic electrons in presence of spin-orbit coupling. Since both cases are described with the same model, we expect to find the same results for the amplitude of the quantum correction or the conductance fluctuations[99].

- Finally, a breaking of the time-reversal symmetry leads to the unitary class.

The breaking of the time-reversal symmetry can be done for example by applying a transverse magnetic field, and this crossover from the orthogonal or symplectic class to the unitary class is what is observed in a magnetoconductance measurement.

Instead of thinking in terms of symmetry classes, it could be convenient to see that for every symmetry class there is a given number of diffusive modes associated : there are 8 (1 singlet and 3 triplets for both diffuson and cooperon) in the orthogonal class, 2 (the diffuson and the cooperon singlets) in the symplectic class and only one in the unitary class (the cooperon is suppressed). We have seen that by nature, the cooperon is only observable when there is time-reversal symmetry (we flipped one of the two Green's functions of a diffuson), this is why the breaking of time-reversal symmetry by a magnetic field change the symmetry class to unitary and suppress the contributions of the cooperon.

A 2 dimensional metal such as graphene and the surface states of a topological insulator belong to the same symmetry class, however there is a deep difference in the strong disorder limit. In the case of the 2 dimensional metal, the eigenstates must appear in pairs, this is known as the fermion doubling theorem, whereas at the surface of a 3 dimensional topological insulator, they have to be in an odd number. In presence of strong disorder, Anderson localization tells that the metal becomes an insulator. This is not the case for

topological insulator as the surface states can be localized only by pairs, implying that that at least one surface state is not localized, and the insulating regime is not reached as long as the disorder preserves the gap[97].

For particulars, as every one knows, make for virtue and happiness; generalities are intellectually necessary evils.

Aldous Huxley, *Brave New World*

Chapter 7

Hexagonal warping of the Fermi surface for topological insulators surface states

7.1 Model for hexagonal warping

For Dirac fermions, the Fermi surface, a cut of the dispersion relation at a given energy, is a pure circle. However, ARPES experiments[61] on the surface states of Bi_2Te_3 showed that instead of being circular, the Fermi surface presents a six-fold deformation which becomes more and more visible as we move away from the Dirac point : from a circle, the Fermi surface turns into a hexagon then into a snowflake (cf Fig. 7.1).

The origin of such a behavior has been understood by L. Fu[64] by studying the band structure of Bi_2Te_3 using $k.p$ theory. This theory corresponds to an expansion of the dispersion relation at small energy and small momentum around the Γ point. The first term in the development explains the Hamiltonian we have used in the previous chapter, but there are higher order terms that have been neglected. They are treated by adding a new term in the

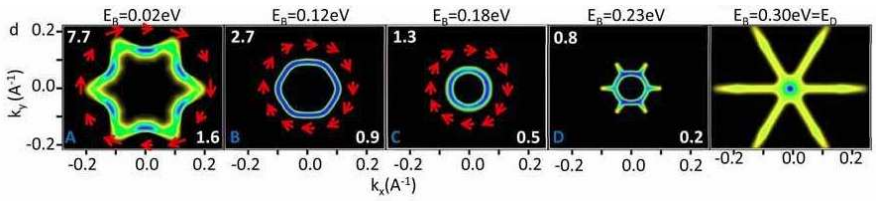

Figure 7.1: ARPES data showing the deformation of the Fermi surface when the Fermi energy is moved away from the Dirac point (from right to left)[98].

Hamiltonian which becomes for Bi_2Te_3 surface states :

$$\mathcal{H} = \hbar v_F(k_x\sigma^y - k_y\sigma^x) + \frac{\lambda}{2}(k_+^3 + k_-^3)\sigma^z \ , \tag{7.1}$$

where we have noted $k_\pm = k_x \pm ik_y$.

Let us take a closer look to this Hamiltonian. First of all, we can perform a $\pi/2$ rotation around the spin z-axis and obtain the $\vec{k}.\vec{\sigma}$ form of the Hamiltonian we used previously. There are only two parameters in this Hamiltonian, the Fermi velocity v_F which has been renormalized by going to an higher order in the $k.p$ theory, and the parameter λ that we will call the warping parameter. Indeed, this second term of the Hamiltonian is the one that breaks the continuous rotational symmetry into a six-fold degeneracy that can be understood as the combination of the three-fold symmetry of the crystalline structure of Bi_2Te_3 and the time-reversal symmetry[101].

A similar departure from Dirac physics is also observed in graphene, but in this case, the deformation is a triangular warping since the time-reversal symmetry in graphene projects a Dirac cone into a different valley Dirac cone. The fact that this warping tilts the spin out of the $x-y$ plane, and that it has not been studied in graphene are the motivation for this work.

7.1.1 Diagonalization of the Hamiltonian

Starting from the Hamiltonian :

$$\mathcal{H} = \hbar v_F(\vec{k}.\vec{\sigma}) + \frac{\lambda}{2}(k_+^3 + k_-^3)\sigma^z \ , \tag{7.2}$$

it is easy to determine the dispersion relation :

$$E(\vec{k}) = \pm\sqrt{\hbar^2 v_F^2 k^2 + \lambda^2 k^6 \cos^2 3\theta} \ , \tag{7.3}$$

where $\vec{k} = (k, \theta)$ in polar representation. We plot this dispersion relation in Fig. 7.2, and check that it reproduces well the behaviour seen experimentally in Fig7.1.

To quantify the strength of this hexagonal warping, a geometric factor depending on the extremal amplitude of the momentum around the Fermi surface has been introduced[98] :

$$w = w_{max}\frac{k_{max} - k_{min}}{k_{max} + k_{min}} \qquad \text{with} \qquad w_{max} = \frac{2+\sqrt{3}}{2-\sqrt{3}} \simeq 13.9 \ . \tag{7.4}$$

This geometric factor depends only on the shape of the Fermi surface, for example, two Fermi surfaces differing only by a simple homothetic transformation will have the same geometric factor. Since the shape of the Fermi

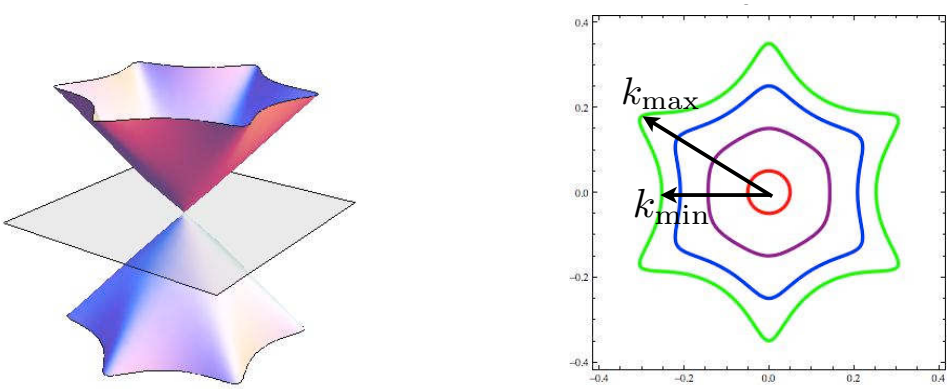

Figure 7.2: Left : Numerical plot of the dispersion relation. Right : Fermi surface for different value of the Fermi energy.

surface changes with the Fermi energy, we introduced the dimensionless parameter $b = \frac{\lambda E_F^2}{2\hbar^3 v_F^3}$ obtained from the Hamiltonian parameters as another measure of the warping strength. The coefficients are linked through the relation $b(w) = \sqrt{w w_{max} \frac{(w_{max}+w)^2}{(w_{max}-w)^3}}$, showing that indeed an increase of b corresponds to an increase of w, and that they both increase with the Fermi energy. Two sets of values of the coefficients appear of interest : when there is no deformation, corresponding to a circular Fermi surface $b = 0$ and $w = 0$; when the the Fermi surface is a hexagon $w = 1$, $b = 2/(3\sqrt{3}) \simeq 0.38$. When the Fermi energy is increased, the edges curves inward and we obtain a snow-flake like Fermi surface, with $w > 1$.

Using experimental ARPES data showing the form of the Fermi surface, it is possible to derive the value of the coefficient w, and thus a range of values of b. Using the experimental values for the Bi_2Se_3 compound $\lambda = 128$ eV.$\mathring{A}^3$, $v_F = 3.55$ eV.$\mathring{A}$ from [102] we obtain relatively small values of warping $0.04 < b < 0.09$ for energies $0.05eV < E < 0.15eV$, and similarly $0.0 < b < 0.04$ with the values $\lambda = 95$ eV.$\mathring{A}^3$, $v_F = 3.0$ eV.$\mathring{A}$ and 0.00eV $< E <$ 0.15eV from [103]. On the other hand, the experimental values for the Bi_2Te_3 compound $\lambda = 250$ eV.$\mathring{A}^3$ and $v_F = 2.55$ eV.$\mathring{A}$ [61, 15] lead to a warping factor ranging from $b = 0.13$ for $E = 0.13$ eV to $b = 0.66$ for $E = 0.295$ eV.

This range of values for b first led to consider a perturbative approach[104][105], but we will see that for values of b larger than 0.2, this perturbative approach appears clearly unapplicable.

To simplify the future calculations we introduce $k_F = E_F/\hbar v_F$ and $k = k_F \tilde{k}(\theta)$ so that the Fermi surface is defined by the equation :

$$1 = \tilde{k}^2(\theta) + 4b^2\tilde{k}^6(\theta) \; . \tag{7.5}$$

7.2 Boltzmann approach perturbative in warping

To calculate the classical conductivity through the Boltzmann method we need the same ingredients as in the previous chapter, but we will develop the series expansion up to the fourth order in b.

7.2.1 Elastic scattering time

The diagonalization of the Hamiltonian $\mathcal{H} = \hbar v_F(\vec{k}.\vec{\sigma}) + \frac{\lambda}{2}(k_+^3 + k_-^3)\sigma^z$ gives the energy $E = \sqrt{\hbar^2 v_F^2 k^2 + \lambda^2 k^6 \cos^2 3\theta}$ far from the Dirac point (this is why we neglect the negative energy excitations). The corresponding spinorial part of the eigenvector is :

$$|\vec{k} = (k,\theta)\rangle_s = \begin{pmatrix} \cos\phi \\ \sin\phi e^{i\theta} \end{pmatrix} \qquad \text{where} \qquad e^{i2\phi} = 2b\tilde{k}^3\cos\theta + i\tilde{k}\ . \tag{7.6}$$

7.2.1.1 Scattering amplitude

Using this value of the eigenvector, it is possible to calculate the spinor overlap between $|\vec{k}\rangle$ and $|\vec{k'}\rangle$. For a given value of the warping parameter b, the value of $\tilde{k}(\theta)$ is fixed, this is equivalent to say that the indication of the Fermi energy and of the the direction of the wavevector is enough to determine its length. We derive exactly the value of the scattering probability from $\vec{k}$ to $\vec{k'}$, on the disorder $|\langle\vec{k'}|V|\vec{k}\rangle|^2$. This probability is proportional to the spinor overlap $g(\vec{k},\vec{k'}) = |_s\langle\vec{k'}|\vec{k}\rangle_s|^2$, that we express as a function of the relative angle between $\vec{k}$ and $\vec{k'}$, the direction of the incoming wavevector and the value of the warping parameter b. It does not depend on the Fermi energy or the length of the wavevectors since they have been absorbed in the definition of b and $\tilde{k}$. We obtain :

$$g(\vec{k},\vec{k'}) = \frac{1}{2}\left[1 + \cos 2\phi\cos 2\phi' + \sin 2\phi\sin 2\phi'\cos(\theta-\theta')\right]\ . \tag{7.7}$$

We can compare this to the result of pure Dirac fermions, where $b = 0$. In this case $\phi = \pi/2$, and we recover the result of Eq. (5.9), $g(\vec{k},\vec{k'}) = \frac{1}{2}(1+\cos(\theta-\theta'))$.

The calculated scattering probability is plotted in Fig.7.3 ; we can notice that the anisotropy is increased by the warping. Moreover, there is now a dependance of the scattering probability in the direction of the incoming wavevector which was absent in the case of pure Dirac fermions.

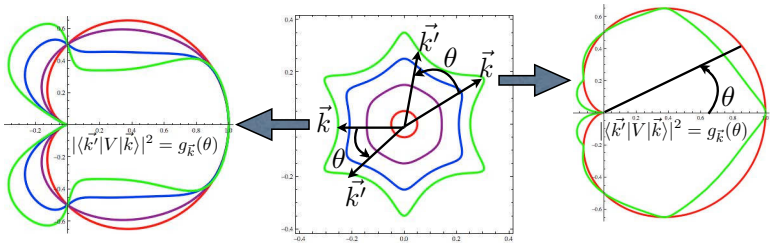

Figure 7.3: Scattering probability as a function of the angle between the incoming and the outgoing wavevector, for different values of the warping, and for two different directions of the incoming wavevector.

7.2.1.2 Density of state and elastic scattering time

The density of state $\rho(E) = \int \frac{d\vec{k}}{(2\pi)^2}\delta(E - E(\vec{k}))$ is now derived by integrating on constant energy contours and we obtain :

$$\rho(E_F) = \frac{E_F}{2\pi\hbar^2 v_F^2}\int \frac{d\theta}{2\pi}\frac{1}{1 + 12b^2\tilde{k}(\theta)\cos^2 3\theta} \ . \tag{7.8}$$

Noting X^0 the value of the quantity X in the absence of warping as derived in the previous chapter $X^0 = X(b = 0)$, we perform a series expansion and we obtain at the fourth order in b :

$$\rho(E_F) = \rho^0(E_F)\left(1 - 6b^2 + 90b^4 + o(b^4)\right) \ . \tag{7.9}$$

The calculation of the elastic scattering time through the Fermi golden rule :

$$\frac{1}{\tau_e(E_F)} = \langle \int \frac{d\vec{k}}{(2\pi)^2} \quad \frac{2\pi}{\hbar}|\langle \vec{k}'|V|\vec{k}\rangle|^2\delta(E(\vec{k}') - E_F)\rangle \ , \tag{7.10}$$

can also be derived by using the same integration on constant energy contours. However the relation between the elastic scattering time and the density of states through the amplitude of the disorder $\hbar/\tau_e = \pi\rho\gamma$ remains. As a result we find that :

$$\frac{1}{\tau_e} = \frac{1}{\tau_e^0}\left(1 - 6b^2 + 90b^4 + o(b^4)\right) \ . \tag{7.11}$$

The effect of the warping is to reduce the density of state : the warping is responsible for an increase of the Fermi surface coming from the curving of the edges, since there is more space available for the same number of energy states, the density of states decreases. On the other hand, the elastic scattering time is increased : this lowering of the density of states induces less scattering of the particles.

This two effects seem to counterbalance so the resulting effect of the hexagonal warping on the diffusion is difficult to guess. However, we have seen that

the interesting time to describe the conductivity is not the elastic scattering time when the scattering is anisotropic, but the transport time. To obtain it, we need to solve the Boltzmann equation.

7.2.2 Boltzmann equation

To solve the Boltzmann equation

$$-e\vec{E}.\frac{\partial f}{\partial \vec{k}} = \langle \int \frac{d\vec{k'}}{(2\pi)^2} \quad 2\pi|\langle \vec{k'}|V|\vec{k}\rangle|^2 \delta(E(\vec{k'}) - E_F) \left[f(\vec{k'}) - f(\vec{k})\right]\rangle \ , \quad (7.12)$$

we will use the linearized ansatz $f(\vec{k}) = n_F(\epsilon(\vec{k})) + \frac{\partial n_F}{\partial \epsilon}\bar{f}(\theta)$ with $\bar{f}$ linear in the electric field. For an electric field along the x-axis, this corresponds to solve the equation :

$$-eE_x.\frac{\partial \epsilon}{\partial k_x} = 2\pi\gamma \int \frac{d\theta'}{(2\pi)^2}|\langle \vec{k'}|\vec{k}\rangle|^2 \frac{k_F|_{\theta'}}{\frac{\partial \epsilon}{\partial k}|_{\theta'}} \left[\bar{f}(\theta') - \bar{f}(\theta)\right] , \quad (7.13)$$

We derive the quantities present in this equation up to fourth order in b :

$$\begin{aligned}
\frac{\partial \epsilon}{\partial k_x} =& \hbar v_F \left(\cos\theta + b^2 \cos 3\theta(11\cos 2\theta + \cos 4\theta)\right. \\
&\left. + \ b^4 \cos^3 3\theta(-109\cos 2\theta + 11\cos 4\theta)\right) \ , \quad (7.14)\\
|\langle \vec{k'}|\vec{k}\rangle|^2 =& \frac{1}{2}\left[1 + \cos(\theta - \theta') + b^2 h_1(\theta,\theta') + b^4 h_2(\theta,\theta')\right] \ , \quad (7.15)\\
h_1(\theta,\theta') =& 4\cos 3\theta \cos 3\theta' - 2(\cos^2 3\theta + \cos^2 3\theta')\cos(\theta - \theta') \ , \quad (7.16)\\
h_2(\theta,\theta') =& -24\cos 3\theta \cos 3\theta'(\cos^2 3\theta + \cos^2 3\theta') \quad (7.17)\\
&+ (4\cos^2 3\theta \cos^2 3\theta' + 22\cos^4 3\theta + 22\cos^4 3\theta')\cos(\theta - \theta') \ ,\\
\frac{k_F|_{\theta'}}{\frac{\partial \epsilon}{\partial k}|_{\theta'}} =& \frac{E_F}{\hbar^2 v_F^2}\left(1 - 12b^2\cos^2 3\theta' + 240 b^4 \cos^4 3\theta'\right) \ , \quad (7.18)
\end{aligned}$$

and solving the equation iteratively in powers of b in the expansion of $\bar{f}$ gives to fourth order in b :

$$\begin{aligned}
\bar{f}(\theta) \quad = \quad & e v_F \tau_e E_x \Big[2\cos\theta + b^2(18\cos\theta + 5\cos 5\theta - \cos 7\theta) \quad (7.19)\\
& - \frac{b^4}{4}(522\cos\theta + 20\cos 5\theta + 44\cos 7\theta + 49\cos 11\theta - 11\cos 13\theta)\Big].
\end{aligned}$$

7.2.2.1 Classical conductivity

The current is then calculated according to :

$$j_x = \int \frac{d\vec{k}}{(2\pi)^2} e \frac{\partial \epsilon}{\partial k_x}\bar{f}(\theta)\delta(\epsilon(\vec{k}) - E_F) = \sigma E_x \ , \quad (7.20)$$

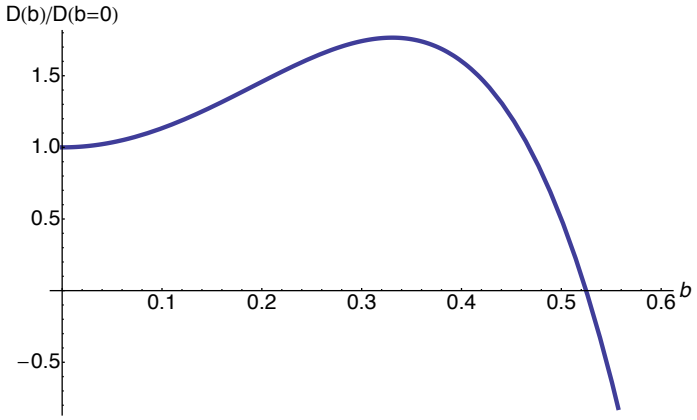

Figure 7.4: Diffusion constant calculated perturbatively to fourth order as a function of the warping parameter b.

leading to the conductivity :

$$\sigma = e^2\rho(E_F)v_F^2\tau_e\left(1 + 8b^2 - 58b^4 + o(b^4)\right). \tag{7.21}$$

We can check that in the limit $b \longrightarrow 0$ of no hexagonal warping, the precedent result of Eq. (5.12) is retrieved since $\rho(E_F)\tau_e = \rho^0(E_F)\tau_e^0 = \pi\hbar\gamma$. This equation defines the diffusion constant $D = D^0(1 + 14b^2 - 64b^4)$. In the end, even if the density of state and the elastic scattering time are effected in opposite way and counterbalance, the increased anisotropy of the scattering is dominant and is responsible for an increase of the conductivity with the warping.

This perturbative approach in b gives a tendency for the effect of the warping on the conductivity, however, for the extremal values of b around 0.6, this gives a negative value for the conductivity (cf Fig. 7.4), suggesting that the larger experimental values for the warping parameter b are beyond the radius of convergence of the series expansion and that an approach non perturbative in warping is necessary.

7.3 Diagrammatic technique : derivation of the classical conductivity

To calculate the classical conductivity with the diagrammatic technique, we follow the method used in the previous chapter : the first step consists in the calculation of the self-energy thus providing the disorder averaged Green's functions. Then, the classical Drude conductivity is calculated as the sum of two contributions, the one where there is no disorder induced coupling between the advanced and the retarded Green's functions that we called the bare conductivity, and the one arising from the vertex renormalization coming

from the diffuson. All this study will be done non-perturbatively in the warping parameter b and confronted to the previous perturbative result obtained by the resolution of the Boltzmann equation.

7.3.1 Averaged Green's function and elastic scattering time.

The averaged Green's function is obtained by calculating the self-energy correction and averaging over disorder as we did in the previous chapter. The corresponding disorder averaged Green's functions read :

$$\langle G^{R/A}(\vec{k})\rangle = \frac{(E \pm i\hbar/2\tau_e)Id + \hbar v_F \vec{k}\ .\ \vec{\sigma} + \lambda k^3 \cos(3\theta)\sigma^z}{(E \pm i\hbar/2\tau_e)^2 - \hbar^2 v_F^2 k^2 - \lambda^2 k^6 \cos^2(3\theta)}\ , \tag{7.22}$$

where the elastic scattering time for the warped (resp. unwarped) conical Dirac fermion τ_e (resp. $\tau_e^{(0)}$) is defined by :

$$\rho\tau_e = \frac{\hbar}{\pi\gamma} = \rho^{(0)}\tau_e^{(0)}. \tag{7.23}$$

We assume that the phase coherence time $\tau_\phi \gg \tau_e$ in order to be in the regime of coherent transport. By using the parameterization $\tilde{k}(\theta)$ of the Fermi surface shape defined in Eq. (7.5) as $1 = \tilde{k}^2(\theta) + 4b^2\tilde{k}^6(\theta)$, we obtain the non perturbative expression for the the density of states :

$$\frac{\rho}{\rho^{(0)}} = \alpha(b) = \int_0^{2\pi} \frac{d\theta}{2\pi} \frac{1}{1 + 12\ b^2\tilde{k}^4(\theta)\cos^2(3\theta)} = \frac{\tau_e^{(0)}}{\tau_e}\ . \tag{7.24}$$

As expected from the perturbative result, we find an increase of the scattering time τ_e by the warping whereas the density of states is reduced by the same factor. Once again, these two counterbalancing effects do not teach anything about the classical conductivity since it is only determined by the transport time or the diffusion constant, and not by the elastic scattering time. To access the conductivity, we need to follow the procedure explained in the previous chapters (starting from Sec. 5.3).

7.3.2 Diagrams for the classical conductivity

We remind the reader that for a given impurity configuration, the conductivity is given by the Kubo formula :

$$\sigma = \sigma_{xx} = \frac{\hbar}{2\pi L^2} \Re\mathrm{Tr}\left[j_x G^R j_x G^A\right]\ , \tag{7.25}$$

In this expression and below, Tr denotes a trace over the electron's Hilbert space (momentum and spin quantum numbers). The current operator j_α is obtained from the Hamiltonian Eq. (7.2) by inserting the vector potential *via*

the minimal coupling substitution $\vec{k} \to \vec{k} - (e/\hbar)\vec{A}$ and using the definition $j_\alpha = \frac{\delta H}{\delta A_\alpha}$. We obtain a warping dependent current operator :

$$j_x = (-e)\left(v_F\ \sigma_x + \frac{3\lambda}{\hbar}\sigma_z(k_x^2 - k_y^2)\right). \tag{7.26}$$

We can check that in the limit of the absence of the warping term $\lambda = 0$, only the constant term σ^x remains. However, in the presence of the warping, there is also a dependance of the current operator in the momentum $\vec{k}$: the previous technique of the current operator renormalization is no longer valid. Instead the classical mean conductivity is obtained from the bubble diagram of Fig. 7.5 where the propagating lines are the retarded and advanced disorder averaged Green functions Eq. (7.22). This classical conductivity is the sum of two terms : σ_A and σ_B. The contribution of diagram A in Fig. 7.5 is defined

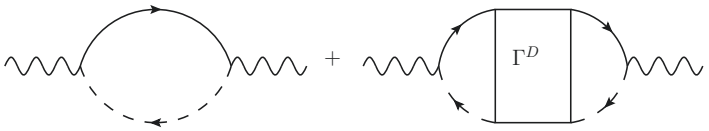

Figure 7.5: Diagrammatic representation of the two contributions σ_A and σ_B to the classical conductance.

at $\vec{q} = 0$ and $\omega = 0$ by :

$$\sigma_A = \frac{\hbar}{2\pi}\int \frac{d\vec{k}}{(2\pi)^2}\ \mathrm{tr}\left[j_x(\vec{k})\langle G^R(\vec{k}, E_F)\rangle j_x(\vec{k})\langle G^A(\vec{k}, E_F)\rangle\right], \tag{7.27}$$

where tr represents a trace over the spin quantum numbers. Performing explicitly the trace and the integration over the momentum $k = |\vec{k}|$, we obtain the following expression:

$$\sigma_A = \frac{\hbar e^2 v_F^2}{2\pi\gamma}\frac{\alpha(b) + 5\beta(b) + \delta(b)}{\alpha(b)}, \tag{7.28}$$

which is non perturbative in b. The function $\alpha(b)$ has been defined in Eq. (7.24) and we have introduced $\beta(b)$ and $\delta(b)$ as :

$$\alpha(b) = \int_0^{2\pi}\frac{d\theta}{2\pi}\frac{1}{1 + 12\ b^2\tilde{k}^4(\theta)\cos^2(3\theta)}, \tag{7.29}$$

$$\beta(b) = \int_0^{2\pi}\frac{d\theta}{2\pi}\frac{4b^2\cos^2(3\theta)\tilde{k}^6(\theta)}{1 + 12b^2\cos^2(3\theta)\tilde{k}^4(\theta)}, \tag{7.30}$$

$$\delta(b) = \int_0^{2\pi}\frac{d\theta}{2\pi}\frac{36b^2(\tilde{k}^4(\theta) - \tilde{k}^6(\theta))}{1 + 12b^2\cos^2(3\theta)\tilde{k}^4(\theta)}, \tag{7.31}$$

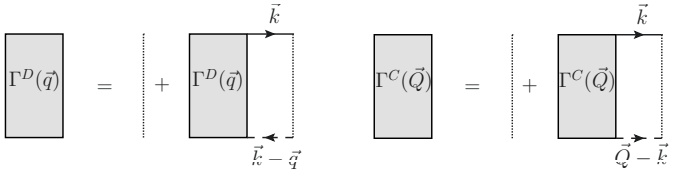

Figure 7.6: Schematic representation of the Diffuson and Cooperon structure factors. The dotted lines correspond to disorder correlators, while the plain and dashed lines represent retarded and advanced Green's functions.

where $\tilde{k}(\theta)$ has been introduced in Eq. (7.5) as $k = k_F\tilde{k}(\theta)$.

The contribution of the diagram B in Fig. 7.5 accounts for the contribution of the so-called diffuson [32]. Retaining only the dominant contribution of the integral, we can write is explicitly as :

$$\sigma_B(\vec{q},\omega) = \frac{\hbar}{2\pi}\mathrm{tr}\left[J_x\Gamma^{(d)}(\vec{q},\omega)J_x\right], \tag{7.32}$$

where the vertex operator J is defined by :

$$J_x = \int \frac{d\vec{k}}{(2\pi)^2}\langle G^A(\vec{k},E)\rangle\ j_x(\vec{k})\ \langle G^R(\vec{k},E)\rangle = J\ \sigma_x\ . \tag{7.33}$$

A contraction over the spin indices is assumed, resulting in the proportionality to σ_x.

The diffuson structure factor Γ^D in Eq. (7.32) is defined diagrammatically as in Eq. (5.32) in the absence of warping , and satisfies the same recursive Dyson equation, solved by the expression $\Gamma^D(\vec{q},\omega) = \gamma\left[Id\otimes Id - \gamma P^D(\vec{q},\omega)\right]$ where P^D is defined as :

$$P^D(\vec{q},\omega) = \int \frac{d\vec{k}}{(2\pi)^2}\langle G^R(\vec{k},E)\rangle\ \langle G^A(\vec{k}-\vec{q},E-\omega)\rangle. \tag{7.34}$$

As in the case of the absence of warping, this diffuson structure factor can be separated into 4 modes, one which is the singlet at $q = 0$ and $\omega = 0$ which is the only diffusive one, and the three triplets that do not contribute at long range, but with one of them being responsible of the renormalization of the transport time. To obtain this contribution to the conductivity, we do not need to solve exactly the Dyson equation : we parametrize the diffuson structure factor at $\omega = 0$ and $\vec{q} = \vec{0}$ using three parameters as follows :

$$\Gamma^{(D)} = a_1 Id\otimes Id + a_2(\sigma^x\otimes\sigma^x + \sigma^y\otimes\sigma^y) + a_3\sigma^z\otimes\sigma^z. \tag{7.35}$$

Then, using this parameterization and the expression for the current operator associated to an advanced and a retarded Green's function of Eq. (7.33) and

performing the resulting trace we obtain :

$$\sigma_B = J^2(a_1 - a_3) \; . \tag{7.36}$$

We derive the value of J as a function of the parameter $\alpha(b)$ and $\beta(b)$ defined in Eq. (7.24) and Eq. (7.30) : $J = \frac{-ev_F}{\gamma}\frac{\alpha(b)+2\beta(b)}{\alpha(b)}$. Similarly, we can derive the value of $a_1 - a_3$, expressing P^D as a function of $\alpha(b)$ and $\beta(b)$ and using the relation $\Gamma = \gamma(Id \otimes Id - \gamma P^D)^{-1}$: $a_1 - a_3 = \frac{\alpha(b)}{\alpha(b)+\beta(b)}$. With these two relations we obtain :

$$\sigma_B = J^2(a_1 - a_3) = \frac{\hbar e^2 v_F^2}{2\pi\gamma}\frac{(\alpha(b) + 2\beta(b))^2}{\alpha(b)(\alpha(b) + \beta(b))} \; . \tag{7.37}$$

It is now possible to add the two contributions of Eq. (7.28) and Eq. (7.37) and obtain the full expression for the classical conductivity, and this allows us to define the diffusion constant D from the Einstein relation $\sigma_{cl} = \sigma_A + \sigma_B = e^2\rho D$. Finally we obtain an expression for the diffusion constant :

$$D \;\; = \;\; \frac{v_F^2\tau_e}{2}\left(\frac{\alpha(b) + 5\beta(b) + \delta(b)}{\alpha(b)} + \frac{(\alpha(b) + 2\beta(b))^2}{\alpha(b)(\alpha(b) + \beta(b))}\right) \; . \tag{7.38}$$

which is non perturbative in the warping parameter b.

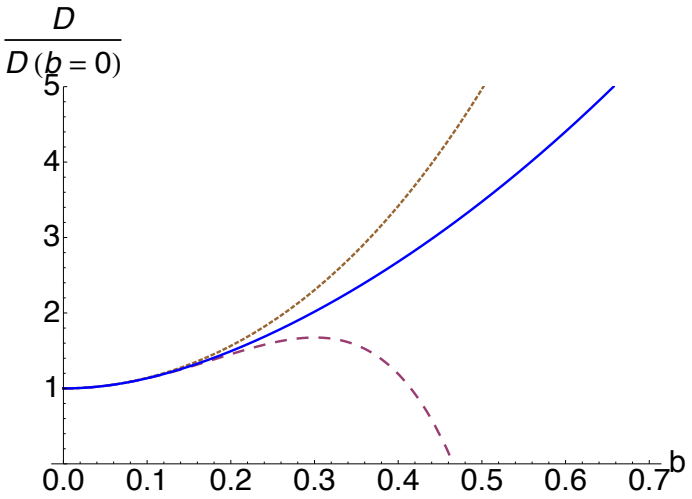

Figure 7.7: Profile of the diffusion constant as a function of warping intensity b. The plain line corresponds to the expression non perturbative in the warping amplitude b, while the dashed curves corresponds to perturbative results to order b^2 and b^4.

In the limit $b \to 0$ of absence of warping, we recover the known result for Dirac fermions with scalar disorder with a diffusion constant $D = v_F^2\tau_e = v_F^2\tau_{tr}/2$ with a transport time $\tau_{tr} = 2\tau_e$ accounting for the inherent anisotropic scattering of Dirac fermions on scalar disorder.

Fig. 7.7 shows the evolution of the diffusion constant as a function of the warping parameter b and the increase by a factor up to 4 of the diffusion coefficient within the range of experimental values of b which can be as high as 0.6. This increase comes from the stronger anisotropy of the scattering when the hexagonal warping strength is increased, whereas the renormalization of the density of states and elastic scattering time balance. This increase of the diffusion coefficient corresponds to a stronger increase of the transport time compared to the elastic scattering time since this diffusion coefficient accounts for both the renormalization of the density of states and the renormalization of the transport time. It is important to notice that this diffusion coefficient is now a function of the warping parameter b : for a given sample with fixed Hamiltonian parameters λ and v_F, the diffusion coefficient can be modified by changing the Fermi energy. The effects of such a change will be examined in the following sections.

Finally, we observe that this non perturbative calculation shows a strong departure of the perturbative approach when b approaches the maximum of the experimental values, showing that a non perturbative in warping approach is necessary to describe transport experiments.

7.4 Quantum corrections to conductivity and universal conductance fluctuations

The warping term $\mathcal{H}_w = \frac{\lambda}{2}(k_+^3 + k_-^3)\sigma^z$ preserves the time-reversal symmetry. Consistently with Sec. 6.4, we can check that the time-reversal operation squares to minus identity $\Theta^2 = -Id$, so we are still in the symplectic class.

We have derived the value of the diffusion constant, so we already know the value of the quantum correction to conductivity and the amplitude of the conductance fluctuation. In Sec. 6.2.2, we have shown that the weak anti-localization correction does not depend on the diffusion constant, so we expect the result to hold in this case. The next section intends to show it explicitly.

7.4.1 Calculation of the quantum correction to conductivity

To obtain the quantum correction to conductivity, the first step is to obtain the new Hikami box H^C, the difficulty arising from the dependence of the current operator on the momentum $j_x = e\left(-v_F\sigma_x + \frac{3\lambda}{\hbar}\sigma_z(k_x^2 - k_y^2)\right)$. Reminding $\Sigma^x = j_x + j_x P^D \Gamma^D$, we express the first Hikami box as :

$$H_0^C = \int_{\vec{k}} \left[G^A(\vec{k})\Sigma^x G^R(\vec{k}) G^R(-\vec{k})\Sigma^x G^A(-\vec{k}) \right]. \tag{7.39}$$

We perform this integral using polar coordinates, and integrate the radial part :

$$H_0^C = \frac{e^2 v_F^2 \tau_e^2}{4\gamma\hbar} \frac{\tau_e}{\tau_e^{(0)}} \int \frac{d\theta}{2\pi} \frac{A_+ B A_+ \otimes A_- B A_-}{1 + 12 b^2 \tilde{k}(\theta)^4 \cos^2(3\theta)} , \tag{7.40}$$

$$A_\pm = Id \pm \tilde{k}(\theta) \left(\cos\theta \sigma^x + \sin\theta \sigma^y\right) + 2b\ \tilde{k}^3(\theta) \cos(3\theta) \sigma^z , \tag{7.41}$$

$$B = \left(2 + \frac{\beta}{\alpha+\beta}\right) \sigma^x + 6b\ \tilde{k}^2(\theta) \cos(2\theta) \sigma^z . \tag{7.42}$$

The two other Hikami boxes, where an impurity line links two Green's functions can be calculated by the method used above, and summing the three Hikami box, one can write the result for the Hikami box as :

$$H^C = \frac{e^2 v_F^2 \tau_e^2}{4\gamma\hbar} H(b) , \tag{7.43}$$

where $H(b)$ is a complex expression containing angular integral functions of b. We need to close this Hikami box with a Cooperon structure factor :

$$\Gamma^C = \frac{\gamma}{\tau_e} \frac{1}{D(b) Q^2} \frac{1}{4} \left(Id \otimes Id - \sigma^x \otimes \sigma^x - \sigma^y \otimes \sigma^y - \sigma^z \otimes \sigma^z\right) . \tag{7.44}$$

We assumed that the cooperon structure factor can still be approximated around $Q = 0$ by a singlet diffusive state, with the relevant diffusion constant $D(b)$. Introducing :

$$h(b) = \mathrm{tr}[H(b) \frac{1}{4} \left(Id \otimes Id - \sigma^x \otimes \sigma^x - \sigma^y \otimes \sigma^y - \sigma^z \otimes \sigma^z\right)] , \tag{7.45}$$

as the trace over the spin space of the cooperon structure factor and the Hikami box, we obtain the quantum correction to the conductivity :

$$\langle \Delta\sigma(b) \rangle = \frac{\hbar}{2\pi} \mathrm{Tr}(H^C \Gamma^C) = \frac{e^2}{h} \frac{v_F^2 \tau_e h(b)}{2D(b)} \int \frac{d\vec{q}}{q^2} . \tag{7.46}$$

The change in the weak anti-localization correction $\frac{v_F^2 \tau_e h(b)}{2D(b)}$ arising from the hexagonal warping can be computed, and we found it to be constant equal to 1 and independent of b. This shows the independence of the weak anti-localization correction with respect to the value of the diffusion constant, as expected from the previous derivation for pure Dirac fermions since we have not changed the symmetries preserved by disorder and thus stayed in the same universality classes of the Anderson problem.

7.4.2 Universal conductance fluctutations

We have just checked in the previous section that the introduction of the hexagonal warping preserves the time-reversal symmetry, and thus that we stay in the symplectic class. Moreover, we have determined the diffusion constant

non perturbatively in the warping parameter b in Eq. (7.38). We can introduce, as in the Sec. 6.3 the phase coherence length $L_\phi = \sqrt{D(b)\tau_\phi(T)}$ and thermal length $L_T = \sqrt{\hbar D(b)/T}$ that now depend on b. The results derived in the case of pure Dirac fermions still hold, with these renormalized lengths. We obtain in the universal regime $L \ll L_\phi, L_T$, the same value for the universal conductance fluctuations :

$$\langle \delta\sigma^2 \rangle = \frac{12}{\pi^4} \left(\frac{e^2}{h}\right)^2 \sum_{n_x=1}^{\infty} \sum_{n_y=0}^{\infty} \frac{1}{(n_x^2+n_y^2)^2} \simeq 0.185613 \left(\frac{e^2}{h}\right)^2. \tag{7.47}$$

In the other regimes, the value of the fluctuations are not universal as they depend on the diffusion coefficient, and we obtain again :

$$\begin{aligned}
\langle \delta\sigma^2 \rangle &\simeq \frac{3}{\pi} \left(\frac{e^2}{h}\right)^2 \left(\frac{L_\phi}{L}\right)^2 \text{ for } L_\phi \ll L, L_T, & (7.48)\\
&\simeq \frac{2}{3} \left(\frac{L_T}{L}\right)^2 \left(\frac{e^2}{h}\right)^2 \ln\left(\frac{L}{L_T}\right) \text{ for } L_T \ll L \ll L_\phi, & (7.49)\\
&\simeq \frac{2}{3} \left(\frac{L_T}{L}\right)^2 \left(\frac{e^2}{h}\right)^2 \ln\left(\frac{L_\phi}{L_T}\right) \text{ for } L_T \ll L_\phi \ll L. & (7.50)
\end{aligned}$$

7.5 Evolution of the diffusion coefficient

7.5.1 WAL correction

The length L_ϕ is defined through the diffusion coefficient, which is now a function of the warping parameter b, and we have seen that the increase of the diffusion coefficient when the warping is increased is dramatic. This means that it is possible, for a given sample with fixed Hamiltonian parameters λ and v_F to modify the value of the diffusion coefficient by changing the Fermi energy as we can see in Fig7.8 where we plotted the evolution of D, and the corresponding conductivity, as a function of the Fermi energy, for a range of energy in the gap of the topological insulator.

This increase of the diffusion coefficient will be responsible for an increase of the classical conductivity with the Fermi energy, but also for an increase of the coherence length $L_\phi = \sqrt{D(b)\tau_\phi(T)}$ and thermal length $L_T = \sqrt{\hbar D(b)/T}$ that appear when studying the amplitude of the conductance fluctuations when not in the universal regime :

$$\begin{aligned}
\langle \delta\sigma^2 \rangle &\simeq \frac{3}{\pi} \left(\frac{e^2}{h}\right)^2 \left(\frac{L_\phi}{L}\right)^2 \text{ for } L_\phi \ll L, L_T, & (7.51)\\
&\simeq \left(\frac{L_T}{L}\right)^2 \left(\frac{e^2}{h}\right)^2 \ln\left(\frac{L}{L_T}\right) \text{ for } L_T \ll L \ll L_\phi, & (7.52)\\
&\simeq \left(\frac{L_T}{L}\right)^2 \left(\frac{e^2}{h}\right)^2 \ln\left(\frac{L_\phi}{L_T}\right) \text{ for } L_T \ll L_\phi \ll L. & (7.53)
\end{aligned}$$

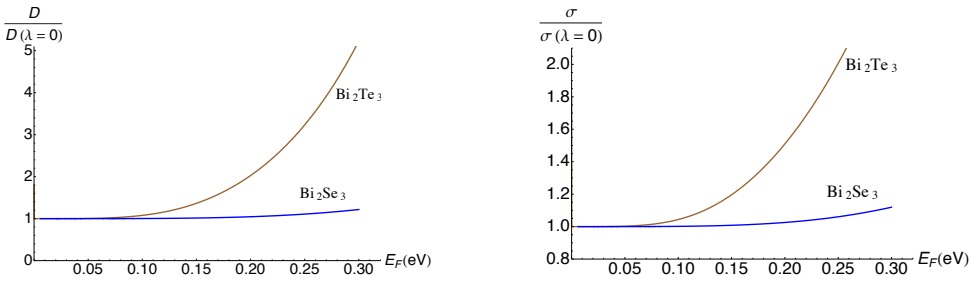

Figure 7.8: Left : Profile of the diffusion constant as a function of the Fermi energy in Bi_2Te_3 and Bi_2Se_3. Right : Evolution of the conductance with the Fermi energy. The parameters v_F and λ have been derived from ARPES experiments as $\lambda = 128$ eV.[3] and $v_F = 3.55$ eV. in Bi_2Se_3 whereas $\lambda = 250$ eV.[3] and $v_F = 2.55$ eV. in Bi_2Te_3 and both the diffusion constant and the conductivity have been normalized with respect to their value in the absence of hexagonal warping $\lambda = 0$.

Since these two lengths are defined as a function of the diffusion coefficient whereas the size of the sample L is fixed, we should observe a variation of the amplitude of the fluctuations when the Fermi energy is changed.

7.5.2 Critical magnetic field

In the magnetoconductance experiments where a transverse magnetic field is applied to the sample in order to change the symmetry class from symplectic to unitary, we observe the suppression of the cooperon as the suppression of the weak anti-localization correction. This crossover is described by :

$$\langle \Delta\sigma(B) \rangle = \frac{e^2}{2\pi^2\hbar} \left[\Psi(\frac{1}{2} - \frac{B_e}{B}) - \Psi(\frac{1}{2} - \frac{B_\phi}{B}) \right] . \tag{7.54}$$

where Ψ is the Digamma function and the characteristic fields $B_X = \hbar/(4eD\tau_X)$. The characteristic field to observe this suppression is B_ϕ and the dependance of this field on the diffusion coefficient can be observed by repeating the experiments with different Fermi energies (cf Fig.7.9).

Similarly, the conductance fluctuations are divided by a factor of 2 when the magnetic field is increased, with a crossover :

$$\langle \delta\sigma(B)^2 \rangle = \frac{1}{2} \langle \delta\sigma^2 \rangle \left[1 + \frac{B_\phi}{B} \Psi'(\frac{1}{2} + \frac{B_\phi}{B}) \right] . \tag{7.55}$$

and this division is observed with the same characteristic field, so the profile of the crossover will be different for different Fermi energies.

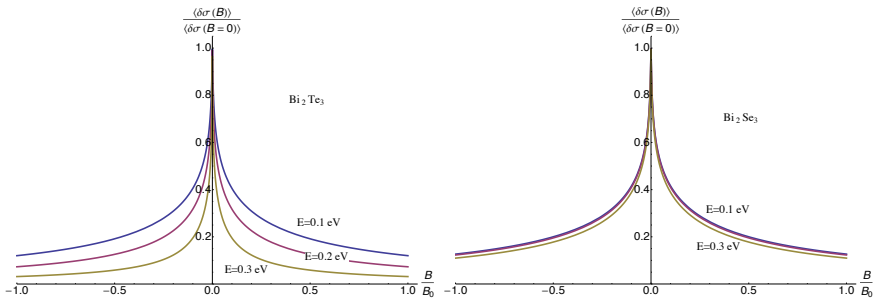

Figure 7.9: Dependence of the weak localization correction $\langle\delta\sigma(B)\rangle/\langle\delta\sigma(B=0)\rangle$ on the Fermi energy for the values of λ and v_F corresponding to the Bi_2Te_3 (Left) and Bi_2Se_3 (Right) compounds. We have chosen to scale the magnetic field as B/B_0 where $B_0 l_e^2 = \Phi_0 = h/e$ to avoid any energy (or warping) dependence of this rescaling field. The results show a clear dependence on energy of the magnetic field characteristic of weak localization decay.

7.6 In plane magnetic field

In opposition to graphene, the spin entering in the Hamiltonian of topological insulators is the real spin, which means that a magnetic field is a powerful tool at the disposition of experimentalists to know better about the properties of such surface states.

For example, we consider the effect of an in plane Zeeman magnetic field on the transport properties of the surface states. This magnetic field adds a new term to the Hamiltonian in Eq. (7.2) :

$$\mathcal{H}_Z = g\mu_B(\sigma^x B_x + \sigma^y B_y). \tag{7.56}$$

In the absence of warping, the total Hamiltonian reads :

$$\mathcal{H} = (\hbar v_F \vec{k} + g\mu_B \vec{B}).\vec{\sigma}. \tag{7.57}$$

This expression shows the Zeeman field acts as a constant vector potential and can be gauged away : we can shift uniformly the momenta by the quantity $g\mu_B\vec{B}/\hbar v_F$ and we obtain the pure Dirac Hamiltonian of Eq. (5.2). As a consequence, this magnetic field should not modify the scattering probability $g(\vec{k},\vec{k'})$.

However, in presence of the hexagonal warping, this shift is not possible anymore, and the introduction of the magnetic field deforms the Fermi surface (cf Fig. 7.10). As a consequence, we observe a dependance in B of the scattering amplitudes $g(\vec{k},\vec{k'})$ and thus a dependance of the conductivity is expected.

Moreover, if we perform the $g\mu_B\vec{B}/\hbar v_F$ shift in momentum, we observe that the Fermi surface is no longer time-reversal symmetric : opposite points

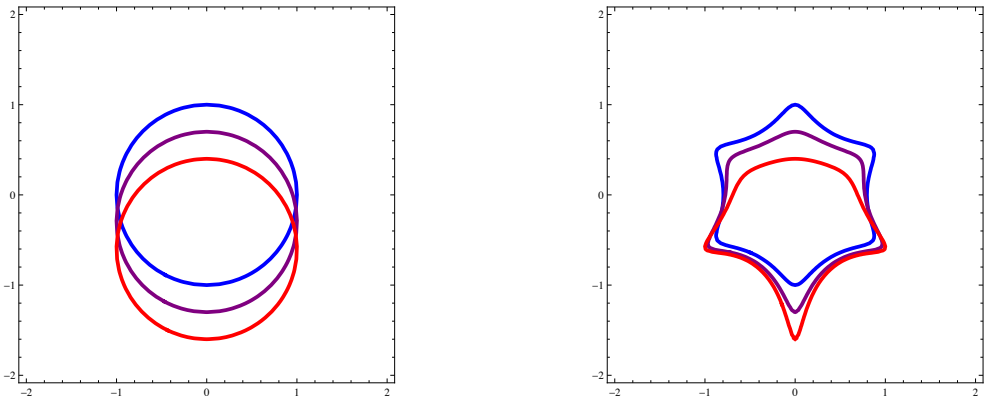

Figure 7.10: Evolution of the Fermi surface in absence of warping (left), and with hexagonal warping (right) as the magnetic field is increased in the y direction (from blue to red).

of the Fermi surface are not at the same distance from the center. We expect a crossover from the symplectic class in the absence of the Zeeman magnetic field to the unitary when time-reversal symmetry is broken.

To describe quantitatively this crossover, we introduce the magnetic field as a perturbation in the standard diagrammatic. The perturbative parameter is $\tilde{B} = g\mu_B B/E_F$. The crossover from the symplectic class to the unitary class corresponds to the suppression of the cooperon contribution as it is now described by the diffusion of a massive singlet. Indeed, to obtain the cooperon structure factor, we need to calculate the quantity $P^C(\vec{Q}) = \int_{\vec{k}} \langle G^A(\vec{Q}-\vec{k})\rangle \otimes \langle G^R(\vec{k})\rangle$. As $\Gamma^C = \gamma(Id\otimes Id - P^C)^{-1}$, we calculate the eigenvalues of the operator $Id\otimes Id - P^C$. In absence of the magnetic field, the smallest eigenvalue is $DQ^2\tau_e$, corresponding to the diffusive singlet state. However, in the presence of the magnetic field, this eigenvalue turns to $DQ^2\tau_e + M(b,\tilde{B})$ and this leads to a cooperon structure factor approximated by :

$$\Gamma^C(\vec{Q}) = \gamma \frac{1}{DQ^2\tau_e + M(b,\tilde{B})} \frac{1}{4} \left[Id\otimes Id - \sigma^x\otimes\sigma^x - \sigma^y\otimes\sigma^y - \sigma^z\otimes\sigma^z\right] . \tag{7.58}$$

It is this mass term $M(b,\tilde{B})$ which encodes the effect of the Zeeman magnetic field. We have already calculated this term in the absence of magnetic field in the study of the hexagonal warping in Eq. (6.4), $M(b,0) = 0$, and we expect this term to vanish in absence of the hexagonal warping, since it corresponds to a magnetic field that can be gauges away $M(0,\tilde{B}) = 0$. Perturbatively to the second order in $\tilde{B}$, this term can be written as $M(b,\tilde{B}) = m(b)\tilde{B}^2$, and we plotted in Fig. 7.11, the evolution of the parameter $m(b)$.

The expression $DQ^2\tau_e + M(b,\tilde{B})$ introduces naturally a length scale $L_B =$

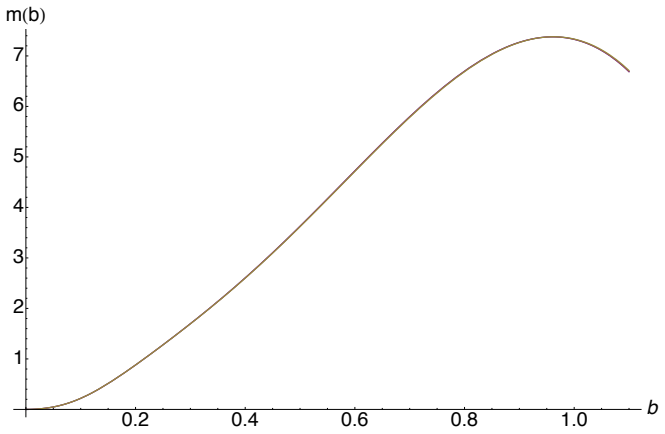

Figure 7.11: Evolution of the coefficient m(b) characterizing the mass term $M(b,\tilde{B}) = m(b)\tilde{B}^2$ due to the magnetic field.

$\sqrt{D\tau_e/M(b,\tilde{B})}$ quantifying the crossover from the symplectic to the unitary class. The length scale combines with the coherence length as

$$\tilde{L}^{-2} = L_\phi^{-2} + L_B^{-2}$$

to form the length scale on which the cooperon is suppressed , the relevant length to describe the weak anti localization and the conductance fluctuations. We obtain :

$$\begin{aligned}
\langle \Delta\sigma(\vec{B})\rangle &= \left(\frac{e^2}{\pi\hbar}\right)\int_{\vec{Q}} \frac{1}{Q^2 + L_B^{-2} + L_\phi^{-2}} = f(\tilde{L}/l_e, L/\tilde{L}) \,, && (7.59)\\
\langle \delta\sigma^2(\vec{B})\rangle &= 6\left(\frac{e^2}{h}\right)^2 \frac{1}{V}\left[\int_{\vec{q}} \frac{1}{(q^2 + L_\phi^{-2})^2} + \int_{\vec{q}} \frac{1}{(q^2 + L_B^{-2} + L_\phi^{-2})^2}\right]\\
&= \frac{1}{2}\langle \delta\sigma^2(\vec{B})\rangle + f_2(L/\tilde{L}) \,. && (7.60)
\end{aligned}$$

The functions f and f_2 depend on the geometry of the sample. In the case of an infinite 2 dimensional sample, we obtain from Eq. (7.59) the logarithmic dependance of f in $\tilde{L}/l_e$ seen in Eq. (6.14) :

$$\langle \Delta\sigma(\vec{B})\rangle = \frac{e^2}{2\pi^2\hbar} \ln\left(\frac{\tilde{L}}{l_e}\right) \,. \qquad (7.61)$$

For different geometries, we need to do the proper summation over all the available momenta, depending on the boundary conditions to obtain the function f and f_2.

We can check that in the absence of the magnetic field, the mass term vanishes and the magnetic length associated L_B becomes infinite. In this case, the relevant length for describing the cooperon is the coherence length $\tilde{L} = L_\phi$. The introduction of the magnetic field reduces the value of the length scale $\tilde{L}$, and we need to compare the sample size to this length, instead of the coherence length.

In order to determine the effects of this magnetic field, we need an order of magnitude of the magnetic length scale L_B, to check if it can be measured experimentally. This magnetic length scale can be expressed as a function of the parameters of the Hamiltonian as follows :

$$\frac{L_B}{l_e} = \frac{\sqrt{D(b)/(D(b=0)m(b))}}{\tilde{B}} = \frac{c(b)}{\tilde{B}}. \tag{7.62}$$

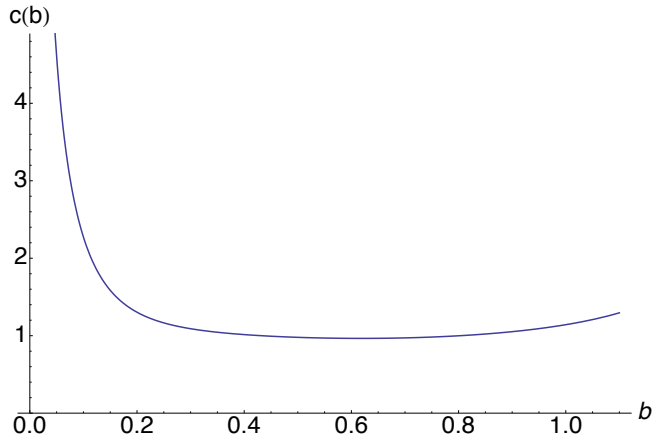

Figure 7.12: Evolution of the coefficient c relating the magnetic length to the elastic scattering length, as a function of the warping parameter.

We have plotted in Fig. 7.12 the evolution of the coefficient c as a function of the warping parameter b. In the Fig. 7.13, we plotted the value of this length normalized to the elastic scattering length with parameters relevant to Bi_2Se_3 and Bi_2Te_3, for a magnetic field of 1 T. This plot shows that we should expect a magnetic length around 1000 l_e, which which means this effect could be measured experimentally.

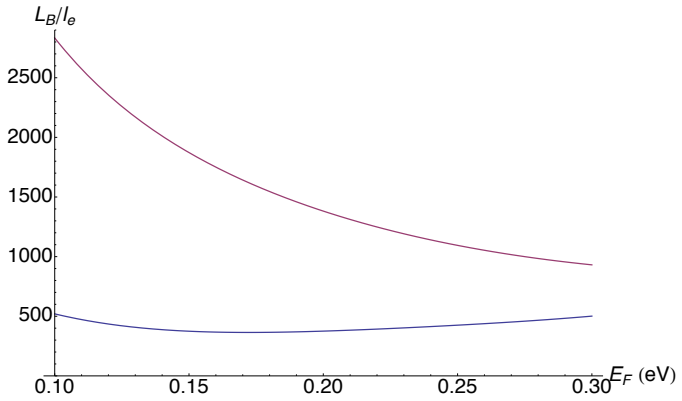

Figure 7.13: dependance of the magnetic dephasing length L_B on the Fermi energy for Bi_2Te_3 (red, $\lambda = 250$ eV.^{3} and $v_F = 2.55$ eV.) and Bi_2Se_3 (blue, $\lambda = 128$ eV.^{3} and $v_F = 3.55$ eV.).

Chapter 8

Conclusions

The aim of this thesis was to study the electronic transport properties of new phases of the matter, the topological insulators.

In a first time, we focused on the quantum spin Hall effect that was just realized experimentally. The main idea was to use the helical edge states of this phase, in combination with the Cooper pairs in a superconductor, to form perfect Cooper pair splitter. In theory, a perfectly clean interface between a normal metal and a superconductor should also realize this perfect Cooper pair splitting but any defect at the interface could absorb momentum during the tunneling process and leaves Cooper pairs unsplitted. We have shown that this no longer the case in a QSH/SC junction, as the total spin of a Cooper pair is conserved during the tunneling. As a consequence, because of the helicity of the QSH edge states, it is necessary that the two electrons forming the Cooper pairs go in opposite directions. We have also stressed the relation between Cooper pair injection and Andreev reflection, and showed that a QSH/SC junction is equivalent to a beam-splitter where reflected electrons are turned into holes, which leads to perfect Andreev reflection in the regime of long superconducting regions. In the case of long superconducting region in a QSH/SC/QSH junction, we also showed this perfect Andreev reflection, with the precaution that the Andreev reflection is only a convenient picture to describe effectively the scattering and that we must remember that the reflection does not occur at the interfaces but on the whole superconducting length.

Secondly, we turned to 3 dimensional topological insulators, where disorder plays a stronger role than in 2 dimensional topological insulators : the edge states of QSH are ballistic, since the time-reversal symmetry prevents backscattering. In the case of 3DTI surface states, the backscattering is also suppressed, but the Fermi surface is a circle, and not reduced to two points. This means that any impurity can scatter the surface states in any direction, and that the propagation of the surface states is diffusive. We focused in the mesoscopic physics regime of coherent transport, where the surface states keep

memory of their phase along the diffusion, allowing for interference effects. In this regime, we studied the diffusion of Dirac fermions, the simplest model to characterize the 3DTI surface states. We also derived the quantum interferences responsible for weak anti-localization correction and the amplitude of the universal conductance fluctuations. This derivation showed that the only relevant parameters to describe these effects are the diffusion constant and the time-reversal symmetry of the hamiltonian (in the case of metals). Finally, we also studied a feature distinguishing the 3DTI surface states from other Dirac fermions (e.g. in graphene) : the hexagonal warping deforming the Fermi surface from a circle into a hexagon or a snow-flake when the Fermi energy is increased. This hexagonal warping preserves the symmetry of the hamiltonian but changes the value of the diffusion constant. As a consequence, we predict that the value of the characteristic magnetic field for weak anti-localization correction or the amplitude of the universal conductance fluctuations should be dependent in the Fermi energy. We also predict a magnetoconductance when the magnetic field is in the plane of the diffusion only in presence of this hexagonal warping.

Bibliography

[1] P. W. Anderson. *Basic Notions of Condensed Matter Physics*, volume 55 of *Frontiers in Physics*. Addison-Wesley, Reading, MA, 1983.

[2] K. Klitzing, G. Dorda, and M. Pepper. New Method for High-Accuracy Determination of the Fine-Structure Constant Based on Quantized Hall Resistance. *Physical Review Letters*, 45(6):494–497, 1980.

[3] D. Thouless, M. Kohmoto, M.P. Nightingale, and M. den Nijs. Quantized Hall Conductance in a Two-Dimensional Periodic Potential. *Physical Review Letters*, 49(6):405–408, 1982.

[4] Yasuhiro Hatsugai. Chern number and edge states in the integer quantum Hall effect. *Phys. Rev. Lett.*, 71:3697–3700, Nov 1993.

[5] C. Kane and E.J. Mele. Quantum Spin Hall Effect in Graphene. *Physical Review Letters*, 95(22), 2005.

[6] A. K. Geim and K. S. Novoselov. The rise of graphene. *Nature Materials*, 6(3):183–191, 03 2007.

[7] B. Andrei Bernevig, Taylor L. Hughes, and Shou-Cheng Zhang. Quantum Spin Hall Effect and Topological Phase Transition in HgTe Quantum Wells. *Science*, 314(5806):1757–1761, 2006.

[8] L. Fu, C. Kane, and E.J. Mele. Topological insulators in three dimensions. *Physical Review Letters*, 98(10), 2007.

[9] J. E. Moore and L. Balents. Topological invariants of time-reversal-invariant band structures. *Phys. Rev. B*, 75(12):121306, March 2007.

[10] Rahul Roy. Topological phases and the quantum spin Hall effect in three dimensions. *Phys. Rev. B*, 79:195322, May 2009.

[11] Haijun Zhang, Chao-Xing Liu, Xiao-Liang Qi, Xi Dai, Zhong Fang, and Shou-Cheng Zhang. Topological insulators in Bi_2Se_3, Bi_2Te_3 and Sb_2Te_3 with a single Dirac cone on the surface. *Nat Phys*, 5(6):438–442, 06 2009.

[12] Markus Konig, Steffen Wiedmann, Christoph Brune, Andreas Roth, Hartmut Buhmann, Laurens W. Molenkamp, Xiao-Liang Qi, and Shou-Cheng Zhang. Quantum Spin Hall Insulator State in HgTe Quantum Wells. *Science*, 318(5851):766, 2007.

[13] D. Hsieh, D. Qian, L. Wray, Y. Xia, Y. S. Hor, R. J. Cava, and M. Z. Hasan. A topological Dirac insulator in a quantum spin Hall phase. *Nature*, 452(7190):970–974, 04 2008.

[14] A. A. Taskin and Yoichi Ando. Quantum oscillations in a topological insulator $Bi_{1-x}Sb_x$. *Phys. Rev. B*, 80:085303, Aug 2009.

[15] Z. Alpichshev, J.G. Analytis, J.-H. Chu, I. R. Fisher, Y. L. Chen, Z. X. Shen, A. Fang, and A. Kapitulnik. STM Imaging of Electronic Waves on the Surface of Bi_2Te_3: Topologically Protected Surface States and Hexagonal Warping Effects. *Phys. Rev. Lett.*, 104:016401, 2010.

[16] C. Bouvier, T. Meunier, P. Ballet, X. Baudry, R. Kramer, and Laurent Levy. Strained HgTe: a textbook 3d topological insulator. arXiv:1112.2092, 2011.

[17] C. Wu, B. A. Bernevig, and S.-C. Zhang. Helical Liquid and the Edge of Quantum Spin Hall Systems. *Phys. Rev. Lett.*, 96(10):106401, March 2006.

[18] Ion Garate and M. Franz. Inverse spin-galvanic effect in the interface between a topological insulator and a ferromagnet. *Phys. Rev. Lett.*, 104:146802, Apr 2010.

[19] Y. S. Hor, A. J. Williams, J. G. Checkelsky, P. Roushan, J. Seo, Q. Xu, H. W. Zandbergen, A. Yazdani, N. P. Ong, and R. J. Cava. Superconductivity in $Cu_xBi_2Se_3$ and its Implications for Pairing in the Undoped Topological Insulator. *Phys. Rev. Lett.*, 104:057001, 2010.

[20] Andreas P. Schnyder, Shinsei Ryu, Akira Furusaki, and Andreas W. W. Ludwig. Classification of topological insulators and superconductors in three spatial dimensions. *Phys. Rev. B*, 78:195125, 2008.

[21] A. P. Schnyder, S. Ryu, A. Furusaki, and A. W. W. Ludwig. Classification of topological insulators and superconductors. *AIP Conf. Proc.*, 10:1134, 2009.

[22] Liang Fu and C. L. Kane. Superconducting Proximity Effect and Majorana Fermions at the Surface of a Topological Insulator. *Phys. Rev. Lett.*, 100:096407, Mar 2008.

[23] A. R. Akhmerov, Johan Nilsson, and C. W. J. Beenakker. Electrically Detected Interferometry of Majorana Fermions in a Topological Insulator. *Phys. Rev. Lett.*, 102:216404, May 2009.

[24] E. Majorana. Teoria simmetrica dell'elettrone e del positrone. *Nuovo Cimento*, 14, 1937.

[25] Jason Alicea, Yuval Oreg, Gil Refael, Felix von Oppen, and Matthew P. A. Fisher. Non-Abelian statistics and topological quantum information processing in 1D wire networks. *Nat Phys*, 7(5):412–417, 05 2011.

[26] F. Wilczek. Two applications of axion electrodynamics. *Phys. Rev. Lett.*, 58:1799–1802, 1987.

[27] A. Yu. Kitaev. Fault-tolerant quantum computation by anyons. *Annals of Physics*, 303(1):2–30, 1 2003.

[28] G. P. Collins. Computing with quantum knots. *Sci. Am.*, 294:57–63, 2006.

[29] J. Nilsson, A. R. Akhmerov, and C. W. J. Beenakker. Splitting of a Cooper Pair by a Pair of Majorana Bound States. *Phys. Rev. Lett.*, 101(12):120403, September 2008.

[30] V. Mourik, K. Zuo, S. M. Frolov, S. R. Plissard, E. P. A. M. Bakkers, and L. P. Kouwenhoven. Signatures of Majorana Fermions in Hybrid Superconductor-Semiconductor Nanowire Devices. *Science*, 336(6084):1003–1007, 2012.

[31] N.W. Aschcroft and N.D. Mermin. *Solid state physics*. Saunders college publishing, 1976.

[32] E. Akkermans and G. Montambaux. *Mesoscopic Physics of Electrons and Photons*. Cambridge University Press, 2007.

[33] Liang Fu and C. L. Kane. Time reversal polarization and a Z_2 adiabatic spin pump. *Phys. Rev. B*, 74:195312, Nov 2006.

[34] B. I. Halperin. Quantized Hall conductance, current-carrying edge states, and the existence of extended states in a two-dimensional disordered potential. *Phys. Rev. B*, 25:2185, February 1982.

[35] R. B. Laughlin. Quantized Hall conductivity in two dimensions. *Phys. Rev. B*, 23(10):5632, May 1981.

[36] M. Kohmoto. Topological Invariant and the Quantization of the Hall conductance. *Annals of Physics*, 160:343–354, 1985.

[37] J. E. Avron, R. Seiler, and B. Simon. Homotopy and Quantization in Condensed Matter Physics. *Phys. Rev. B*, 51(1):51, Jul 1983.

[38] Joseph E. Avron and Ruedi Seiler. Quantization of the Hall Conductance for General, Multiparticle Schrödinger Hamiltonians. *Phys. Rev. Lett.*, 54(4):259, Jan 1985.

[39] Shiing-shen Chern. Characteristic Classes of Hermitian Manifolds. *Annals of Mathematics*, 47(1):85–121, 01 1946.

[40] C. Kane and E.J. Mele. Z_2 Topological Order and the Quantum Spin Hall Effect. *Physical Review Letters*, 95(14):146802, 2005.

[41] J. T. Chalker and S. L. Sondhi. Transverse magnetoresistance of the two-dimensional chiral metal. *Phys. Rev. B*, 59:4999–5002, Feb 1999.

[42] M. Z. Hasan and C. L. Kane. *Colloquium* : Topological insulators. *Rev. Mod. Phys.*, 82:3045–3067, Nov 2010.

[43] Xiao-Liang Qi and Shou-Cheng Zhang. Topological insulators and superconductors. *Rev. Mod. Phys.*, 83:1057, 2011.

[44] F. Laloë C. Cohen-Tannoudji, B. Diu. *Mécanique quantique*. Hermann, 1997.

[45] R. Leturcq. Lecture in GDR Physique mésoscopique summer school in Cargèse, 09 2012.

[46] B. Bernevig and S. C. Zhang. Quantum Spin Hall Effect. *Physical Review Letters*, 96(10), 2006.

[47] C. Day. Quantum Spin Hall Effect Shows up in a Quantum Well Insulator, Just as Predicted. *Physics Today*, 61(1):010000, 2008.

[48] Andreas Roth, Christoph Brüne, Hartmut Buhmann, Laurens W. Molenkamp, Joseph Maciejko, Xiao-Liang Qi, and Shou-Cheng Zhang. Nonlocal Transport in the Quantum Spin Hall State. *Science*, 325(5938):294–297, 2009.

[49] Xiao-Yong Feng, Wei-Qiang Chen, Jin-Hua Gao, Qiang-Hua Wang, and Fu-Chun Zhang. Anderson impurity in a helical metal. *Phys. Rev. B*, 81:235411, Jun 2010.

[50] J. Gao, W. Chen, X. C. Xie, and F.-C. Zhang. In-plane noncollinear exchange coupling mediated by helical edge states in quantum spin Hall systems. *Phys. Rev. B*, 80(24):241302, December 2009.

[51] Liang Fu and C. L. Kane. Topological insulators with inversion symmetry. *Phys. Rev. B*, 76:045302, Jul 2007.

[52] H.-J. Zhang, C.-X. Liu, X.-L. Qi, X.-Y. Deng, X. Dai, S.-C. Zhang, and Z. Fang. Electronic structures and surface states of the topological insulator $Bi_{1-x}Sb_x$. *Physical Review B*, 80(8), 2009.

[53] Oleg V. Yazyev, Joel E. Moore, and Steven G. Louie. Spin polarization and transport of surface states in the topological insulators Bi_2Se_3 and Bi_2Te_3 from first principles. *Phys. Rev. Lett.*, 105:266806, 2010.

[54] D. Hsieh, Y. Xia, L. Wray, D. Qian, A. Pal, J. H. Dil, J. Osterwalder, F. Meier, G. Bihlmayer, C. L. Kane, Y. S. Hor, R. J. Cava, and M. Z. Hasan. Observation of unconventional quantum spin textures in topological insulators. *Science*, 323:919–922, 2009.

[55] Wonsig Jung, Yeongkwan Kim, Beomyoung Kim, Yoonyoung Koh, Chul Kim, Masaharu Matsunami, Shin-ichi Kimura, Masashi Arita, Kenya Shimada, Jung Hoon Han, Juyoung Kim, Beongki Cho, and Changyoung Kim. Warping effects in the band and angular-momentum structures of the topological insulator Bi_2Te_3. *Phys. Rev. B*, 84:245435, Dec 2011.

[56] S. Souma, K. Kosaka, T. Sato, M. Komatsu, A. Takayama T. Takahashi, M. Kriener, Kouji Segawa, and Yoichi Ando. Direct Measurement of the Out-of-Plane Spin Texture in the Dirac-Cone Surface State of a Topological Insulator. *Phys. Rev. Lett.*, 106:216803, 2011.

[57] Y. H. Wang, D. Hsieh, D. Pilon, L. Fu, D. R. Gardner, Y. S. Lee, and N. Gedik. Observation of a warped helical spin texture in Bi_2Se_3 from circular dichroism angle-resolved photoemission spectroscopy. *Phys. Rev. Lett.*, 107:207602, 2011.

[58] Y. Xia, D. Qian, D. Hsieh, L. Wray, A. Pal, H. Lin, A. Bansil, D. Grauer, Y. S. Hor, R. J. Cava, and M. Z. Hasan. Observation of a large-gap topological-insulator class with a single Dirac cone on the surface. *Nat Phys*, 5(6):398–402, 06 2009.

[59] D. Hsieh, Y. Xia, D. Qian, L. Wray, J. H. Dil, F. Meier, J. Osterwalder, L. Patthey, J. G. Checkelsky, N. P. Ong, A. V. Fedorov, H. Lin, A. Bansil, D. Grauer, Y. S. Hor, R. J. Cava, and M. Z. Hasan. A tunable topological insulator in the spin helical Dirac transport regime. *Nature*, 460(7259):1101–1105, 08 2009.

[60] Z. Alpichshev, J. G. Analytis, J.-H. Chu, I. R. Fisher, and A. Kapitulnik. STM imaging of a bound state along a step on the surface of the topological insulator Bi_2Te_3. *Phys. Rev. B*, 84:041104, 2011.

[61] Y. L. Chen, J. G. Analytis, J.-H. Chu, Z. K. Liu, S.-K. Mo, X. L. Qi, H. J. Zhang, D. H. Lu, X. Dai, Z. Fang, S. C. Zhang, I. R. Fisher, Z. Hussain, and Z.-X. Shen. Experimental realization of a three-dimensional topological insulator, Bi_2Te_3. *Science*, 325:178–181, 2009.

[62] M. I. Katsnelson, K. S. Novoselov, and A. K. Geim. Chiral tunnelling and the Klein paradox in graphene. *Nat Phys*, 2(9):620–625, 09 2006.

[63] J. Seo, P. Roushan, H. Beidenkopf, Y. S. Hor, R. J. Cava, and A. Yazdani. Transmission of topological surface states through surface barriers. *Nature*, 466:343–346, 2010.

[64] L. Fu. Hexagonal Warping Effects in the Surface States of the Topological Insulator Bi_2Te_3. *Phys. Rev. Lett.*, 103(26), 2009.

[65] J. Analytis, J. Chu, Y. Chen, F. Corredor, R. McDonald, Z. Shen, and I. Fisher. Bulk Fermi surface coexistence with Dirac surface state in Bi_2Se_3: A comparison of photoemission and Shubnikov–de Haas measurements. *Phys. Rev. B*, 81:205407, 2010.

[66] Yong-qing Li, Ke-hui Wu, Jun-ren Shi, and Xin-cheng Xie. Electron transport properties of three-dimensional topological insulators. *Front. Phys.*, 7(2):165–174, 2012.

[67] N. Butch, K. Kirshenbaum, P. Syers, A. Sushkov, G. Jenkins, H. Drew, and J. Paglione. Strong surface scattering in ultrahigh-mobility Bi_2Se_3 topological insulator crystals. *Phys. Rev. B*, 81:241301(R), 2010.

[68] K. Eto, Z. Ren, A. Taskin, K. Segawa, and Y. Ando. Angular-dependent oscillations of the magnetoresistance in Bi_2Se_3 due to the three-dimensional bulk Fermi surface. *Phys. Rev. B*, 81:195309, 2010.

[69] Zhi Ren, A. A. Taskin, Satoshi Sasaki, Kouji Segawa, and Yoichi Ando. Large bulk resistivity and surface quantum oscillations in the topological insulator Bi_2Te_2Se. *Phys. Rev. B*, 82:241306, Dec 2010.

[70] J. G. Checkelsky, Y. S. Hor, R. J. Cava, and N. P. Ong. Bulk band gap and surface state conduction observed in voltage-tuned crystals of the topological insulator Bi_2Se_3. *Phys. Rev. Lett.*, 106:196801, 2011.

[71] Guanhua Zhang, Huajun Qin, Jing Teng, Jiandong Guo, Qinlin Guo, Xi Dai, Zhong Fang, and Kehui Wu. Quintuple-layer epitaxy of thin films of topological insulator Bi_2Se_3. *Applied Physics Letters*, 95(5):053114, 2009.

[72] Hong-Tao He, Gan Wang, Tao Zhang, Iam-Keong Sou, George K. L Wong, Jian-Nong Wang, Hai-Zhou Lu, Shun-Qing Shen, and Fu-Chun Zhang. Impurity effect on weak antilocalization in the topological insulator Bi_2Te_3. *Phys. Rev. Lett.*, 106:166805, 2011.

[73] Yi Zhang, Ke He, Cui-Zu Chang, Can-Li Song, Li-Li Wang, Xi Chen, Jin-Feng Jia, Zhong Fang, Xi Dai, Wen-Yu Shan, Shun-Qing Shen, Qian Niu, Xiao-Liang Qi, Shou-Cheng Zhang, Xu-Cun Ma, and Qi-Kun Xue.

Crossover of the three-dimensional topological insulator Bi_2Se_3 to the two-dimensional limit. *Nat Phys*, 6(8):584–588, 08 2010.

[74] Yi Zhang, Cui-Zu Chang, Ke He, Li-Li Wang, Xi Chen, Jin-Feng Jia, Xu-Cun Ma, and Qi-Kun Xue. Doping effects of Sb and Pb in epitaxial topological insulator Bi_2Se_3 thin films: An in situ angle-resolved photoemission spectroscopy study. *Applied Physics Letters*, 97(19):194102, 2010.

[75] J. Chen, H. J. Qin, F. Yang, J. Liu, T. Guan, F. M. Qu, G. H. Zhang, J. R. Shi, X. C. Xie, C. L. Yang, K. H. Wu, Y. Q. Li, and L. Lu. Gate-Voltage Control of Chemical Potential and Weak Antilocalization in Bi_2Se_3. *Phys. Rev. Lett.*, 105:176602, Oct 2010.

[76] H D Li, Z Y Wang, X Kan, X Guo, H T He, Z Wang, J N Wang, T L Wong, N Wang, and M H Xie. The van der Waals epitaxy of Bi_2Se_3 on the vicinal Si(111) surface: an approach for preparing high-quality thin films of a topological insulator. *New Journal of Physics*, 12(10):103038, 2010.

[77] H. D. Li, Z. Y. Wang, X. Guo, Tai Lun Wong, Ning Wang, and M. H. Xie. Growth of multilayers of Bi_2Se_3/ZnSe: Heteroepitaxial interface formation and strain. *Applied Physics Letters*, 98(4):043104, 2011.

[78] Yao-Yi Li, Guang Wang, Xie-Gang Zhu, Min-Hao Liu, Cun Ye, Xi Chen, Ya-Yu Wang, Ke He, Li-Li Wang, Xu-Cun Ma, Hai-Jun Zhang, Xi Dai, Zhong Fang, Xin-Cheng Xie, Ying Liu, Xiao-Liang Qi, Jin-Feng Jia, Shou-Cheng Zhang, and Qi-Kun Xue. Intrinsic Topological Insulator Bi2Te3 Thin Films on Si and Their Thickness Limit. *Advanced Materials*, 22(36):4002–4007, 2010.

[79] Peng Cheng, Canli Song, Tong Zhang, Yanyi Zhang, Yilin Wang, Jin-Feng Jia, Jing Wang, Yayu Wang, Bang-Fen Zhu, Xi Chen, Xucun Ma, Ke He, Lili Wang, Xi Dai, Zhong Fang, Xincheng Xie, Xiao-Liang Qi, Chao-Xing Liu, Shou-Cheng Zhang, and Qi-Kun Xue. Landau Quantization of Topological Surface States in Bi_2Se_3. *Phys. Rev. Lett.*, 105:076801, Aug 2010.

[80] A. Richardella, D. M. Zhang, J. S. Lee, A. Koser, D. W. Rench, A. L. Yeats, B. B. Buckley, D. D. Awschalom, and N. Samarth. Coherent heteroepitaxy of Bi_2Se_3 on GaAs (111)B. *Applied Physics Letters*, 97(26):262104, 2010.

[81] D. Kim, S. Cho, N.P. Butch, P. Syers, K. Kirshenbaum, J. Paglione, and M.S. Fuhrer. Minimum conductivity and charge inhomogeneity in Bi_2Se_3 in the topological regime. arXiv:1105.1410, 2011.

[82] D. Kong, W. Dang, J.J. Cha, H. Li, S. Meister, H. Peng, Z. Liu, and Y. Cui. Few-layer nanoplates of Bi_2Se_3 and Bi_2Te_3 with highly tunable chemical potential. *Nano Lett.*, 10:2245, 2010.

[83] Can-Li Song, Yi-Lin Wang, Ye-Ping Jiang, Yi Zhang, Cui-Zu Chang, Lili Wang, Ke He, Xi Chen, Jin-Feng Jia, Yayu Wang, Zhong Fang, Xi Dai, Xin-Cheng Xie, Xiao-Liang Qi, Shou-Cheng Zhang, Qi-Kun Xue, and Xucun Ma. Topological insulator Bi_2Se_3 thin films grown on double-layer graphene by molecular beam epitaxy. *Applied Physics Letters*, 97(14):143118, 2010.

[84] Hailin Peng, Keji Lai, Desheng Kong, Stefan Meister, Yulin Chen, Xiao-Liang Qi, Shou-Cheng Zhang, Zhi-Xun Shen, and Yi Cui. Aharonov-Bohm interference in topological insulator nanoribbons. *Nat Mater*, 9(3):225–229, 03 2010.

[85] Rodolphe Guyon, Thierry Martin, and Gordey B. Lesovik. Tunable decoherence in the vicinity of a normal metal-superconducting junction. *Phys. Rev. B*, 64:035315, 2001.

[86] Leon N. Cooper. Bound Electron Pairs in a Degenerate Fermi Gas. *Phys. Rev.*, 104:1189–1190, Nov 1956.

[87] J. Bardeen, L. N. Cooper, and J. R. Schrieffer. Microscopic Theory of Superconductivity. *Phys. Rev.*, 106:162–164, Apr 1957.

[88] A. F. Andreev. Thermal conductivity of the intermediate state of superconductors. *Sov. Phys. JETP*, 19(1228), 1964.

[89] I. Affleck, J.-S. Caux, and A. M. Zagoskin. Andreev scattering and Josephson current in a one-dimensional electron liquid. *Phys. Rev. B*, 62:1433, July 2000.

[90] A. Altland and M.R. Zirnbauer. Nonstandard symmetry classes in mesoscopic normal-superconducting hybrid structures. *Phys. Rev. B*, 55:1142, 1997.

[91] I. Knez, R.-R. Du, and G. Sullivan. Andreev Reflection of Helical Edge Modes in InAs/GaSb Quantum Spin Hall Insulator. *Physical Review Letters*, 109(18):186603, 2012.

[92] D. Culcer, E.H. Hwang, T.D. Stanescu, and S. Das Sarma. Two-dimensional surface charge transport in topological insulators. *Phys. Rev. B*, 82:155457, 2010.

[93] K. S. Novoselov, A. K. Geim, S. V. Morozov, D. Jiang, Y. Zhang, S. V. Dubonos, I. V. Grigorieva, and A. A. Firsov. Electric field effect in atomically thin carbon films. *Science*, 306(5696):666–669, 2004.

[94] A. H. Neto, F. Guinea, N. M. Peres, K. S. Novoselov, and A. K. Geim. The electronic properties of graphene. *Rev. Mod. Phys.*, 81:109–163, 2009.

[95] E. McCann, K. Kechedzhi, V.I. Fal'ko, H. Suzuura, T. Ando, and B.L. Altshuler. Weak-localization magnetoresistance and valley symmetry in graphene. *Phys. Rev. Lett.*, 97:146805, 2006.

[96] M.Yu. Kharitonov and K.B. Efetov. Universal conductance fluctuations in graphene. *Phys. Rev. B*, 78:033404, 2008.

[97] Kentaro Nomura, Mikito Koshino, and Shinsei Ryu. Topological Delocalization of Two-Dimensional Massless Dirac Fermions. *Phys. Rev. Lett.*, 99:146806, 2007.

[98] Su-Yang Xu, L. A. Wray, Y. Xia, F. von Rohr, Y. S. Hor, J. H. Dil, F. Meier, B. Slomski, J. Osterwalder, M. Neupane, H. Lin, A. Bansil, A. Fedorov, R. J. Cava, and M. Z. Hasan. Realization of an isolated Dirac node and strongly modulated Spin Texture in the topological insulator Bi_2Te_3. arXiv:1101.3985, 2011.

[99] Shinobu Hikami, Anatoly I. Larkin, and Yosuke Nagaoka. Spin-Orbit Interaction and Magnetoresistance in the Two Dimensional Random System. *Progress of Theoretical Physics*, 63(2):707–710, 1980.

[100] F. Evers and A. D. Mirlin. Anderson transitions. *Rev. Mod. Phys.*, 80:1355, 2008.

[101] Chao-Xing Liu, Xiao-Liang Qi, HaiJun Zhang, Xi Dai, Zhong Fang, and Shou-Cheng Zhang. Model hamiltonian for topological insulators. *Phys. Rev. B*, 82:045122, 2010.

[102] K. Kuroda, M. Arita, K. Miyamoto, M. Ye, J. Jiang, A. Kimura, E. E. Krasovskii, E. V. Chulkov, H. Iwasawa, T. Okuda, K. Shimada, Y. Ueda, H. Namatame, and M. Taniguchi. Hexagonally Deformed Fermi Surface of the 3D Topological Insulator Bi_2Se_3. *Phys. Rev. Lett.*, 105:076802, 2010.

[103] T. Hirahara, Y. Sakamoto, Y. Takeichi, H. Miyazaki, S-I Kimura, I. Matsuda, A. Kakizaki, and S. Hasegawa. Anomalous transport in an n-type topological insulator ultrathin Bi_2Se_3 film. *Phys. Rev. B*, 82:155309, 2010.

[104] G. Tkachov and E. M. Hankiewicz. Weak antilocalization in HgTe quantum wells and topological surface states: Massive versus massless Dirac fermions. *Phys. Rev. B*, 84:035444, 2011.

[105] C. M. Wang and F. J. Yu. Effects of hexagonal warping on surface transport in topological insulators. *Phys. Rev. B*, 84:155440, 2011.

[106] Xiao-Liang Qi, Rundong Li, Jiadong Zang, and Shou-Cheng Zhang. Inducing a Magnetic Monopole with Topological Surface States. *Science*, 323(5918):1184–1187, 2009.

[107] Rui Yu, Wei Zhang, Hai-Jun Zhang, Shou-Cheng Zhang, Xi Dai, and Zhong Fang. Quantized Anomalous Hall Effect in Magnetic Topological Insulators. *Science*, 329(5987):61–64, 2010.

[108] Desalegne Teweldebrhan, Vivek Goyal, and Alexander A. Balandin. Exfoliation and characterization of bismuth telluride atomic quintuples and quasi-two-dimensional crystals. *Nano Letters*, 10(4):1209–1218, 2012/12/09 2010.

[109] Joel E. Moore. The birth of topological insulators. *Nature*, 464(7286):194–198, 03 2010.

[110] L. Fu and C. L. Kane. Probing Neutral Majorana Fermion Edge Modes with Charge Transport. *Phys. Rev. Lett.*, 102(21):216403, May 2009.

[111] H. Steinberg, D. Gardner, Y. Lee, and P. Jarillo-Herrero. Surface state transport and ambipolar electric field effect in Bi_2Se_3 nanodevices. *Nano Lett.*, 10:5032, 2010.

[112] P.M. Ostrovsky, I.V. Gornyi, and A.D. Mirlin. Interaction-Induced Criticality in Z2 Topological Insulators. *Phys. Rev. Lett.*, 105:036803, 2010.

[113] James G. Analytis, Ross D. McDonald, Scott C. Riggs, Jiun-Haw Chu, G. S. Boebinger, and Ian R. Fisher. Two-dimensional surface state in the quantum limit of a topological insulator. *Nat. Phys.*, 6:960, 2010.

Résumé

Les travaux présentés dans cette thèse ont pour objectif d'apporter à la physique mésoscopique un éclairage concernant la compréhension des propriétés de transport électroniques d'une classe de matériaux récemment découverts : les isolants topologiques.

La première partie de ce manuscrit est une introduction aux isolants topologiques, mettant en partie l'accent sur leurs spécificités par rapport aux isolants "triviaux" : des états de bords hélicaux (dans le cas de l'effet Hall quantique de spin en 2 dimensions) ou de surface relativistes (pour les isolants topologiques tridimensionnels) robustes vis-à-vis du désordre.

La deuxième partie propose une sonde de l'hélicité des états de bords de l'effet Hall quantique de spin en étudiant les propriétés remarquables de l'injection de paires de Cooper dans cette phase topologique.

La troisième partie étudie la diffusion des états de surface des isolants topologiques tridimensionnels dans le régime cohérent de phase. L'étude de la diffusion, de la correction quantique à la conductance (antilocalisation faible) et de l'amplitude des fluctuations universelles de conductance de fermions de Dirac sans masse est présentée. Cette étude est aussi menée dans le cas d'états de surface dont la surface de Fermi présente la déformation hexagonale observée expérimentalement.

Mots-clés : Isolants topologiques ; Effet Hall quantique de spin ; Physique mésoscopique ; Transport électronique cohérent ; Systèmes désordonnés ; (Anti)localisation faible ; Fluctuations universelles de conductance ; Fermions de Dirac ; Réflexion d'Andreev.

Abstract

The works presented in this thesis intend to contribute to condensed matter physics in the understanding of the electronic properties of a recently discovered class of materials : the topological insulators.

The first part of this memoir is an introduction to topological insulators, focusing on their specifities compared to "trivial" insulators : helical edge states (in the two dimensional quantum spin Hall effect) or relativistic surface states (for three dimensional topological insulators) both robust *against* disorder.

The second part proposes a new way to probe the unique properties of the helical edge states of quantum spin Hall effect *via* the injection of Cooper pair from a superconductor.

The third part deals with the diffusion of the three dimensional topological insulator surface states, in the phase coherent regime. The diffusion, the quantum correction to conductivity, and the amplitude of the universal conductance fluctuations are studied. This study is also led in the experimentally relevant case where the Fermi surface presents a hexagonal deformation.

Keywords : Topological insulators : Quantum spin Hall effect ; Mesoscopic physics ; Coherent electronic transport ; Disordered systems ; Weak (anti)localization ; Universal conductance fluctuations ; Dirac fermions ; Andreev reflection.